Doctoral Dissertation (Censored)
博士論文（要約）

Low-Vibration Conductive Cooling of KAGRA Cryogenic Mirror Suspension
(KAGRA 極低温鏡懸架システムの低振動伝導冷却)

A Dissertation Submitted for the Degree of Doctor of Philosophy
December 2020
令和 2 年 12 月博士 (理学) 申請

Department of Physics, Graduate School of Science,
The University of Tokyo
東京大学大学院理学系研究科
物理学専攻

Tomohiro Yamada
山田 智宏

Abstract

Direct detection of the gravitational waves opened a new window to observe the Universe. The recent observations have discovered astronomically important events such as the "mass-gap" objects with $50 - 120\,M_\odot$. These discoveries have provided observational facts for the theories of the formation of black holes and their binaries, and allow us to place restrictions on those theories. To observe more such events, the low-frequency sensitivity of the gravitational wave detector is now highly important.

The Large-scale Cryogenic Gravitational wave Telescope KAGRA is the third km-scale interferometric gravitational wave detector in the world and is expected to contribute to the joint observation with Advanced LIGO and Advanced Virgo in the next observing run O4. One of the most advanced technologies in KAGRA is to cool sapphire mirrors at 20 K for thermal noise reduction. These mirrors are cooled down by thermal radiation and thermal conduction. While thermal radiative cooling is done by non-contact way, thermal conductive cooling requires connecting heat links to the mirror suspension system, and it has been pointed out that these heat links may become a shortcut for vibration which could shake the mirror above the displacement noise requirement level. According to our recent calculation, indeed, it was shown that heat links make the detector sensitivity worse in the low-frequency region.

Therefore, we have developed a device to reduce vibration transfer via heat links, i.e., Heat Link Vibration Isolation System (HLVIS). This system is introduced in the middle of the thermal path and functioned to attenuate vibration via heat links. The HLVIS was considered from the viewpoints of mechanical and thermal aspects. The mechanical performance was practically tested by measuring the mechanical transfer function at cryogenic temperature. The thermal performance was evaluated by the integrated cooling test with the mirror suspension after the installation of the HLVIS in KAGRA. The spring constants of the heat links connecting the HLVIS and the mirror suspension were also practically measured.

We calculated the vibration inflow via the heat links after HLVIS installation based on the measured results and showed that it was successfully reduced under the design sensitivity curve in the observation frequency band although we couldn't satisfy the requirement curve due to some issues. Regarding thermal performance, we confirmed that thermal resistance inside the HLVIS was as designed. However, it was newly found that the temperature of the mirror suspension system was higher than the design due to unknown heat flow. For above mechanical and thermal problems, we have suggested several countermeasures.

It was confirmed that installation of HLVIS greatly contributes to improve the detector sensitivity. In the design sensitivity, detectable volume is expected to be improved by a factor of approximately 2 and 40 for observation of $50 - 50\,\mathrm{M}_\odot$ and $100 - 100\,\mathrm{M}_\odot$ binary black hole mergers. Moreover, in O4, which is scheduled to start in 2022, about 1.5 and 11 times improvements of the number of detections are estimated for $50-50\,\mathrm{M}_\odot$ and $100-100\,\mathrm{M}_\odot$ objects by installing the HLVIS. These achievements by developing the HLVIS are essentially important for observing mass-gap objects.

ACKNOWLEDGMENTS

I had the privilege to join the KAGRA project in the initial phase, and was given the chance to work on one of the most advanced technologies in KAGRA. As a consequence I had the pleasure to work with many great people from the project, I would like to take this opportunity to express my gratitude towards them.

Firstly, I would like to express my sincere gratitude to Professor Takaaki Kajita for giving me this opportunity to work for KAGRA cryogenics. I would not be able to have a fulfilling research life without his support. I would like to thank Professor Takayuki Tomaru for his guidance and for providing me many opportunities to conduct many important research topics. All the experiences in five years have surely led to my self-improvement. I would also like to thank Dr. Takafumi Ushiba for his kind assist and sound advice. I could not complete all measurements without his great support. I would like to thank Professor Toshikazu Suzuki for his great help and I was impressed by his deep knowledge of physics. I would like to thank Dr. Kazuhiro Yamamoto for long time kind assist and I was impressed by his smartness. Dr. Nobuhiro Kimura kindly led me to deep world of cryogenics and I was also impressed by his huge knowledge for zymurgy. I would like to thank Dr. Hirotaka Shimizu, Dr. Suguru Takada, and Dr. Yuki Inoue for great help and fruitful discussion for my research. Special thanks go to Ms. Ayako Node, Ms. Ayako Ueda, Mr. Yoshikazu Namai, Mr. Shin-ichi Terashima, Mr. Iwao Murakami, Mr. Masahiro Takahashi, and Mr. Hiroyasu Sawada for their excellent technical and engineering supports in KEK and Kamioka. A great thanks goes to Professor Ettore Majorana for welcoming me to the Sapienza University of Rome and a lot of discussion for my research. I would also like to thank Dr. Helios Vocca and Dr. Flavio Travasso for great help in HCB bonding and wonderful "Omotenashi" in Italy. Dr. Kieran Craig and Dr. Rahul Kumar were always friendly to me and chatting with them was always refreshing. I would like to thank Mr. Takahiro Miyamoto, Mr. Hiroki Tanaka, Dr. Kunihiko Hasegawa, Mr. Takaharu Shishido, Mr. Masashi Fukunaga, Mr. Bajpai Rishabh, and Mr. Takumi Nishimoto for being great colleagues and it

was a pleasure to work with them.

In the Kamioka site, many staffs kindly supported my research: Professor Masatake Ohashi, Professor Yoshio Saito, Dr. Shinji Miyoki, Dr. Takashi Uchiyama, Dr. Osamu Miyakawa, Dr. Keiko Kokeyama, Dr. Takaaki Yokozawa, Dr. Takahiro Yamamoto, Dr. Shoich Oshino, and Dr. Kazuhiro Hayama. Thanks to their supports, I could deeply focus on my research. Many postdocs also helped my research: Dr. Koki Okutomi, Dr. Lucia Trozzo, Dr. Tatsuki Washimi, Dr. Chihiro Kozakai, Dr. Fabian Pena Arellano, Dr. Darkhan Tuyenbayev, and Dr. Dan Chen. I was quite impressed by discussion with them.

I would like to thank KAGRA technical staffs for their great efforts on the electrical circuits and mine works, etc. I would also like to thank KAGRA office in Kamioka and Kashiwa. Special thanks go to all my colleagues with whom I shared research time.

Most of my research were carried out in KEK with great supports of many people. In Cryogenics Science Center, I would like to thank Professor Tohru Ogitsu, Professor Tatsushi Nakamoto, Dr. Michinaka Sugano, Dr. Kento Suzuki, Mr. Ken-ichi Tanaka, Ms. Emiko Kotaki, and Mr. Tadashi Okazaki. Especially, I have to apologize to Mr. Tanaka and Mr. Okazaki for my un-organized offer of liquid helium. In Accelerator Laboratory, I would like to thank Professor Shinichiro Michizono, Professor Hirotaka Nakai, and Mr. Sakae Araki. Thanks to them, I could complete my experiment despite the pandemic.

Professor Tadashi Koseki, Professor Yasushi Suto, Professor Tadayuki Takahashi, Professor Masato Takita, and Professor Takao Nakagawa reviewed the dissertation. Their comments greatly improved the dissertation.

On a personal front I would like to sincerely thank my family for their support throughout my education. I would also like to thank Mr. Hisashi Hahakabe for his continuous great support.

This research was financially supported by GRASP (Graduate Research Abroad in Science Program) in the University of Tokyo, JSPS (Japan Society for the Promotion of Science) fellowship DC1, and JSR fellowship in the University of Tokyo.

CONTENTS

Chapter 1
INTRODUCTION

Gravitational-wave astronomy is now firmly established even though it has just been five years since gravitational waves were detected directly [1–3]. They have enabled direct observation of black holes. Recently, several massive black holes have been found; component masses in the "mass-gap" region [4, 5]. These events have given new observational knowledge to the theories of black holes and their formation. Since the merger frequencies of the mass-gap objects are approximately below 100 Hz, the low-frequency sensitivity of the gravitational wave detector is now very important.

The Large-scale Cryogenic Gravitational wave Telescope KAGRA is a ground-based interferometric gravitational wave detector constructed under the Kamioka mine in Japan. It is third km-scale interferometric detector in the world and is expected to contribute to the joint observation with Advanced LIGO [6] in the USA and Advanced Virgo [7] in Italy in the next observing run O4 [8]. In the interferometric gravitational wave detector, it is necessary to ultimately reduce any vibration because it measures the position change of the mirror caused by gravitational waves with laser interference. Fundamental noise sources that limit the detector sensitivity at low frequencies are quantum noise due to the quantum nature of light and thermal noise due to thermal fluctuation in the mirror and its suspension. To reduce thermal noise, KAGRA adopts 20 K cryogenic sapphire mirror for first time in the world for a km-scale gravitational wave detector [9–12].

The mirror needs to be cooled with as small vibration as possible, so, it is cooled by thermal radiation in the high-temperature region which is typically from room temperature to 100 K because thermal radiative cooling can be done by non-contact way and it is suitable in terms of vibration transmission. However, thermal conductive cooling must be used at cryogenic temperature because the efficiency of thermal radiation is decreased. Since heat links connect the cooling part and mirror suspension for thermal conductive cooling, it has been

pointed out that these heat links may become a shortcut for vibration inflow and it could shake the mirror above the displacement noise requirement level [15, 16]. According to our recent calculation, indeed, it was shown that the heat links make the detector sensitivity worse in the low-frequency region. Especially for observations of mass-gap objects, the number of detectable events was estimated to be decreased to 1/2 and 1/40 for binary black hole mergers of $50 - 50\,\mathrm{M}_\odot$ and $100 - 100\,\mathrm{M}_\odot$, respectively.

To solve this critical problem, we have developed a device to reduce vibration transfer via the heat links. This system is installed between the cooling part and mirror suspension, that is exactly the middle of thermal path, and functions to attenuate vibration via the heat links; we named this system Heat Link Vibration Isolation System, HLVIS for short. To sufficiently reduce vibration transfer via heat links and not limit heat flow, the HLVIS is considered from the viewpoints of mechanical and thermal aspects. It is composed of three stages with three types of tension springs and designed to attenuate vibration transfer below the noise requirement curve in KAGRA.

In this dissertation, the detailed mechanical design of the HLVIS and the experimental results of the mechanical transfer function measurement are presented. The measured results of the spring constant of the heat link, which is a critical parameter to decide amount of vibration transfer, are also reported. The thermal design and a pre-experiment enabling more accurate thermal design are described. Based on the above results, improvement of the detector sensitivity is discussed, and the reasonable sensitivity curve in O4 reflecting thermal issue newly found is also shown.

Outline of the dissertation

This dissertation is organized as follows. Chapter 2 briefly reviews the theory of gravitational waves, the principle of interferometric gravitational wave detector, and major noise sources. Physics with gravitational waves are summarized in the last section. Chapter 3 overviews KAGRA gravitational wave detector focusing on the cryogenic parts. Chapter 4 is the background of this study. Details of the heat link are discribed with measured data, and the past cooling results are analyzed using these data. After calculating vibration inflow via heat links, the target of this study is stated. Chapters $5-7$ are the core part of this dissertation. Chapter 5 describes the design of the HLVIS. Chapter 6 reports the mechanical performance test results carried out in KEK. In the last section, the improvement of the sensitivity by installing the HLVIS is discussed. Chapter 7 reports the performance tests in KAGRA. The thermal performance of the HLVIS is discussed using the integrated cooling test results. The estimated vibration inflow via heat links and the latest sensitivity curves are compared in the last section. Chapter 8 provides the future prospects and concludes the dissertation.

Chapter 2
GRAVITATIONAL WAVES AND DETECTION

Gravitational waves are very small ripples of curved spacetime. They are produced by the accelerating movement of objects with mass. They change the distance between two objects so that it is possible to detect them by measuring the distance very precisely. A laser interferometer plays this role with advanced techniques.

This chapter briefly reviews the theory and principle of detection of gravitational waves, major noise sources in the interferometric gravitational wave detector, recent observation results, and their physics.

2.1 Theory of gravitational waves

Gravitational waves are derived from the Einstein equation. It is first linearized and the gravitational waves are derived. Their polarization and the effect onto the test particle are considered. The quadruple radiation and energy transfer by gravitational waves are explained.

2.1.1 Einstein equation

Gravitational waves are derived as a waveform of the linearized Einstein equation, which can be expressed as [18, 19]

$$G_{\mu\nu} = R_{\mu\nu} - \frac{1}{2} g_{\mu\nu} R = \frac{8\pi G}{c^4} T_{\mu\nu}, \tag{2.1}$$

where $G_{\mu\nu}$, $R_{\mu\nu}$, $g_{\mu\nu}$, R, and $T_{\mu\nu}$ are Einstein tensor, Ricci tensor, metric tensor, scalar curvature, and energy-momentum tensor, respectively. G and c are New-

tonian constant of gravitation and speed of light, respectively. In vacuum, since $T_{\mu\nu}$ is zero, equation (2.1) can be derived as

$$R_{\mu\nu} - \frac{1}{2} g_{\mu\nu} R = 0. \tag{2.2}$$

The metric of Minkowski spacetime is defined as

$$\eta_{\mu\nu} = \begin{pmatrix} -1 & 0 & 0 & 0 \\ 0 & 1 & 0 & 0 \\ 0 & 0 & 1 & 0 \\ 0 & 0 & 0 & 1 \end{pmatrix}. \tag{2.3}$$

Here, we consider metrics that are close to flat spacetime:

$$g_{\mu\nu} = \eta_{\mu\nu} + h_{\mu\nu}. \tag{2.4}$$

The amplitude $h_{\mu\nu}$ are small perturbations to the flat spacetime:

$$|h_{\mu\nu}| \ll 1 \tag{2.5}$$

$h_{\mu\nu}$ satisfies everywhere across spacetime.

We introduce the Riemann tensor $R_{\mu\nu\alpha\beta}$ to express equation (2.1) with $h_{\mu\nu}$. The Riemann tensor $R_{\mu\nu\alpha\beta}$ is

$$R_{\mu\nu\alpha\beta} = \frac{1}{2}\left(\frac{\partial^2 g_{\mu\beta}}{\partial x^\nu \partial x^\alpha} + \frac{\partial^2 g_{\nu\alpha}}{\partial x^\mu \partial x^\beta} - \frac{\partial^2 g_{\nu\beta}}{\partial x^\mu \partial x^\alpha} - \frac{\partial^2 g_{\mu\alpha}}{\partial x^\nu \partial x^\beta}\right) + \left(\Gamma_{\rho,\nu\alpha}\Gamma^{\rho}{}_{\mu\beta} - \Gamma_{\rho,\mu\alpha}\Gamma^{\rho}{}_{\nu\beta}\right). \tag{2.6}$$

Γ is the Christoffel symbol and is defined as

$$\Gamma^{\mu}{}_{\nu\lambda} = \frac{1}{2} g^{\mu\alpha}(g_{\alpha\nu,\lambda} + g_{\alpha\lambda,\nu} - g_{\nu\lambda,\alpha}). \tag{2.7}$$

We consider $h_{\mu\nu}$ until the first order, then the Riemann tensor can be calculated as

$$R_{\mu\nu\alpha\beta} = \frac{1}{2}(h_{\mu\beta,\nu\alpha} + h_{\nu\alpha,\mu\beta} - h_{\nu\beta,\mu\alpha} - h_{\mu\alpha,\nu\beta}). \tag{2.8}$$

Relationship between the Riemann and Ricci tensors are

$$R_{\mu\nu} = R^{\alpha}{}_{\mu\alpha\nu}, \tag{2.9}$$

and $R_{\nu\beta}$ is expressed as

$$R_{\nu\beta} = \frac{1}{2}\left(h^{\mu}{}_{\beta,\mu\nu} + h^{\mu}{}_{\nu,\mu\beta} - h_{\nu\beta,\mu}{}^{,\mu} - h^{\mu}{}_{\mu,\nu\beta}\right). \tag{2.10}$$

Moreover, the scalar curvature R can be derived as

$$R = \left(h^{\mu}{}_{\beta}{}^{,\beta}{}_{,\mu} - h^{\mu}{}_{\mu}{}^{,\beta}{}_{,\beta}\right) \tag{2.11}$$

by contracting equation (2.10) with ν, μ. We define $\bar{h}_{\mu\nu}$ as

$$\bar{h}_{\mu\nu} \equiv h_{\mu\nu} - \frac{1}{2}\eta_{\mu\nu}h, \tag{2.12}$$

$$h \equiv h^{\rho}{}_{\rho}, \tag{2.13}$$

and calculate equation (2.1) with equation (2.10) and equation (2.11). By giving Lorentz gauge condition $\bar{h}^{\rho}{}_{\mu,\rho} = 0$, the linearized Einstein equation in vacuum is derived as

$$\Box\bar{h}_{\mu\nu} = \left(-\frac{\partial^2}{\partial t^2} + \frac{\partial^2}{\partial x^2} + \frac{\partial^2}{\partial y^2} + \frac{\partial^2}{\partial z^2}\right)\bar{h}_{\mu\nu} = 0. \tag{2.14}$$

When we consider the energy-momentum tensor, equation (2.14) is

$$\Box\bar{h}_{\mu\nu} = -\frac{16\pi G}{c^4}T_{\mu\nu}. \tag{2.15}$$

Equation (2.15) shows that gravitational waves are generated by time varying $T_{\mu\nu}$.

2.1.2 Gravitational wave polarization

A plane wave solution as equation (2.16) can be considered as an solution of equation (2.14):

$$\bar{h}_{\mu\nu} = A_{\mu\nu}\exp(\mathrm{i}k_{\alpha}x^{\alpha}). \tag{2.16}$$

When this plane wave solution satisfy the Lorentz gauge condition and equation (2.14), equation (2.16) needs to satisfy following two conditions:

$$A_{\mu\nu}k^{\nu} = 0, \tag{2.17}$$

$$k_{\mu}k^{\mu} = 0. \tag{2.18}$$

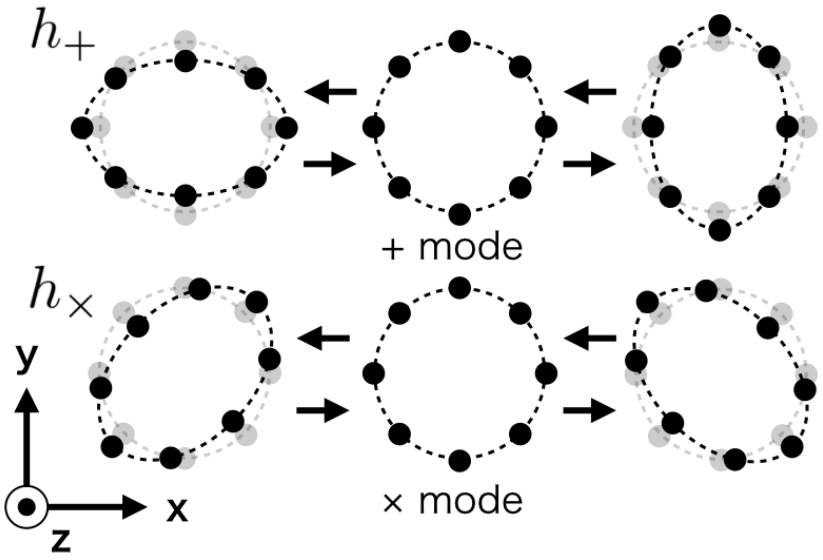

Figure 2.1: Schematic view of movement of the test particles by gravitational waves traveling along z axis. Test masses move tidally.

equation (2.17) indicates that the plane wave solution is a transverse wave, and equation (2.18) indicates that the gravitational waves propagate with the speed of light. Transforming equation (2.16) into Transverse-Traceless (T-T) gauge condition equation (2.19) and equation (2.20)) gives equation (2.21).

$$A^{\mu}{}_{\mu} = 0 \tag{2.19}$$

$$A_{\mu\nu}U^{\nu} = 0 \tag{2.20}$$

U^{ν} is an arbitrary unit vector including time. When we consider plane wave propagation to the z-direction, it is obvious that gravitational waves have two polarization modes: + mode and × mode (see figure 2.1).

$$A^{\mathrm{TT}}_{\mu\nu} = \begin{pmatrix} 0 & 0 & 0 & 0 \\ 0 & A_{xx} & A_{xy} & 0 \\ 0 & A_{xy} & -A_{xx} & 0 \\ 0 & 0 & 0 & 0 \end{pmatrix} = A^{+}_{\mu\nu} + A^{\times}_{\mu\nu} \tag{2.21}$$

$$A^{+}_{\mu\nu} = \begin{pmatrix} 0 & 0 & 0 & 0 \\ 0 & A_{xx} & 0 & 0 \\ 0 & 0 & -A_{xx} & 0 \\ 0 & 0 & 0 & 0 \end{pmatrix}, A^{\times}_{\mu\nu} = \begin{pmatrix} 0 & 0 & 0 & 0 \\ 0 & 0 & A_{xy} & 0 \\ 0 & A_{xy} & 0 & 0 \\ 0 & 0 & 0 & 0 \end{pmatrix} \tag{2.22}$$

From here, $A^{+}_{\mu\nu} = h_{+}$, $A^{\times}_{\mu\nu} = h_{\times}$ are defined for sake of simplicity.

2.1.3 Effect onto the test particle

TT-gauge condition is applied to the system that the test particle is at rest. The test particle follows the equation of geodesic deviation equation (2.23)

$$\frac{\mathrm{d}}{\mathrm{d}\tau}U^{\mu} + \Gamma^{\mu}{}_{\alpha\beta}U^{\alpha}U^{\beta} = 0. \tag{2.23}$$

Since the test particle is at rest first, an initial value of its acceleration is

$$\left(\frac{\mathrm{d}U^{\mu}}{\mathrm{d}\tau}\right)_0 = -\Gamma^{\mu}{}_{00} = -\frac{1}{2}\eta^{\mu\nu}(h_{\nu 0,0} + h_{0\nu,0} - h_{00,\nu}). \tag{2.24}$$

Since $h^{\mathrm{TT}}_{\mu 0}$ is zero, initial velocity is zero. This discussion indicates that the test particle will be at rest forever in TT coordinate system.

When the light flies along x-axis, the proper distance can be expressed as

$$\Delta l = \int |ds^2|^{1/2} = \int |g_{\alpha\beta}dx^{\alpha}dx^{\beta}|^{1/2} = \int_0^{\varepsilon} |g_{xx}|^{1/2}\mathrm{d}x \approx \left[1 + \frac{1}{2}h^{\mathrm{TT}}_{xx}(x=0)\right]\varepsilon. \tag{2.25}$$

Since h^{TT}_{xx} is not zero generally, we can find that the proper distance has time variation. A laser light flies a geodesic so that it can measure the change of the proper distance. This is a fundamental principle of the laser interferometric gravitational wave detector such as KAGRA.

2.1.4 Gravitational wave emission

A solution of equation (2.15) can be written as

$$\bar{h}_{\mu\nu} = \frac{4G}{c^4} \int \frac{\tau_{\mu\nu}(t - |\boldsymbol{x} - \boldsymbol{x'}|, \boldsymbol{x'})}{|\boldsymbol{x} - \boldsymbol{x'}|} \mathrm{d}^3\boldsymbol{x'}. \tag{2.26}$$

where $\tau_{\mu\nu}$ is the energy momentum pseudotensor. The mass quadruple momentum is expressed as

$$I_{ij} = \int \rho x^i x^j \ \mathrm{d}^3 x, \tag{2.27}$$

so that traceless part of the momentum is derived as

$$\bar{I}_{ij} = \int \rho \left(x^i x^j - \frac{1}{3}\delta_{ij} r^2 \right) \mathrm{d}^3 x. \tag{2.28}$$

Therefore, the amplitude of gravitational waves can be expressed as

$$h_{ij}^{\mathrm{TT}} = \frac{2G}{c^4 r} \frac{\partial^2}{\partial t^2} \bar{I}_{ij}(t - r), \tag{2.29}$$

where r is the distance from the origin of gravitational waves.

2.2 Interferometric gravitational wave detector

Laser interferometric gravitational wave detector makes possible to realize high sensitivity in wide frequency range. This section briefly reviews the principle of the laser interferometric gravitational wave detector.

2.2.1 Michelson interferometer

As explained in section 2.1.3, a laser interferometric gravitational wave detector detects gravitational-wave signals by measuring the proper distance. Its basic configuration is the Michelson interferometer as shown in figure 2.2.

In the Michelson interferometer, a laser beam goes into the Beam Splitter (BS) and become two orthogonal lights [20]. These lights individually fly along x and y arms and come back from both ends by reflecting of the mirrors (Test Masses). Reflected lights recombine at the BS to produce interference. When gravitational waves enter the interferometer, they change the proper distances of two arms in anti-phase. Therefore, the phase difference occurs in the reflected lights, and we can detect gravitational-wave signals.

Response to the gravitational wave

We consider the response of the Michelson interferometer to the gravitational wave [21]. When + mode gravitational wave is entering the interferometer, ds^2 is given by

$$ds^2 = -c^2dt^2 + (1 + h_+(t))dx^2 + (1 - h_+(t))dy^2 + dz^2, \tag{2.30}$$

where $h_\times = 0$. $h_+(t)$ means time variance of the amplitude of gravitational waves at the position of the observer.

Since $ds^2 = 0$ for light, by equation (2.30), the one going to x-axis can be expressed as

$$dx = \pm\frac{cdt}{\sqrt{1 + h_+(t)}} \sim \pm\left(1 - \frac{1}{2}h_+(t)\right)cdt. \tag{2.31}$$

Let τ_x be time it takes for the light to travel both ways between Beam Splitter and the mirror. Integrating both sides of equation (2.31) gives

$$\frac{2L_x}{c} = \int_{t-\tau_x}^{t}\left(1 - \frac{1}{2}h_+(t)\right)\mathrm{d}t. \tag{2.32}$$

By $h \ll 1$, the phase difference in both ways can be written as

$$\phi_x = \Omega\tau_x \sim \Omega\frac{2L_x}{c} + \frac{\Omega}{2}\int_{t-\frac{2L_x}{c}}^{t} h_+(t)\mathrm{d}t. \tag{2.33}$$

Here, $\tau_x \sim \frac{2L_x}{c}$ is assumed. Ω is an angular frequency of the laser. As with x-axis, the phase difference along y-axis can be written as

$$\phi_y = \Omega\tau_y \sim \Omega\frac{2L_y}{c} + \frac{\Omega}{2}\int_{t-\frac{2L_y}{c}}^{t} h_+(t)\mathrm{d}t. \tag{2.34}$$

Total phase difference of lights travelling along x and y-axis is written as

$$\begin{aligned}\Delta\phi &= \Omega\frac{2(L_x - L_y)}{c} + \frac{\Omega}{2}\int_{t-\frac{2L_x}{c}}^{t} h_+(t)\mathrm{d}t + \frac{\Omega}{2}\int_{t-\frac{2L_y}{c}}^{t} h_+(t)\mathrm{d}t \\ &= \Omega\frac{2(L_x - L_y)}{c} + \Delta\phi_{\mathrm{GW}}\end{aligned} \tag{2.35}$$

Here, $\Delta\phi_{\mathrm{GW}}$ expresses the phase difference produced by gravitational waves. When $L_x \sim L_y \sim L$ is assumed, $\Delta\phi_{\mathrm{GW}}$ can be expressed as

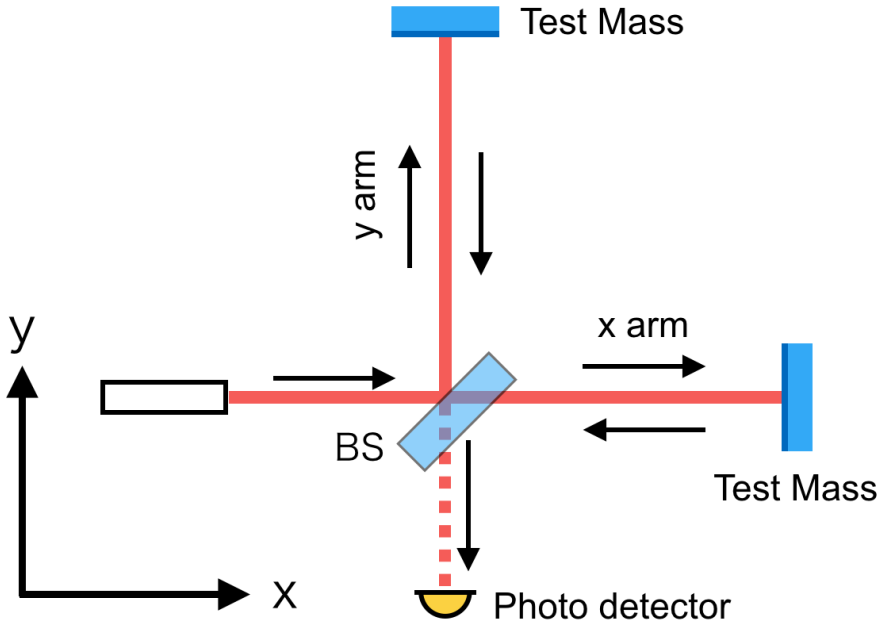

Figure 2.2: Schematic view of the Michelson interferometer. A laser beam is divided into two beams at the BS, each beam flies along x and y arms and come back from both ends by reflecting of the end mirrors.

$$\Delta\phi_{\mathrm{GW}} = \Omega \int_{t-\frac{2L}{c}}^{t} h_{+}(t)\mathrm{d}t. \tag{2.36}$$

Frequency response and baseline length

We consider the frequency response of the Michelson interferometer. Applying the Fourier transform to the $h_{+}(t)$ gives

$$h_{+}(t) = \int_{-\infty}^{\infty} h(\omega)e^{i\omega t}\mathrm{d}\omega. \tag{2.37}$$

We obtain following equation (2.38) by inserting equation (2.37) into equation (2.36).

$$\begin{aligned}\Delta\phi_{\mathrm{GW}} &= \Omega \int_{t-\frac{2L}{c}}^{t} \int_{-\infty}^{\infty} h(\omega) e^{i\omega t} \mathrm{d}\omega \mathrm{dt} \\ &= \int_{-\infty}^{\infty} \frac{2\Omega}{\omega} e^{i\omega(t-\frac{L}{c})} \sin\left(\frac{L\omega}{c}\right) h(\omega) \mathrm{d}\omega \\ &= \int_{-\infty}^{\infty} H_{\mathrm{MI}}(\omega) h(\omega) \mathrm{d}\omega\end{aligned} \tag{2.38}$$

$H_{\mathrm{MI}}(x)$ is the frequency response function of the Michelson interferometer:

$$H_{\mathrm{MI}}(x) = \frac{2\Omega}{\omega} e^{i\omega(t-\frac{L}{c})} \sin\left(\frac{L\omega}{c}\right), \tag{2.39}$$

where ω is an angular frequency of gravitational waves.

Equation (2.39) gives a condition that maxmizes $|H_{\mathrm{MI}}(x)|$:

$$\frac{L\omega}{c} = \frac{\pi}{2}. \tag{2.40}$$

If we extend the length of the baseline more from equation (2.40), we cannot expect further better sensitivity. This is because the effect of gravitational waves will be integrated during the traveling time of lights. For 100 Hz and 1 kHz gravitational waves, we can calculate that the optimal baseline length is 750 km and 75 km by equation (2.40), respectively, for example.

2.2.2 Fabry-Perot Michelson interferometer

It is almost impossible to construct such a large interferometer with several-100 km baseline on the earth. Therefore, a Fabry-Perot cavity is constructed to extend effective baseline length by installing a mirror in the center-side as shown in figure 2.3 [20]. Light from the BS first passes through a center-side mirror (Input Test Mass, ITM), then come back to the ITM from the end by reflecting of the end mirror (End Test Mass, ETM). There is a high-reflection coating on the cavity-side surface of the ITM so that the light is reflected towards the ETM again. Since the reflectivity of the ITM is slightly lower than the ETM's, light stored in the cavity comes out from the arm little by little.

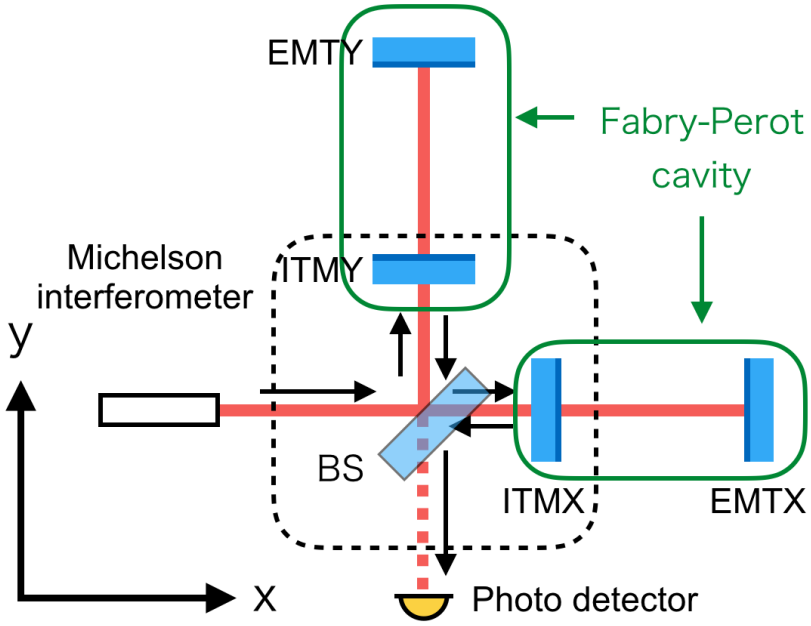

Figure 2.3: Schematic view of the Fabry-Perot Michelson interferometer. Another mirror is installed between the BS and the ETM to constitute the Fabry-Perot cavity in each arm.

The response function of the Fabry-Perot Michelson interferometer is expressed as [21]

$$|H_{\mathrm{FPMI}}(x)| = \frac{2\alpha\Omega}{\omega(1 - r_{\mathrm{I}} r_{\mathrm{E}})} \frac{|\sin\gamma|}{\sqrt{1 + F\sin^2\gamma}}. \tag{2.41}$$

Here, α, γ, and F are

$$\alpha = \frac{t_{\mathrm{I}}^2 r_{\mathrm{E}}}{-r_{\mathrm{I}} + (r_{\mathrm{I}}^2 + t_{\mathrm{I}}^2) r_{\mathrm{E}}}, \tag{2.42}$$

$$\gamma = \frac{L\omega}{c}, \tag{2.43}$$

$$F = \frac{4 r_{\mathrm{I}} r_{\mathrm{E}}}{(1 - r_{\mathrm{I}} r_{\mathrm{E}})^2} = \left(\frac{2\mathcal{F}}{\pi}\right)^2. \tag{2.44}$$

t_{I}, r_{I}, r_{E}, L are the transmissivity of ITM, the reflectivity of ITM, the reflectivity of ETM, and the cavity length. $\mathcal{F}$ is called as finess, this is the value to show

the steepness of resonance of Fabry-Perot cavity. Using the finess $\mathcal{F}$, average number of round trips is defined as

$$N = \frac{2\mathcal{F}}{\pi}. \tag{2.45}$$

In KAGRA, other advanced optical techniques are also used such as power recycling [22], signal recycling, and resonant sideband extraction techniques [23]. The power recycling technique is picked up and explained below because it is strongly related with heat input into the Test Mass.

2.2.3 Power recycling technique

Power recycling is a technique to increase the effective input laser power [22]. When the interferometer is in operation, the output port is controlled to be "dark", i.e. reflected lights from arms are canceled out, therefore, most lights go back to the way to the laser. The power recycling technique reflects those lights back to the interferometer and constitute a cavity between a power recycling mirror and the whole interferometer (see figure 2.4).

When the power recycling is performed, a large amount of laser transmits to ITM. Although substrates with low absorption are chosen for the mirror, heat absorption from passing laser is not negligible. In room-temperature detectors, the thermal compensation system is adopted to compensate for the thermal lensing effect by laser absorption at the center of the mirror. In KAGRA, since the temperature is very low, the thermal lensing effect is negligible, however, injected heat must be somehow extracted. High thermal conductive fibers play an important role in this, details are described in section 3.2 [24].

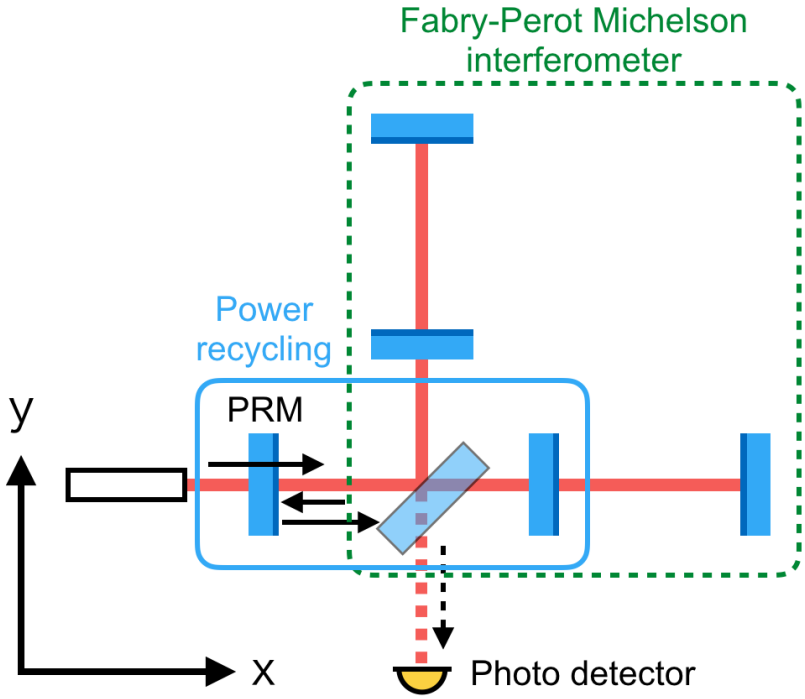

Figure 2.4: Schematic view of relationship between the power recycling mirror and the Fabry-Perot Michelson interferometer. A light from the Fabry-Perot Michelson interferometer is reflected back to the interferometer at the PRM.

2.3 Major noise sources

In order to detect tiny signals of gravitational waves, every noise source needs to be carefully considered. A ground-based interferometric gravitational wave detector has several fundamental noise sources, which cannot be overcome. Seismic noise due to seismic vibration which dominates very low frequency. Quantum noise due to the quantum nature of light dominates almost the whole frequency region. Thermal noise due to thermal fluctuation is a dominant noise source at low frequency. This section briefly reviews fundamental noise sources in the interferometric gravitational wave detector.

2.3.1 Seismic noise

Ground is always vibrating by not only earthquakes but also human activities, wind, and sea waves, etc [25, 26]. Since seismic noise level depends on the place, the easiest way to reduce it is to build the detector in a quiet vibration area: it is usually far from the urban area.

Seismic vibration level of such area is, however, still very large to detect gravitational waves. Therefore, Test Masses must be strictly isolated from seismic vibration and a pendulum system is usually adopted for this purpose. When a mass is suspended by a wire with length of l, a displacement transfer function from the suspension point to the mass is derived as

$$H(\omega) = \frac{\omega_0^2}{-\omega^2 + \omega_0^2}, \tag{2.46}$$

where ω is angular frequency and $\omega_0 = \sqrt{g/l}$. g is gravitational acceleration. As shown with blue curve in the figure 2.5, it can be found that the transfer function has a inclination of f^{-2} above the resonant frequency. Furthermore, when a pendulum has multiple stages, above the resonant frequencies, the inclination of the transfer function can be expressed as

$$|H(f)| \propto f^{-2n}. \tag{2.47}$$

Since the observation frequency band of the ground-based gravitational wave detector is typically above 10 Hz, the multiple stage pendulum is required to achieve high vibration attenuation ratio in the observation frequency band.

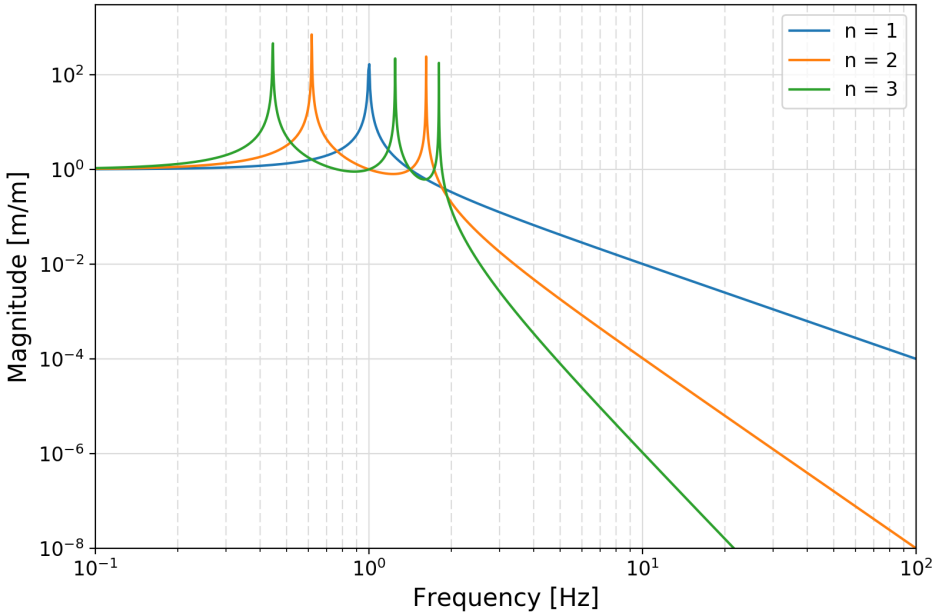

Figure 2.5: Mechanical transfer function of various numbers of stages. An index of n represents the number of stages.

2.3.2 Quantum noise

There are two noises in the quantum noise: shot noise and the radiation pressure noise [20]. Shot noise is caused by statistical fluctuations in the number of photons at the output port of the interferometer. When N-photons enter a photodetector, the fluctuation in number of photons will be proportional to the square root N. The gravitational-wave signal is proportional to laser power and shot noise is proportional to the square root of the power, therefore, the signal-to-noise ratio of shot noise is proportional to the square root of the power.

On the other hand, radiation pressure noise is caused by random photons hitting the test mass so that the signal-to-noise ratio of radiation pressure noise is inversely proportional to the square root of laser power.

2.3.3 Thermal noise

Thermal noise is caused by thermal fluctuation of the molecules and atoms that compose the test mass and its suspension system [27]. The amplitude of the thermal fluctuation force is product of temperature T and loss angle ϕ [28]:

$$P(\Omega) \propto T\phi, \tag{2.48}$$

where $P(\Omega)$ is the power spectrum density of the fluctuation. Loss angle represents ease of energy dissipation from the system; large loss angle means that energy dissipates easily from the system. To decrease thermal noise, temperature T should be low and loss angle ϕ should be small. There are roughly two kinds of thermal noise to be considered: mirror thermal noise and suspension thermal noise.

Mirror thermal noise

Sources of dissipation for the mirror thermal noise is located in the mirror substrate and coatings. For both, two types of dissipation exist: structure damping and thermoelastic damping. It is experimentally known that the structure damping can be considered as white noise, and it is also called Brownian noise. The thermoelastic damping is caused by heat relaxation in the inhomogeneous strain. The power spectrum densities of mirror thermal noise in the mirror substrate are given by [28]

$$P_{\mathrm{MirrorsubBrown}}(\Omega) = \left(\frac{2}{L}\right)^2 \frac{4k_{\mathrm{B}}T(1-\sigma_{\mathrm{sub}}^2)\phi_{\mathrm{sub}}}{\sqrt{\pi}E_{\mathrm{sub}}w_0\omega}, \tag{2.49}$$

$$P_{\mathrm{Mirrorsubthermo}}(\Omega) = \left(\frac{2}{L}\right)^2 \frac{16k_{\mathrm{B}}T^2\alpha_{\mathrm{sub}}^2 w_0 J_{\mathrm{sub}}(\Omega_{\mathrm{c}})}{\sqrt{\pi}\kappa_{\mathrm{sub}}}, \tag{2.50}$$

$$J_{\mathrm{sub}}(\Omega_{\mathrm{c}}) = \frac{\sqrt{2}}{\pi^{3/2}} \int_0^\infty du \int_{-\infty}^\infty dv \frac{u^3 \mathrm{e}^{-u^2/2}}{(u^2+v^2)[(u^2+v^2)^2+\Omega_{\mathrm{c}}^2]}, \tag{2.51}$$

$$\Omega_{\mathrm{c}} = \frac{\Omega\rho_{\mathrm{sub}}c_{\mathrm{sub}}w_0^2}{2\kappa_{\mathrm{sub}}}. \tag{2.52}$$

The parameters L, k_{B} and w_0 represent the arm length, Stefan-Boltzmann constant, and beam radius at mirror, respectively. The parameters σ_{sub}, ϕ_{sub}, E_{sub}, α_{sub}, κ_{sub}, ρ_{sub}, and c_{sub} denote the Poisson ratio, loss angle of mirror substrate,

Young's modulus, thermal expansion coefficient, thermal conductivity, density, and specific heat per unit mass of the mirror substrate, respectively.

Although there are four orders of magnitude difference between the thickness of the reflective coating layers ($\sim 10\,\mu$m) and mirror substrate ($\sim 100\,$mm), the loss angle of coating is four orders of magnitude larger than the substrate, so coating thermal noise cannot be ignored. The power spectrum densities of coating thermal noise are given by [28]

$$G_{\rm MirrorcoatBrown}(\Omega) = \left(\frac{2}{L}\right)^2 \frac{8k_{\rm B}T(1+\sigma_{\rm sub})(1-2\sigma_{\rm sub})d_{\rm coat}\phi_{\rm coat}}{\sqrt{\pi}E_{\rm sub}w_0^2\omega}, \quad (2.53)$$

$$G_{\rm Mirrorcoat\,thermo}(\Omega) = \left(\frac{2}{L}\right)^2 \frac{2k_{\rm B}T^2\left[2\alpha_{\rm eff}d_{\rm coat}(1+\sigma_{\rm sub})-\beta_{\rm eff}\lambda\right]^2}{\pi w_0\kappa_{\rm sub}} \times J_{\rm coat}(\Omega_c), \quad (2.54)$$

$$J_{\rm coat}(\Omega_{\rm c}) = \frac{2\sqrt{2}}{\pi}\int_0^\infty du\int_{-\infty}^\infty dv\frac{u(u^2+v^2)\mathrm{e}^{-u^2/2}}{(u^2+v^2)^2+\Omega_{\rm c}^2}. \quad (2.55)$$

The parameters $d_{\rm coat}$ and $\phi_{\rm coat}$ represent the thickness and loss angle of the coating, $\alpha_{\rm eff}$ and $\beta_{\rm eff}$ are the effective thermal expansion and effective temperature dependence of the refractive index of the coating, respectively. λ is the wavelength of laser.

Suspension thermal noise

Suspension thermal noise also caused by the structure damping and thermoelastic damping. The power spectrum density of suspension thermal noise is given by [28]

$$P_{\rm Suspension} = \left(\frac{2}{L}\right)^2 \frac{4k_{\rm B}Tg}{m\Omega^5 l_{\rm fiber}}(\phi_{\rm fiber}+\phi_{\rm fiberthermo}) \times\sqrt{\frac{4\pi E_{\rm fiber}}{mgl_{\rm fiber}^2}}\left(\frac{d_{\rm fiber}}{4}\right)^2, \quad (2.56)$$

$$\phi_{\rm fiberthermo} = \frac{\alpha_{\rm fiber}^2 E_{\rm fiber}T}{\rho_{\rm fiber}c_{\rm fiber}}\frac{f/f_0}{1+(f/f_0)^2},\quad f_0 = 2.16\frac{\kappa_{\rm fiber}}{\rho_{\rm fiber}c_{\rm fiber}d_{\rm fiber}^2}. \quad (2.57)$$

The parameters g is the gravitational acceleration, $l_{\rm fiber}$, $d_{\rm fiber}$, and $E_{\rm fiber}$ are the length, diameter, Young's modulus of fiber, respectively. $\phi_{\rm fiber}$ and $\phi_{\rm fiberthermo}$

represent the loss angles by structure damping and thermoelastic damping of the fiber, respectively. α_{fiber}, κ_{fiber}, ρ_{fiber}, and c_{fiber} are the thermal expansion coefficient, thermal conductivity, density, and specific heat per unit mass, respectively. The latter term in the right-hand-side of equation (2.56) express the ratio between its elastic restoring force and the gravitational force, which represents the dilution of the dissipation inside the suspension fiber.

2.4 Observation of gravitational waves

Several observing runs have been carried out in the last few years. The first observing run (O1) from September 12th, 2015 until January 19th, 2016 by the Advanced LIGO detected three events including the first direct detection of the gravitational-wave [1]. The second observing run (O2) started on November 30th, 2016, and ended on August 25th, 2017. The Advanced Virgo joined O2 from August 1st, 2017, and enabled the first three-detector observation of gravitational waves [29]. O2 found eight events including a binary neutron star merger. Results from O1 and O2 were summarized in the Gravitational-Wave Transient Catalog (GWTC-1) [30]. O3 was divided into three phases: O3a was carried out from April 1st to September 30th, 2019, O3b was done from November 1st, 2019 to late March 2020, and O3GK was performed from April 7th to 21st, 2020 only by GEO600 and KAGRA. O3GK was the first joint observation for KAGRA in the international gravitational-wave observation network. At present, O3a data is published as GWTC-2, and thirty-nine gravitational wave events in total are described such as massive binary black holes and binary systems with asymmetric mass ratio [31].

2.4.1 Observed gravitational wave events

Several notable events are picked up and briefly explained here.

- **GW150914 :** The first detected gravitational waves [1]. As a result of the coalescence of binary black hole with $35.6^{+4.7}_{-3.1}\,M_\odot$ and $30.6^{+3.0}_{-4.4}\,M_\odot$, a black hole with $63.1^{+3.4}_{-3.0}\,M_\odot$ was formed and the energy of $3.1^{+0.4}_{-0.4}\,M_\odot c^2$ was radiated in gravitational waves. This is the first event to show the existence of a stellar-mass black hole.

- **GW170814 :** The first detected gravitational waves by three-detector observation [29]. The area of the 90 % credible region was reduced from $1160\,\mathrm{deg}^2$ to $60\,\mathrm{deg}^2$ using all three detectors

- **GW170817 :** The first detection of gravitational waves from binary neutron stars [2]. Two space telescopes, Fermi Gamma-ray Space Telescope and INTEGRAL, detected the short gamma-ray burst GRB 170817A after 1.7 s of the coalescence. Subsequent electro-magnetic observation identified a counterpart object in the NGC 4993.

- **GW190521 :** The gravitational waves generated by massive binary black holes, resulting in $150.3^{+35.8}_{-20.0}\,M_\odot$ after coalescence [4]. A primary mass $\sim 85\,M_\odot$ forces to reconsider the cut off mass range inferred from the GWTC-1.

- **GW190814 :** The gravitational waves from a highly asymmetric system [32]. They had a confidently unequal mass ratio ($q = 0.28^{+0.12}_{-0.06}$) and exhibited strong signs of higher harmonics in the waveform.

In addition to the above events, there are many other important events listed in the GWTC-1 and the GWTC-2.

2.4.2 Observing scenarios over the next several years

At the time of writing this dissertation, all the gravitational wave detectors in the world are stopping their operation and upgrading instruments to achieve better sensitivity. In KAGRA, many works are carried out in parallel such as modification of optics, installation of baffles, upgrade and repair of suspensions, and replacement of cryocoolers towards the next observing run. Currently, two observing runs, O4 and O5, are scheduled around 2022 and 2025 as shown in figure 2.6 [8].

In O4, the following observational ranges[‡1] are estimated: Advanced LIGO at $160 - 190$ Mpc, Advanced Virgo at $90 - 120$ Mpc, and KAGRA at $25 - 130$ Mpc. In O5, the target sensitivity ranges are 330 Mpc for Advanced LIGO, $150 - 260$ Mpc for Advanced Virgo, and over 130 Mpc for KAGRA. The above sensitivities and precise dates of these runs are now being actively planned and remain fluid. Reasonable detector configuration in KAGRA for O4 is discussed in section 7.3.2.

[‡1] The distance at which gravitational waves associated with the binary neutron star merger with $1.4 - 1.4\,M_\odot$ can be detected by signal-to-noise ratio 8.

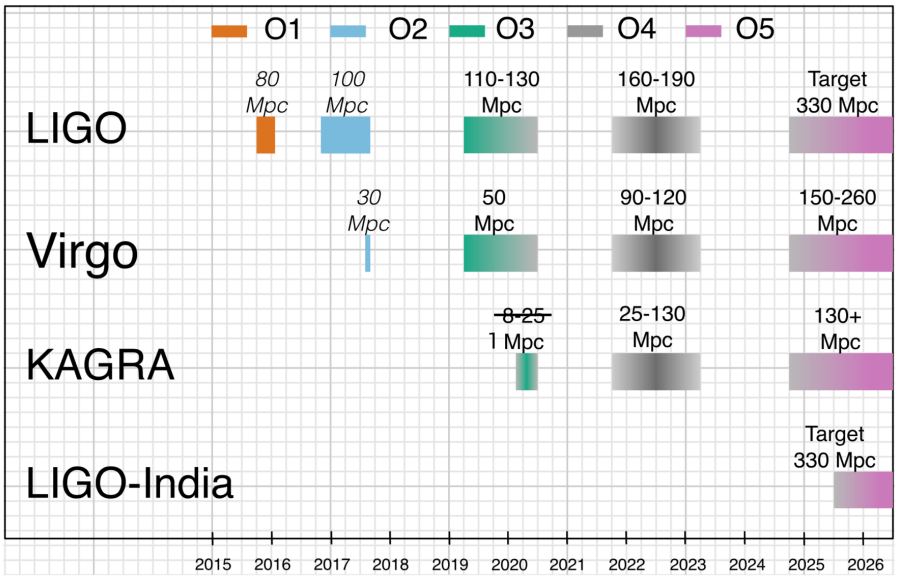

Figure 2.6: Planned sensitivity evolution and observing runs of the Advanced LIGO, Advanced Virgo, KAGRA over the next several years [8].

2.5 Physics with gravitational waves

As introduced in section 2.4.1, gravitational waves have revealed various astronomical information such as the existence of a stellar-mass black hole and the origin of short Gamma-Ray Burst. On the other hand, discrepancies between observed results and theories have also arisen. Focusing on heavy black holes, I consider the physics with gravitational waves for near future.

2.5.1 Population of binary black holes

A lot of theories are considered for binary black hole formation. The isolated binary black hole may be formed by common envelope evolution [33], the remnant of Population Ⅲ stars [34], or chemically homogeneous stellar evolution [35]. Also, near the cluster, binary black hole mergers could occur via dynamical interactions in young stellar clusters, globular clusters, nuclear star clusters [36], triple systems [37], or the disks of active galactic nuclei [38]. Or, a part of a primordial black hole population in the early Universe might be an origin of a binary black hole [39].

The common envelope scenario expects component masses up to 50 $M_{\odot}$, mass

ratios in the range $0.3 < q < 1$, and aligned spins. The chemically homogeneous scenario predicts component masses in the range $\sim 20 - 50\,M_\odot$ and isotropic spins. It is thought that black holes aren't formed between $50 - 120\,M_\odot$ by supernovae. This is because when a star has a mass of $130 - 300\,M_\odot$, an oxygen-rich core is formed, explosive burning occurs, and the star is completely disrupted [40]. This mass region of $50 - 120\,M_\odot$, where no black hole exists, is called mass-gap. The dynamical interaction models predict isotropic spins and enable massive binaries. The primordial black holes models predict low spins and isotropic spin orientation. As introduced above, there are many scenarios for black holes, therefore, it is important to give them constraints by observing many events in the coming observation run.

In fact, before publishing GWTC-2, Advanced LIGO and Advanced Virgo have reported the cut off mass range $< 45\,M_\odot$ for component masses, and this criterion is compatible with the above theories. Furthermore, observation results in O1 and O2 also agree with the existence of the "lower mass gap" between $2.5 - 5\,M_\odot$, which has been believed so far [30].

However, the GWTC-2 reports several high-mass events such as GW190521, GW190602_175927, and GW190519_153544 for which component masses are much heavier than $45\,M_\odot$. Also, according to the GWTC-2, GW190814 had an accompanying compact object with $\sim 2.6\,M_\odot$, which is exactly within the lower mass gap. These results, summarized in the figure 2.7, force us to reconsider models for the distribution of black hole masses in the binary systems.

Especially for massive binary black holes, many theories do not explain their existence. Therefore, in parallel with theoreticians' work, we should increase statistics with many detections. For such events, the detector sensitivity at several dozens of Hz is very important as explained below.

When two compact objects are revolving in a circular orbit, in Schwarzschild geometry, the radius of an Innermost Stable Circular Orbit, $r_{\rm ISCO}$, can be derived as [41]

$$r_{\rm ISCO} = \frac{6G(m_1 + m_2)}{c^2}, \tag{2.58}$$

where G is the constant of gravitation, m_1 and m_2 are masses of objects, and c is the speed of light. When objects approach $r_{\rm ISCO}$ by decreasing the energy by gravitational wave radiation, the dynamics is dominated by strong field effects, and the Schwartzschild geometry is no longer applicable. Therefore, this is the time of coalescence and the end of the inspiral phase. At this moment, the merger frequency f_s approaches the value [41]

$$f_s = \frac{1}{6\sqrt{6}(2\pi)} \frac{c^3}{G(m_1 + m_2)}. \tag{2.59}$$

Here Kepler's third law was used. According to equation (2.59), the merger frequencies for $50\,M_\odot - 50\,M_\odot$ and $100\,M_\odot - 100\,M_\odot$ are given as 22 Hz and 11 Hz (see figure 2.8). Therefore, better detector sensitivity at low frequencies enables to impose stronger constraints to the theory.

2.5.2 Test of general relativity

General relativity has been verified through various experiments. Beginning with the gravitational lensing effect by Eddington, it has been proven through various cosmic observations, such as the perihelion shift of the orbit of Mercury and the orbital decay of PSR 1913+16 [42]. The validity of general relativity has also been derived by measuring the difference in gravitational potential with extremely high precision optical lattice clocks [43].

Gravitational waves are also the best event to directly test general relativity. Especially in the strong gravitational field, the gravitational-wave is the only way to test general relativity. Reference [44] presents eight ways to verify them. It says that there is no inconsistency between general relativity and all eight validation tests to the detected events during O1 to O3a. These verifications require precise observations from the inspiral phase to the coalescence and quasi-normal mode. Conventionally, we have been considering binary neutron stars with several solar mass for long time, but the recent observations clearly show that number of black holes with several dozens solar mass is much large. As mentioned in section 2.5.1, gravitational waves from these binaries are in the frequency range of tens to hundreds of Hz from inspiral to quasi-normal mode. Although laser interferometric detectors have the best strain sensitivity in the hundreds of Hz, it is now necessary to observe the gravitational waves especially in the low-frequency region with high accuracy.

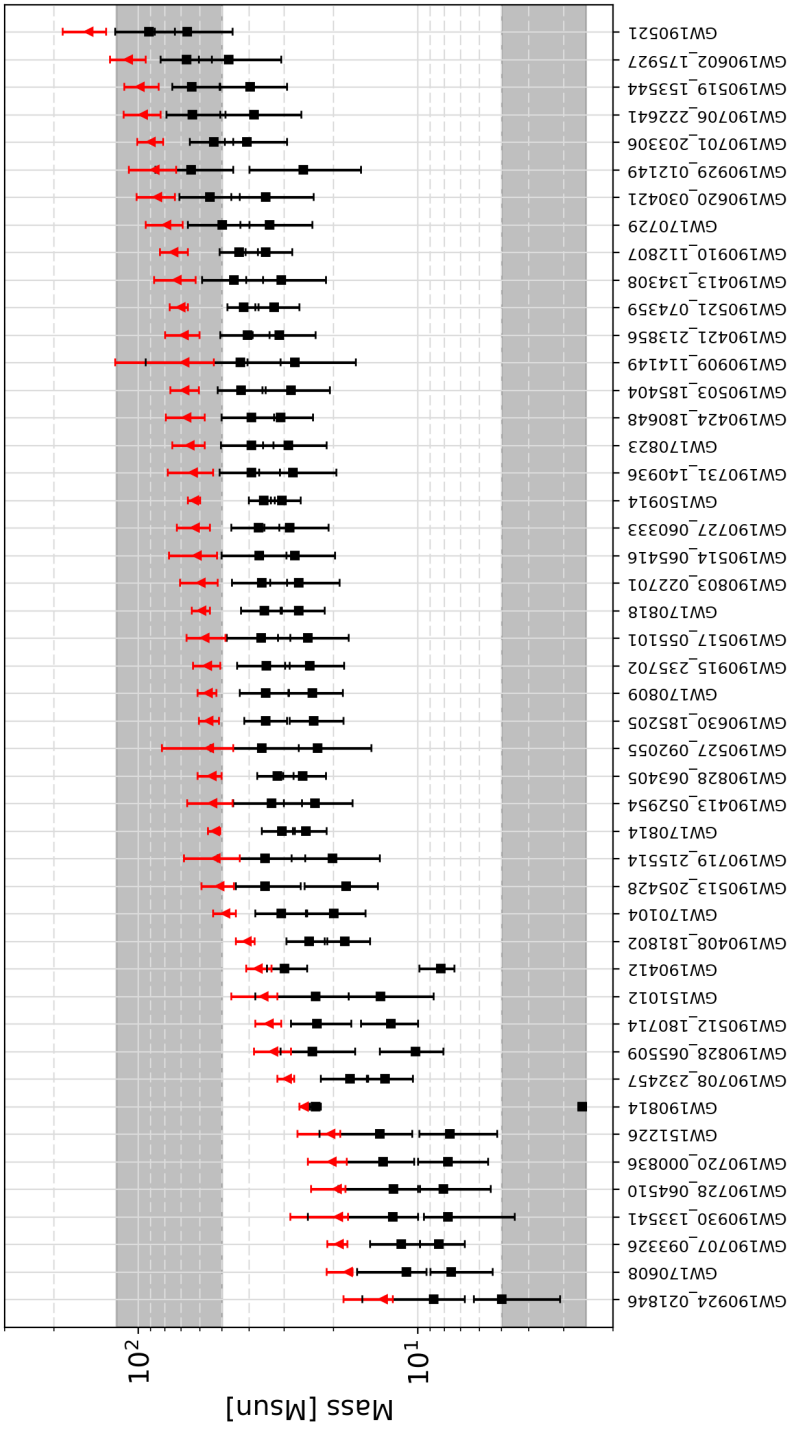

Figure 2.7: Summary of detected black hole events. In each column, two black squares represent masses of the component masses and a red triangle represent mass after the merger. Upper and lower grey zone represent mass-gap and lower mass-gap regions, respectively.

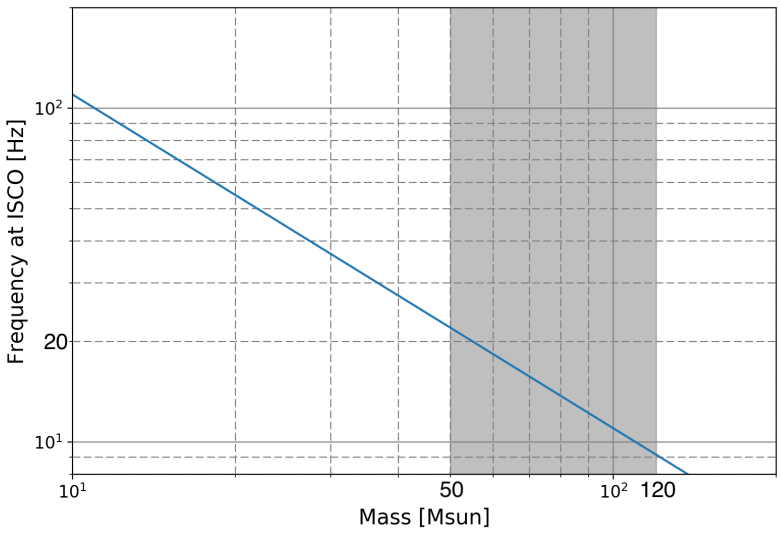

Figure 2.8: Relationship between the mass and merger frequency. Horizontal axis represents mass of a component object when equal-mass binary is assumed. Grey zone shows mass-gap region.

Chapter 3
LARGE-SCALE CRYOGENIC GRAVITATIONAL WAVE TELESCOPE KAGRA

Although KAGRA is the third km-scale interferometric gravitational wave detector in the world, it has two advanced features: an underground site and a cryogenic mirror. This chapter first briefly overviews the KAGRA detector, then introduces detail of the suspension system for the cryogenic mirror, and finally explain apparatus for mirror cooling.

3.1 Overview of KAGRA

This section overviews the detector configuration of KAGRA and its role in the international gravitational wave observation network.

3.1.1 Detector configuration

The Large-scale Cryogenic Gravitational wave Telescope KAGRA was constructed in the Kamioka mine (Mt.Ikenoyama). All the equipments are placed in the underground tunnel, and the vacuum system occupies most part of it: vacuum ducts with 800 mm in diameter are installed in two arms, and dozens of vacuum chambers are placed at the end and corner stations. An underground site was chosen to reduce seismic noise and this is one of the most advanced attempts in KAGRA. Another advanced key feature in KAGRA is the 20 K cryogenic mirror to reduce thermal noise, which limits the most sensitive frequency region in the ground-based interferometric gravitational wave detector. Since thermal noise is

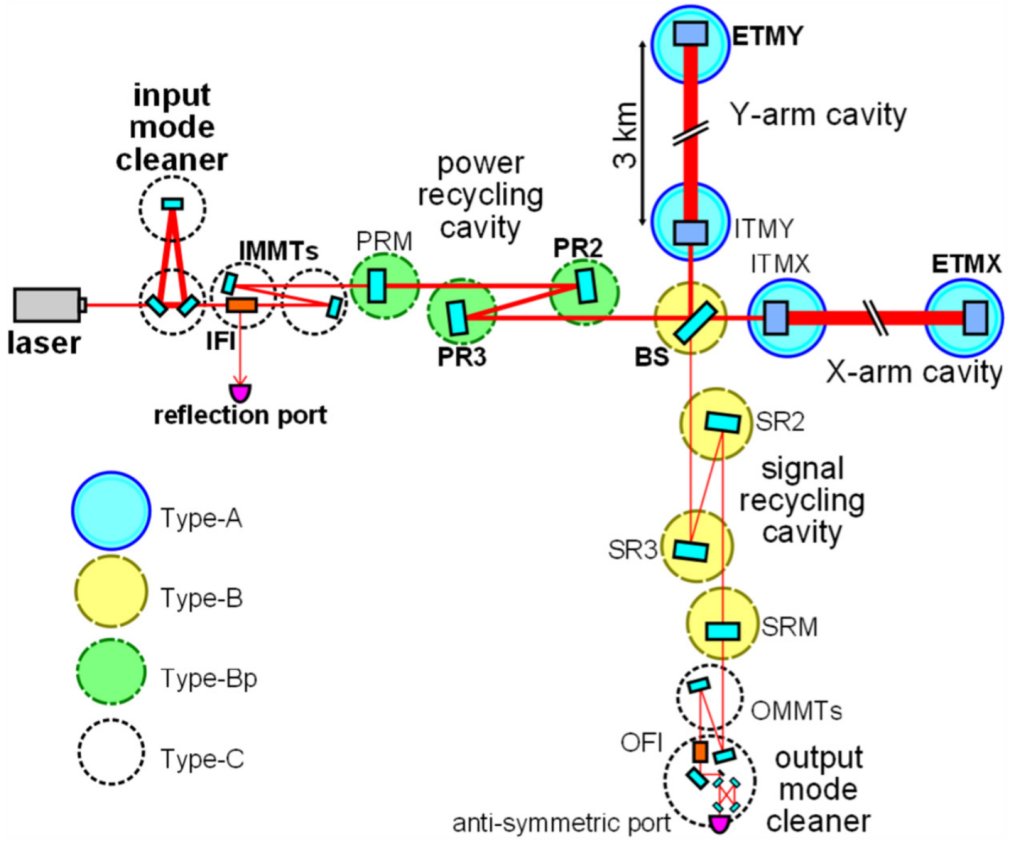

Figure 3.1: Optical layout of KAGRA [12]. At the corner section, a main laser source, Input Mode Cleaner (IMC), and Input Mode Matching Telescope (IMMT) are installed in the most upstream region. The Power Recycling (PR) system, Beam Splitter (BS), and Signal Recycling (SR) system are installed at center of the corner area. Output Mode Matching Telescope (OMMT) and Output Mode Cleaner (OMC) are installed in the most downstream region. In arms, sapphire Test Masses (ITMX, ETMX, ITMY, ETMY) are installed.

proportional to product of temperature and loss angle as explained in section 2.3.3, decreasing temperature gives a large advantage to reduce it.

The design optical configuration of KAGRA is the Dual Recycled Fabry-Perot Michelson Interferometer (DRFPMI) as shown in figure 3.1. It is the Fabry-Perot Michelson Interferometer adopting power and signal recycling systems. All the blue rectangles in figure 3.1 represent mirrors to constitute the DRFPMI, the cryogenic mirrors are four mirrors that constitute the Fabry-Perot cavity in x-

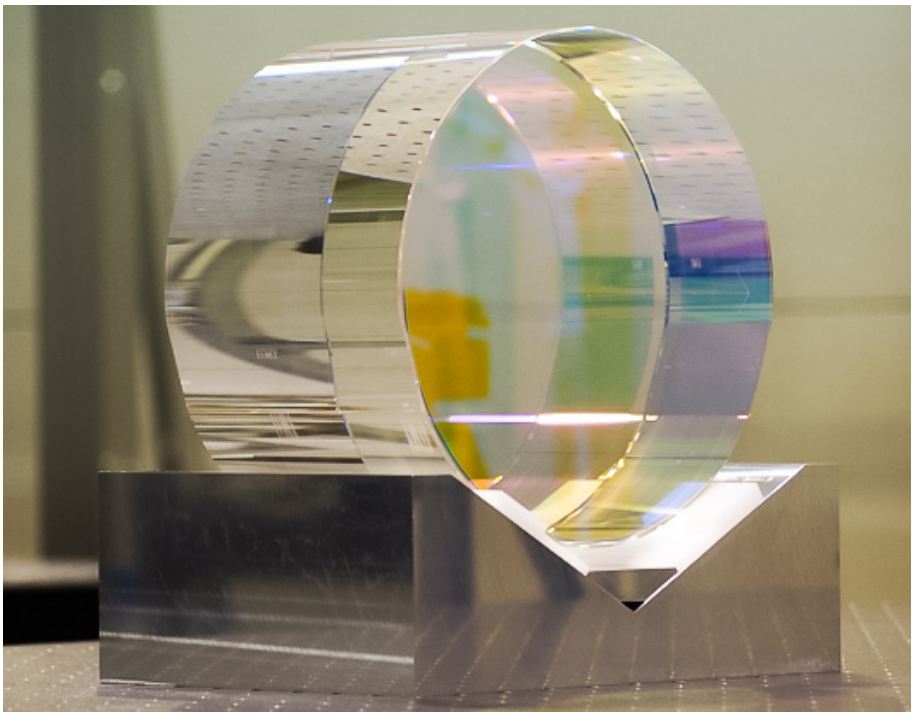

Figure 3.2: Photo of the KAGRA sapphire mirror. It is 220 mm in diameter, 150 mm in thickness, and 23 kg in weight and made of artificial monocrystal sapphire. The dielectric multilayer coating is on the surface [45].

and y-arms. They are made of artificial monocrystal sapphire with 220 mm in diameter, 150 mm in thickness, and 23 kg in weight (see figure 3.2). Other mirrors are made of fused silica and operated at room temperature.

3.1.2 Sensitivity

The design sensitivity of KAGRA is shown in figure 3.3 [46]. Low-, intermediate-, high-frequency regions are dominated by suspension thermal and quantum noises, quantum and mirror thermal noises, and quantum noise, respectively. When KAGRA joins the international gravitational wave observation network with the design sensitivity and enables four detectors observation, sky localization will be improved to be about ten square degrees: it was hundreds to thousands and tens to hundreds of square degrees for two and three detectors, respectively. This improvement is significantly important for an accurate alert to the optical telescopes for multi-messenger astronomy.

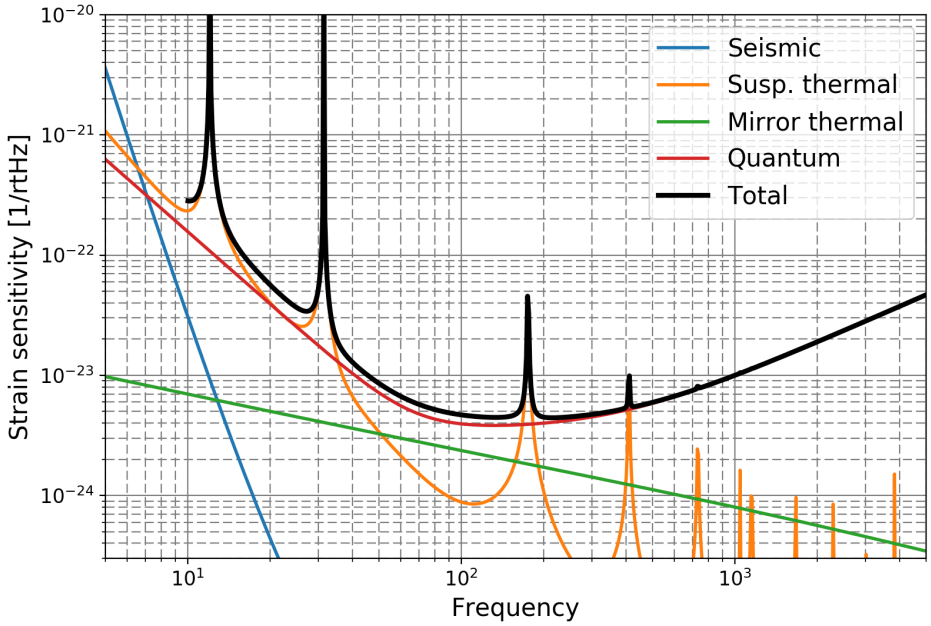

Figure 3.3: KAGRA design sensitivity [46]. Blue, orange green, and red colored lines represent the seismic noise, suspension thermal noise, mirror thermal noise, quantum noise. Black line shows the total of these noises.

The merger rate of binary black holes is estimated to be $23.9^{+14.9}_{-8.6}\,\mathrm{Gpc}^{-3}\mathrm{yr}^{-1}$ [31], however, all the events cannot be detected because the duty factors of detectors are not 100 %. Furthermore, at least three detectors are necessary for accurate sky localization. Assuming unplanned downtime periods, it is calculated that the duty factor in a three-detector network (LIGO Hanford, LIGO Livingston, and Virgo) is operated in coincidence approximately $34-42\,\%$ of the time. If KAGRA joins this detector network, the duty factor with three or more detectors will be improved to be around $65-74\,\%$ of the time [8].

3.2 Seismic attenuation system for the test mass

The seismic noise is reduced by constructing the detector underground, however, vibration level is still large to detect gravitational waves. Therefore, the test masses are suspended by pendulums to isolate ground vibration. This section briefly reviews seismic noise and its attenuation system for test masses.

3.2.1 Seismic motion

Seismic motion is divided into two types: cultural noise ($> 1\,\mathrm{Hz}$) and natural noise ($< 1\,\mathrm{Hz}$) [26,47]. It seems that the cultural noise is mainly caused by human activities such as traffic, factory, footsteps, etc... The frequency band of these activities overlapes with the observation frequency band so we have to consider these sources very carefully. On the other hand, the natural noise originates from ocean waves, air pressure, and earth tides, etc. This low frequency noise strongly depends on the location. By detailed site study, KAGRA was constructed under Mt.Ikenoyama; vibration level of Kamioka site is about two orders of magnitude lower than urban area as shown in figure 3.4.

3.2.2 Seismic attenuation system

Simply, the movement of the test mass has to be smaller than the effect of gravitational waves. As shown in figure 3.4, vibration level of Kamioka site is order of $10^{-10}\,\mathrm{m}/\sqrt{\mathrm{Hz}}$ at $10\,\mathrm{Hz}$, while KAGRA requires the displacement sensitivity of order of $10^{-18}\,\mathrm{m}/\sqrt{\mathrm{Hz}}$ at $10\,\mathrm{Hz}$. Therefore, the high performance vibration isolation system is necessary for KAGRA.

The seismic attenuation system for the test mass is a 13.5-m tall multi-stage pendulum, which is called Type-A suspension. The Type-A suspension has 9-stages; the upper 5-stages are at room temperature and called Type-A Tower, the lower 4-stages are at cryogenic temperature and called Cryogenic Mirror Suspension or Cryopayload. While other optics are suspended from the rigid tower structures built on the first floor, Type-A suspension is suspended from the second floor of the tunnel. This approach enables to eliminate resonances of the tower structure. Furthermore, it contributes to increasing the stability of the interferometer operation because a pair of Type-A suspensions in each arm move commonly with the bedrock of Mt.Ikenoyama.

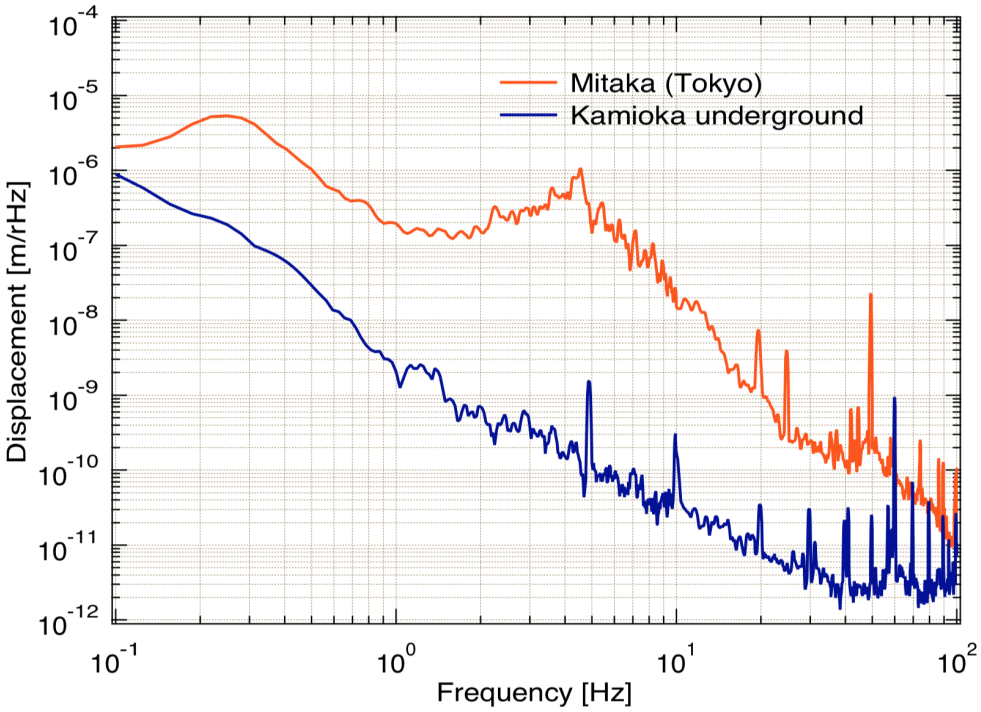

Figure 3.4: Comparison of vibration level between Kamioka site and Mitaka [16]. Small seismic level relaxes the requirement for the vibration isolation systems.

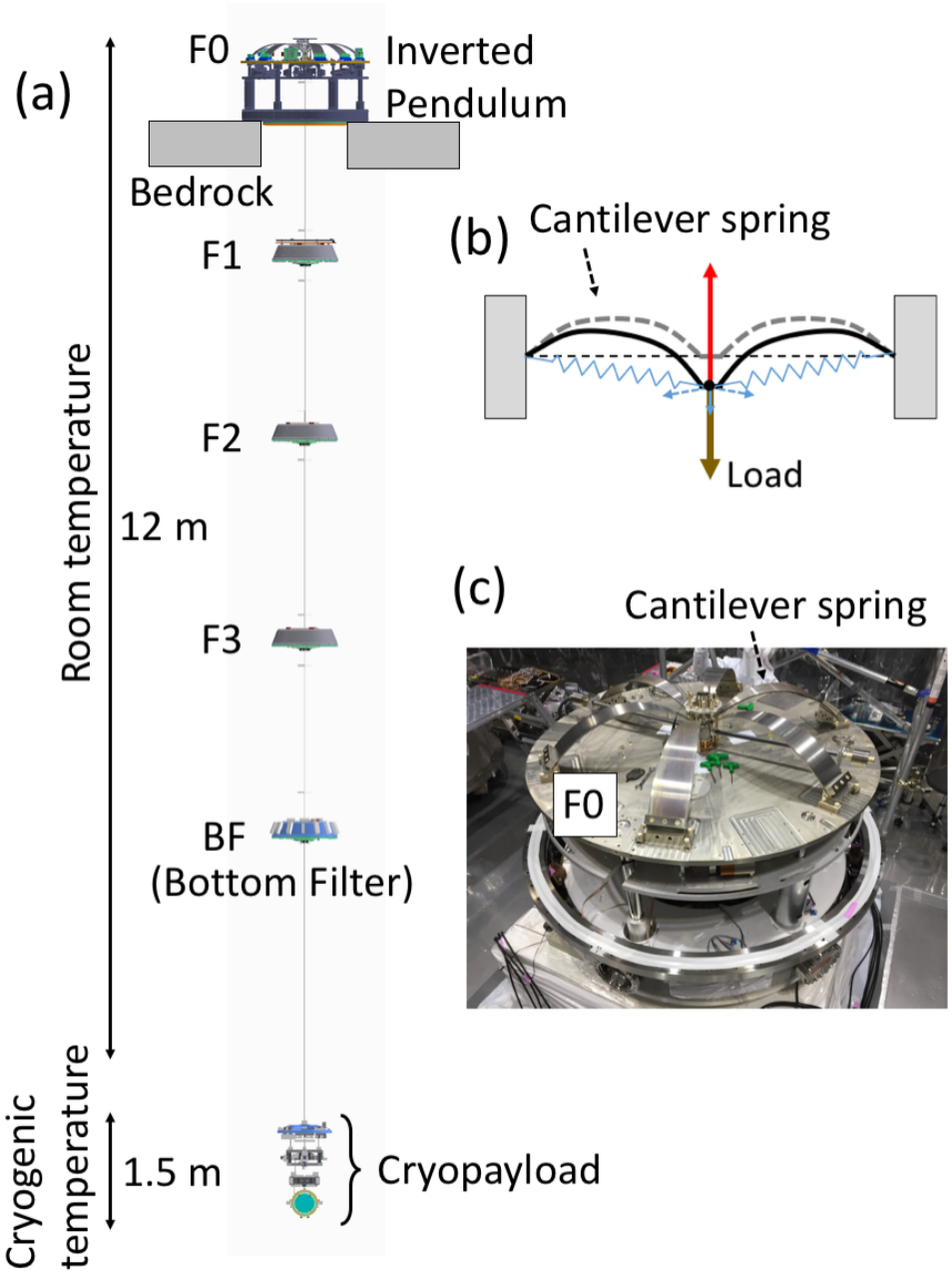

Figure 3.5: (a): Overview of Type-A suspension. Type-A suspension is mounted on the bedrock. There are five stages of GAS filter from F0 to BF. Cryopayload is the bottom most part (1.5 m). (b): Schematic view of the GAS filter. A set of cantilever springs are compressed together to achieve low frequency in the vertical direction. Blue springs represent the spring composition for the compressed direction; while the horizontal composition cancels each other out, the vertical composition remains when the center part move up and down [48]. (c): A photo of the F0 [49]. Six blades in total are compressed together.

3.2.3 Cryogenic mirror suspension

Cryogenic mirror suspension (or cryopayload) consists of four stages [50]: Platform (PF), Marionette (MN), Intermediate Mass (IM), and Test Mass (TM) as shown in figure 3.6. Except for the Platform stage, the Recoil Mass surrounds each stage: Marionette Recoil (MNR), Intermediate Mass Recoil (IMR), and Test Mass Recoil (TMR). A series chain from TM to MN is called Test Mass chain (TM chain), and the one from TMR to MNR is called Recoil Mass chain (RM chain). Total mass of the cryopaylaod is 200 kg. Test Mass and Recoil Mass chains have magnets and coils, respectively, to constitute coil-magnet actuators for suspension damping and interferometer operation. Details of each stage are explained below.

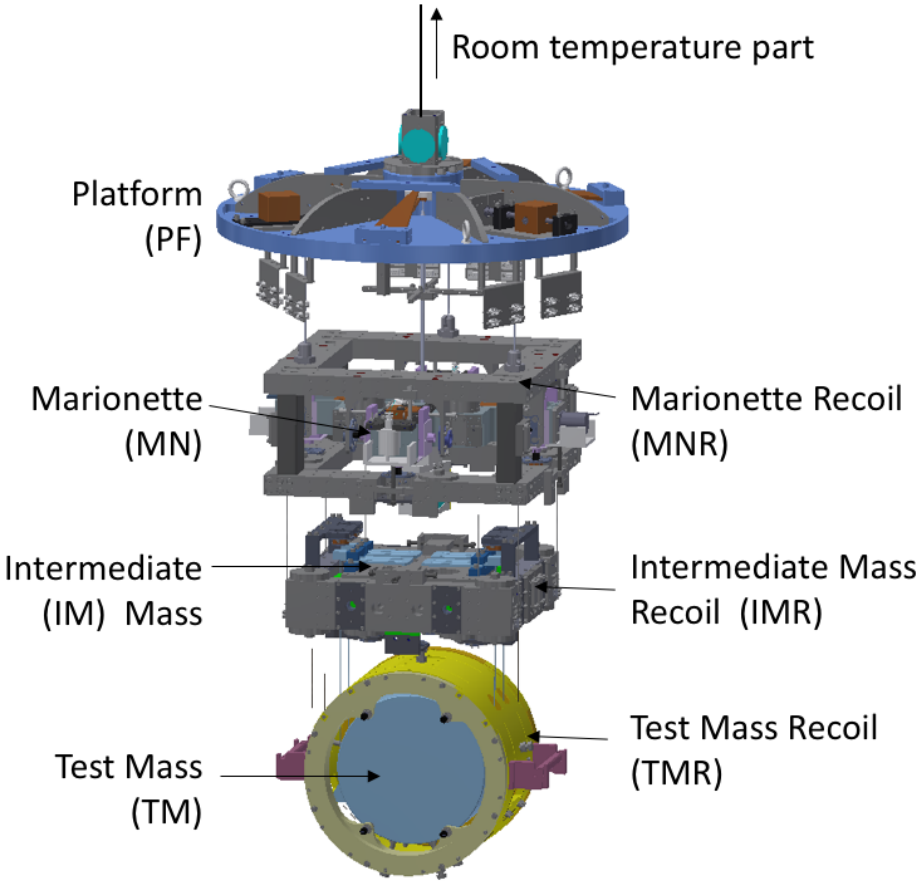

Figure 3.6: 3D view of Cryopayload.

Platform

Platform (figure 3.7) is located on the top of the cryopayload and connected with the Bottom Filter, which is the last stage of the room temperature part, with a 3.3-m rod made of Maraging steel (see figure 3.5). The Platform suspends both of Test Mass and Recoil Mass chains.

The TM chain is suspended from the point of intersection of three cantilever blade springs made of copper berylium with about 4 Hz resonance for the fundamental mode. These blades work for vertical vibration attenuation. To rotate whole the RM chain, the moving mass systems is installed.

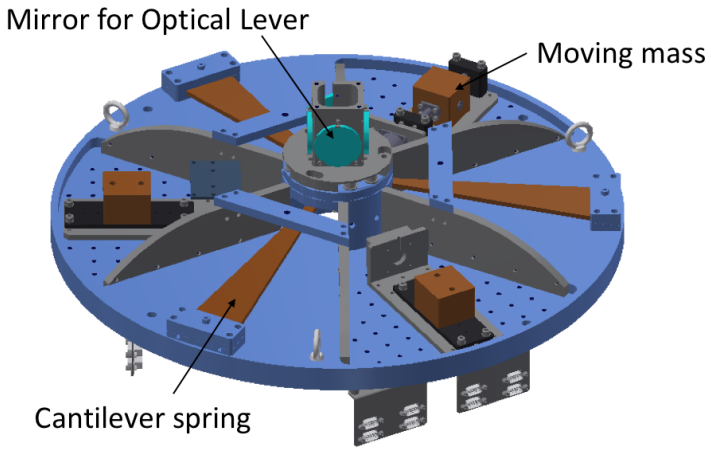

Figure 3.7: Platform. Three cantilever springs made of copper berylium are merged at the center and suspend TM chain with one rod. Mirrors for the optical lever are also installed.

Marionette

Marionette (figure 3.8) is located one stage under the Platform. It has + shape structure with the moving mass systems for rough inclination adjustments of the IM and TM stages [51]. KAGRA tunnel has 1/300 inclination to drain spring water so that X-end TM reflects the laser beam upwards and Y-end TM reflects it downwards. MNR is the first place where the heat links from the

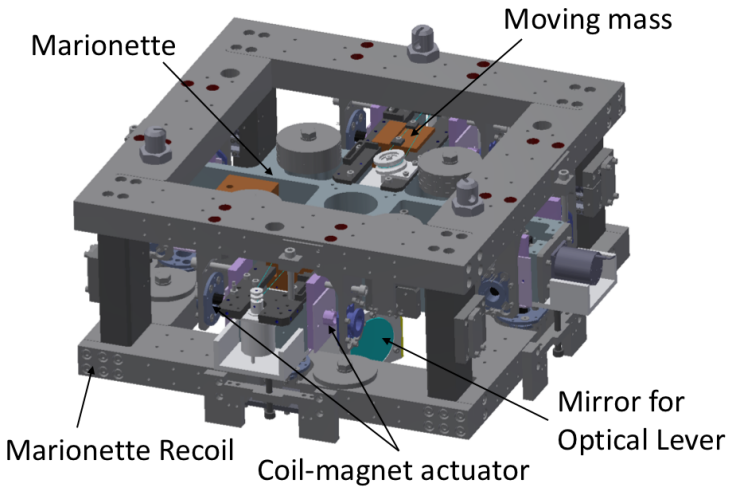

Figure 3.8: Marionette. In order to align the inclination of the TM, the moving mass systems are installed in the + shape arms. A mirror for the optical lever is mounted under MN.

cooling bar are attached as shown in figure 3.13,

Intermediate Mass

Intermediate Mass (figure 3.9) is the second last stage of the cryopayload. Four folded-blade springs made of sapphire are mounted on the IM to suspend the TM.

Test Mass

Test Mass (figure 3.10), or just mirror, is located at the bottom of the cryopayload. Sapphire has significant characteristics at cryogenic temperature: very low mechanical loss and very high thermal conductivity. The dielectric multilayer coating is coated on the surface [45].

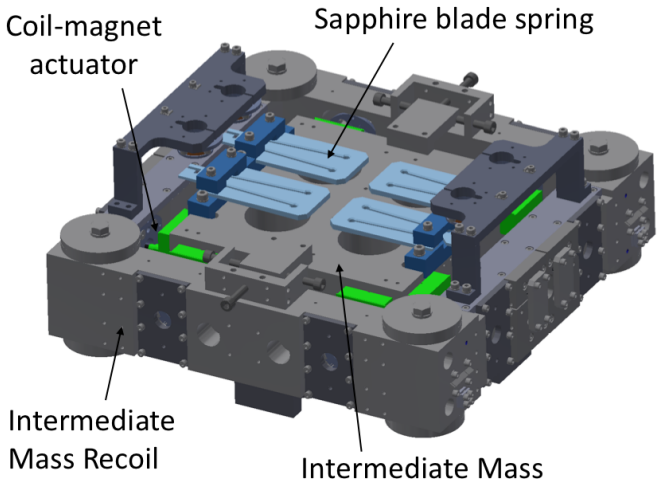

Figure 3.9: Intermediate Mass. Sapphire blade springs suspend the TM with sapphire fibers and also are the cooling path for the TM.

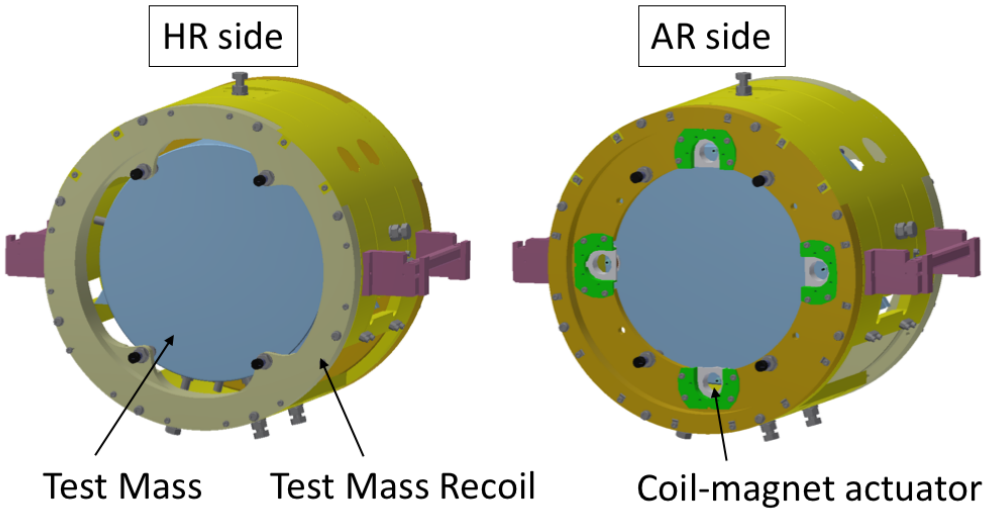

Figure 3.10: Test Mass. HR (High Reflection) side reflects laser beam. There are coil magnet actuators on the AR (Anti Reflection) side. For the Recoil mass, very low magnetism stainless steel NSSC130S is used.

3.2.4 Sapphire suspension

The sapphire suspension (figure 3.11) is a part of the cryopayload. In order to reduce thermal noise, the TM and parts near the TM are made by sapphire. Main components are sapphire blade spring, sapphire fiber, and sapphire Test Mass. Sapphire blade springs have two roles: to lower the resonant frequency of the vertical stretching mode, and to compensate for the difference in fiber lengths. Roles of the sapphire fibers are both suspending the TM and extracting heat from the TM. Since 0.724 W of heat input is estimated into Input Test Mass (ITM) for design configuration of KAGRA [46], sapphire fiber has a diameter of 1.6 mm and a length of 350 mm long to extract heat input. To make good surface contact between the sapphire blade spring and the nail head of the fiber, gallium bonding technique is used to bond them together. Besides, since the TM is cylindrical in shape, two sapphire ears are bonded on the side by making flat surfaces on the TM. Hydroxide Catalysis Bonding (HCB) was used for the ear bondings because it has smaller thickness and high shear strength at cryogenic temperature[‡1] [52, 53].

[‡1] All the HCBs were carried in the clean booth in University of Toyama with large technical supports by University of Perugia and University of Glasgow. I was one of the core members for this work.

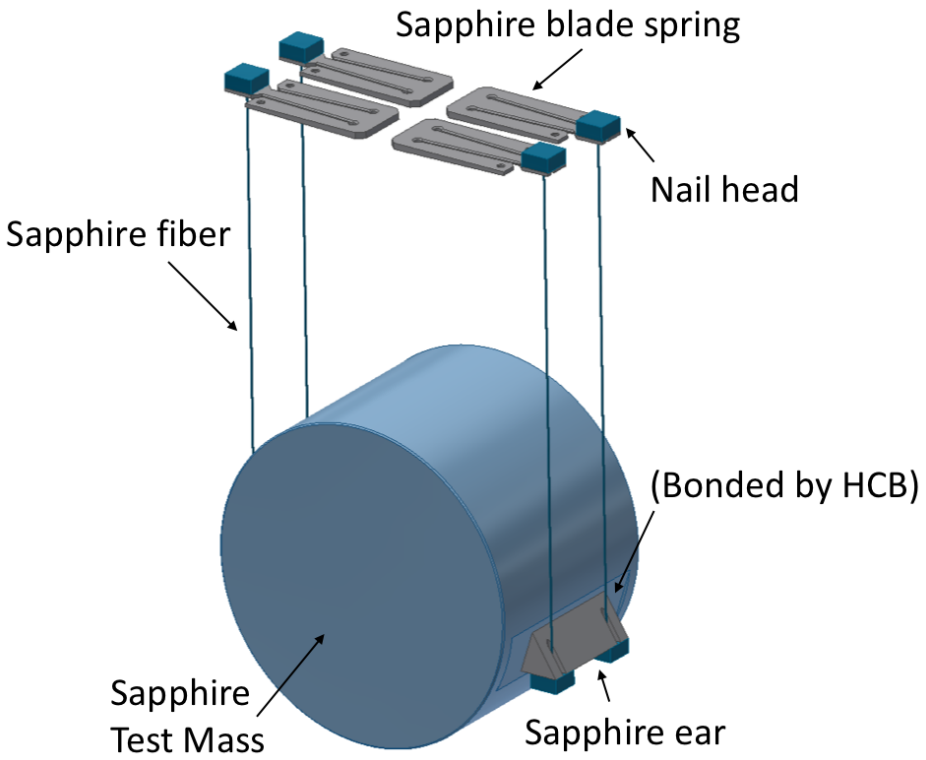

Figure 3.11: Overview of the sapphire suspension. The Test Mass is suspended by four sapphire fibers (1.6 mm in diameter and 350 mm in length). There is a nail head at each end of the fiber. Gallium bonding technique is used to bond the blade spring and nail head of the fiber. Hydroxide Catalysis Bonding is adopted to attach sapphire ears on the flat cuts of the TM.

3.3 Cooling systems

This section briefly reviews the cooling system for the cryopayload: low-vibration cryocooler, cryostat, and cryogenic duct shield.

3.3.1 Cryocooler

Nowadays, two types of cryocoolers are widely, and commercially available: Gifford-McMahon (GM) cryocooler [54] and pulse tube (PT) cryocooler [55]. Both cryocoolers achieve refrigeration with rotary valves that switch the cold head between a low- and high-pressure source [56]. A big difference between the GM and PT cryocoolers is displacer; while the displacer moves as a substantial piston to exchange working gas in the GM, working gas itself works as a "gas piston" in the PT. Therefore, the PT cryocooler has no oscillating mass in the cryogenic part. Thanks to this feature, the PT cryocooler has smaller vibration than the GM, and it is preferable for the gravitational wave detector.

KAGRA's 4 K PT cryocooler has novel mechanisms to further reduce working vibration [57-59]. The concept of development is to fix a cryocooler rigidly onto the bedrock (see figure 3.12). As shown in figure 3.4, the vibration level of the Kamioka site is very small, so if we can fix the cryocooler and its cold heads to the massive and stable bedrock, we can expect to suppress the vibration of the cryocooler. Since it is difficult to reduce the vibration of cold heads themself, vibration reduction (VR) stages, which are rigidly fixed onto the floor but thermally isolated from it, are installed. Each cold head and VR stage are connected with flexible heat links.

3.3.2 Cryostat

A cryostat is a vacuum chamber to cool down the sapphire test mass. In contrast to other large-scale cryogenic systems such as an accelerator, KAGRA does not use any cryogen. This is to reduce maintenance work and to operate in a turn-key style. Also, the KAGRA tunnel has very limited volume so that choking gas should be inappropriate. On the other hand, four mechanical cryocoolers are used effectively for cooling. They are the pulse tube cryocoolers, which are specialized to reduce the working vibration as explained in section 3.3.1.

As shown in figure 3.13, all the first stages of the four PTs are connected to the the outer radiation shield. Two second-stages of the four are connected to

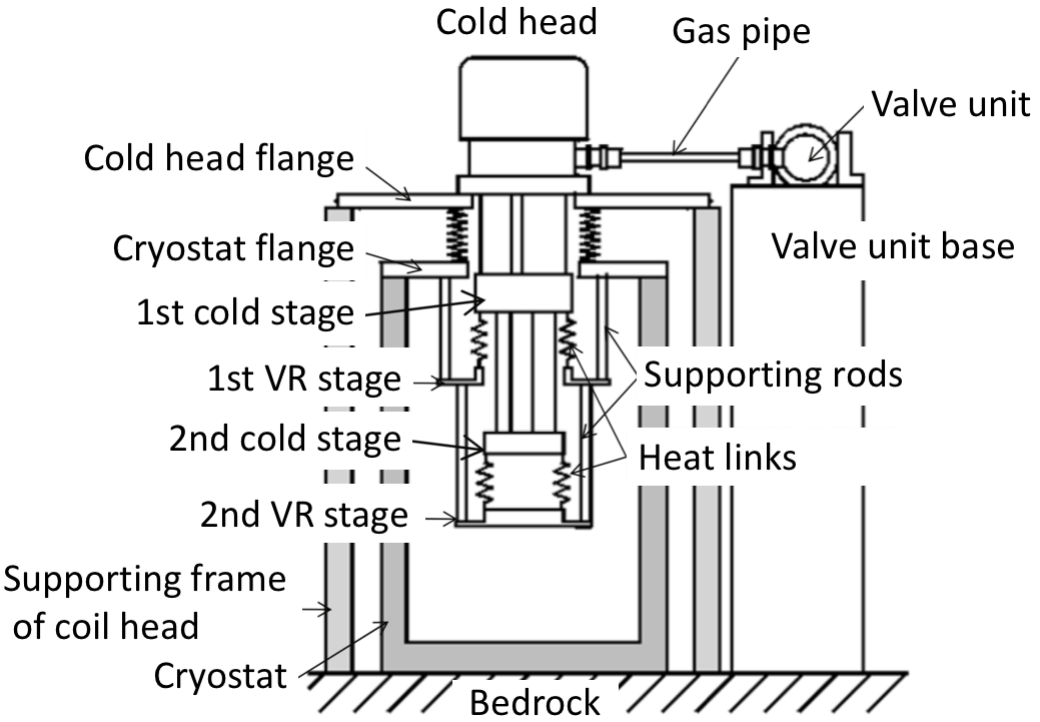

Figure 3.12: Schematic view of low vibration pulse tube cryocooler for KAGRA (reference [59] was modified). Valve unit is separated from the cold head. The vibration reduction (VR) stages are fixed to the bedrock via supporting structures.

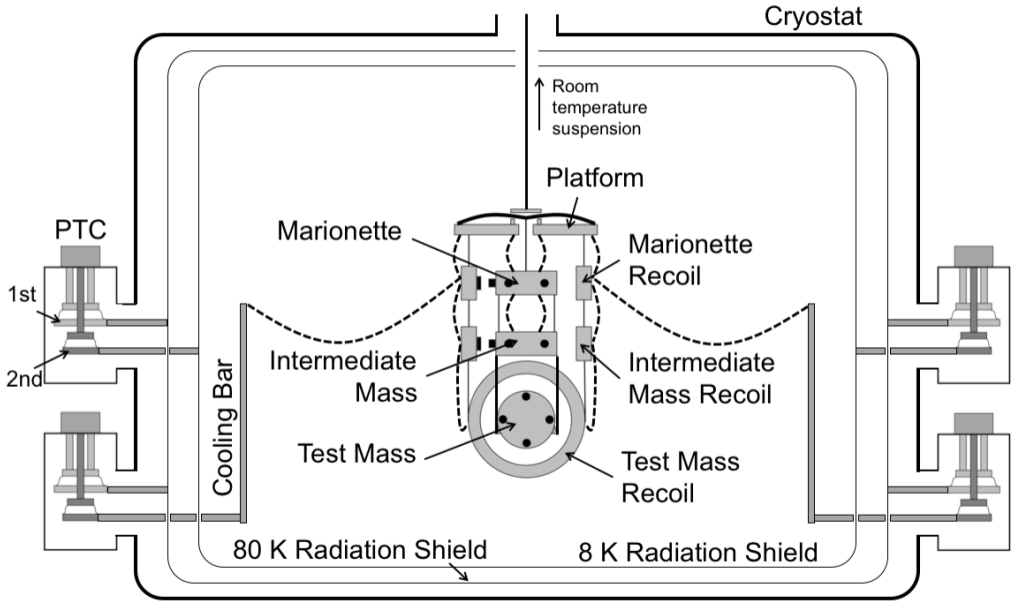

Figure 3.13: Schematic view of the cryostat. Four cryocoolers are used in total. Black broken lines represent the heat links. The heat links connects between the cooling bar and Marionette Recoil.

the inner radiation shield. Remaining two second-stages are connected to the cryopayload for conductive cooling.

In KAGRA, radiation shields work not only for shutting out 300 K thermal radiation but also for thermal radiative cooling of the cryopayload. To assist radiative cooling, inner surface of the inner shield is coated by Diamond Like Carbon (DLC) coating [60, 61]. Radiation shields have supporting structures from the cryostat chamber, which is designed to be rigid at cryogenic temperature by considering thermal shrink of the rods. In order to extend cooling path from the conductive-cooling-cryocooler, a cooling bar is attached at the end. The cooling bars are rigidly connected to the radiation shield with stainless steel bolts.

3.3.3 Cryogenic duct shield

In the common sense of the cryostat, it is natural to completely cover an object with cold surrounding shields, however, there are two large holes in front and back side of the KAGRA cryostat for the laser path. These apertures are one of the difficulties for the cooling of the cryopayload since 300 K thermal radiation is tremendously large. One solution to reduce thermal radiation from there is to install cryogenic duct shields and baffles in front of both sides of the cryostat. In order to minimize the reflection of radiation, five baffles are installed for one side, and baffles and inner surface of the duct shields are coated by Solblack coating [62]. A cryogenic duct shield is cooled down with one stage pulse tube cryocooler. According to past work, a cryogenic duct shield reduces 300 K thermal radiation to 0.1 W for one side [13]. It was also reported that heat input into the Test Mass stage by thermal radiation from apertures were estimated as 50 mW in total [13].

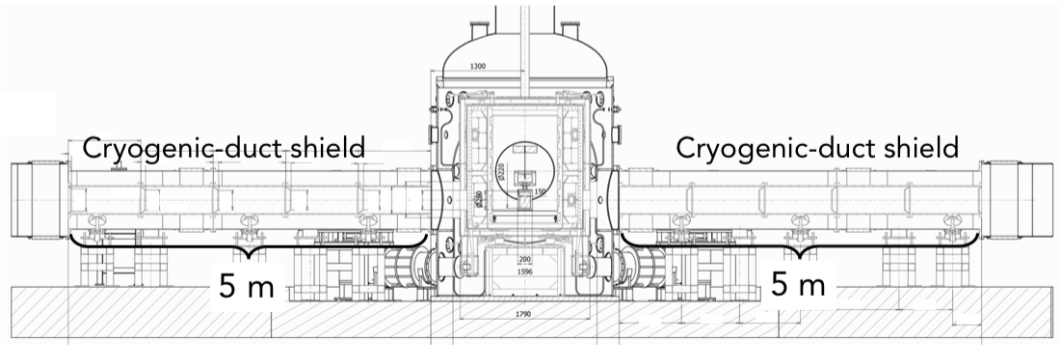

Figure 3.14: Side view of the cryostat and cryogenic duct shield. A cryogenic duct shield is 5 m long and has five baffles [13]. Baffles and inner surface of the duct shields are coated by Solblack coating [62].

Chapter 4
SUSPENSION COOLING AND HEAT LINK

Sapphire Test Mass has to be cooled down quietly to achieve an excellent detector sensitivity and effectively to reduce observation dead time. In this chapter, cooling scheme for the cryopayload, detail of the heat link and its material properties, and a potential problem in the suspension cooling are reviewed. At last, the target of the study is stated.

4.1 Suspension cooling

Thermal radiative cooling and thermal conductive cooling are utilized for suspension cooling. This section briefly overviews cooling scheme and describes a potential problem.

4.1.1 Thermal radiative cooling

Thermal radiation is the emission of electromagnetic waves whose wavelength depends on the temperature. No mediating substances are needed. Heat transfer by thermal radiation from objects 1 to 2, P_{Rad}, is expressed as [63]

$$P_{\mathrm{Rad}} = \frac{\sigma}{\frac{1}{\varepsilon_1} + \frac{A_1}{A_2}\left(\frac{1}{\varepsilon_2} - 1\right)} A_1 (T_1^4 - T_2^4), \tag{4.1}$$

where A, T, ε, and σ are surface area, temperature, emissivity, and Stefan-Boltzmann constant.

In KAGRA, objects 1 and 2 are considered as the cryopayload and inner radiation shield, respectively. Since equation (4.1) means that thermal radiative

heat transfer is proportional to $(T^4_{\rm payload} - T^4_{\rm shield})$, the radiation shield is quickly cooled down to assist thermal radiation in KAGRA. Two pulse tube cryocoolers are assigned for this purpose. In order to further assist thermal radiation, KAGRA cryogenic system adopts black coatings to increase emissivity. Three types of black coatings are currently used: Diamond Like Carbon (DLC) coating [61], Solblack coating [62], and low-magnetism Solblack coating [64]. DLC is adopted for the inner surface of the inner radiation shield because it has a very low outgassing rate. Solblack is adopted for the cryogenic duct shield and Wide Angle Baffle (WAB)[‡1]. Low-magnetism Solblack is adopted for the cryopaylaod. Solblack family is a chemically-treated nickel plating, so it is possible to coat large parts, which are difficult to be coated by DLC. Photos of DLC and low-magnetism Solblack coatings in the KAGRA cryogenic system are shown in figure 4.1.

4.1.2 Thermal conductive cooling

Thermal conduction takes place via heat carriers in the medium. Heat transfer by thermal conduction from objects 1 to 2, $P_{\rm Cond}$, is expressed as [63]

$$P_{\rm Cond} = -\frac{S}{l}\int_{T_1}^{T_2} \kappa(T){\rm d}T, \tag{4.2}$$

where S, l, and $\kappa(T)$ is cross-sectional area, length, and thermal conductivity of the heat conductor. As an indicator of the ease of heat transfer, thermal resistance R_θ is introduced, which is defined as

$$R_\theta = \frac{\Delta T}{P}, \tag{4.3}$$

where ΔT and P are the temperature difference and heat flow. High thermal resistance means that it is difficult for heat to flow. When the temperature difference between T_1 and T_2 is small in equation (4.2), that allows linear approximation for thermal conductivity κ, equation (4.2) is changed to

$$P_{\rm Cond} = \frac{S}{l}\kappa_0(T_1 - T_2), \tag{4.4}$$

where κ_0 is constant thermal conductivity at the intermediate temperature $(T_1 - T_2)/2$. Therefore, the thermal resistance of the heat conductor can be expressed

[‡1]WAB is placed in front of the Test Mass to absorb scattered light on the HR surface. It is cooled down at cryogenic temperatures.

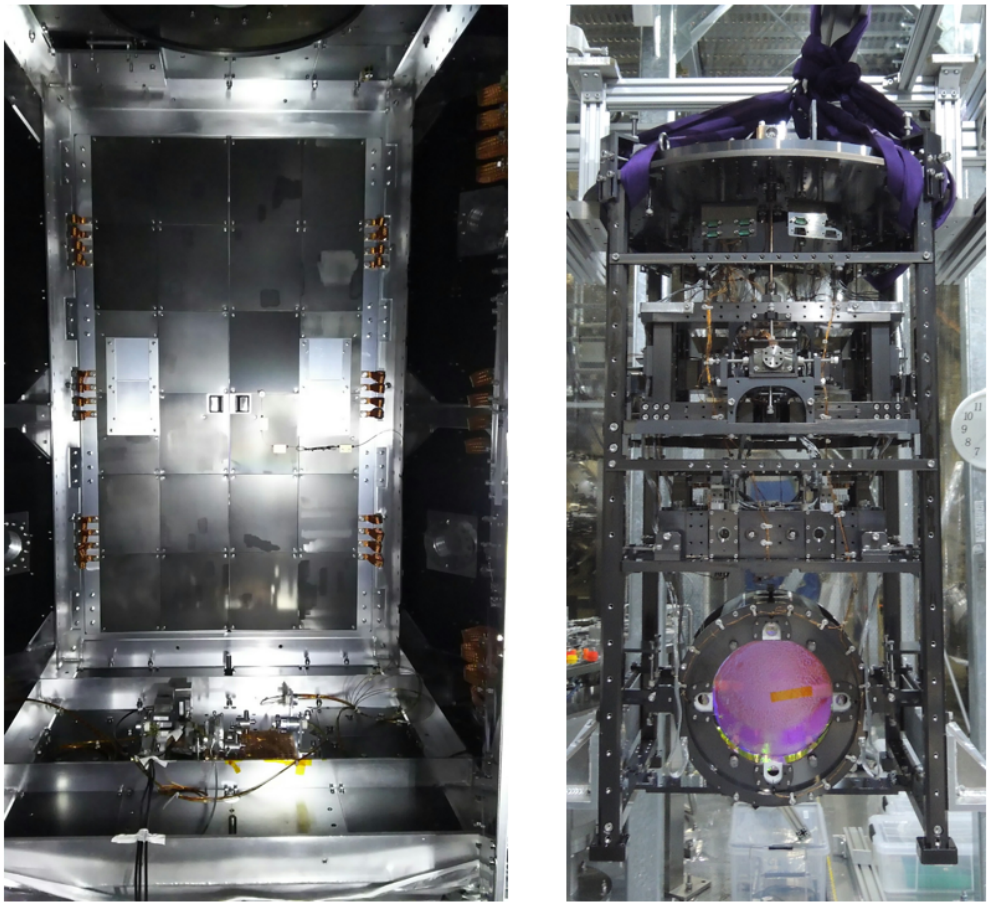

Figure 4.1: (a): DLC coated inner radiation shield. (b): Low-magnetism Solblack coated cryopayload.

as

$$R_{\mathrm{Cond}} = \frac{l}{S\kappa_0}. \tag{4.5}$$

Equation (4.5) indicates that the heat conductor should have a short length and large cross-sectional area for effective thermal conduction. However, these characteristics assume a rigid connection, this is completely opposite request from the viewpoint of suspension cooling in KAGRA because the Test Mass needs to be cooled down very quietly.

4.1.3 Cooling concept and potential problem

Cryopayload must be cooled as quiet as possible. Thermal radiation is preferable in this sense because it is non-contact cooling. However, according to equation (4.1), it will be ineffective when the cryopayload is at cryogenic temperature, which is typically below 100 K. On the other hand, pure metals such as high purity aluminum and oxygen-free copper have large thermal conductivities at cryogenic temperature [65-68]. They can compensate for heat extraction at cryogenic temperature instead of thermal radiation. Therefore, cooling concept of the cryopayload is "thermal radiation at high temperature and thermal conduction at low temperature".

Relationship between cooling method and practical situation is organized in figure 4.2. The TM is vibration-isolated by room temperature part, and only the cryopayload is cooled down to cryogenic temperatures by connecting the heat conductors. There is a large problem here, that is, these heat conductors are connected to the *vibration-isolated stage*. They become a shortcut of vibration inflow and may shake the TM above the displacement noise requirement of KAGRA. Source of vibration is not only seismic vibration but also vibration of cryocooler, cryostat, and radiation shields.

In order to reduce vibration inflow as much as possible, the stiffness of the heat conductor has to be small while keeping thermal conductance; a soft and high thermal conductive heat link is necessary. Therefore, we first developed an appropriate heat link, and measured its thermal and mechanical properties. We have then evaluated the thermal performance by a cooling test in KAGRA, and calculated the effect of vibration inflow via heat links to the detector sensitivity.

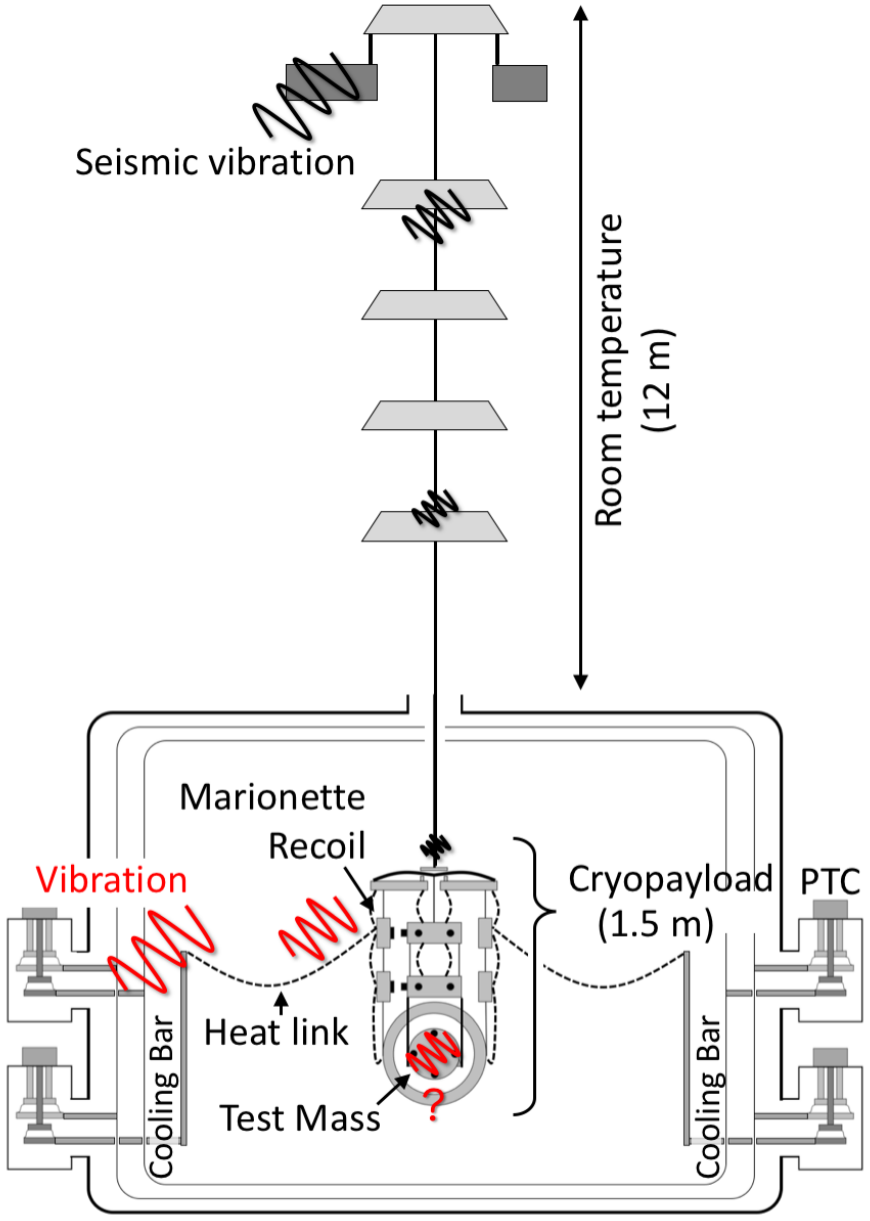

Figure 4.2: Schematic view of relationship between Type-A suspension and the heat link. Seismic vibration (black zigzag) from the top is sufficiently attenuated by room temperature part. The heat link becomes shortcut for vibration inflow (red zigzag) and may shake the Test Mass above the displacement noise requirement of KAGRA

4.2 Heat link

The heat link currently used has been developed for KAGRA. This section explains the detail of the heat link and reports several measurement results.

4.2.1 Overview of heat link

The heat link is required to have high thermal conductivities at cryogenic temperatures. High purity aluminum and oxygen-free copper were considered as candidate materials [65-68]. The heat link has been also required to be soft, so aluminum was chosen because Young's modulus of aluminum is almost half of copper's. Therefore, the heat link is made of pure aluminum with a purity of 99.9999 % (6 N). Furthermore, it is composed of many thin wires to decrease the effective spring constant (detail can be found in section 4.2.4).

The composition of the heat link is shown in figure 4.3. The minimum unit of the heat link is a thin wire with a diameter of 0.15 mm. Seven thin wires are gathered and stranded, and a primary twist is formed. Similarly, seven primary twists are gathered and stranded, and a secondary twist is formed. The heat link is made by seven secondary twists in parallel with two terminals made by 5 N aluminum at both ends. Each terminal has a hole with a diameter of 5 mm to be fixed by an M4 screw. Fabrication was carried out by Japanese companies;

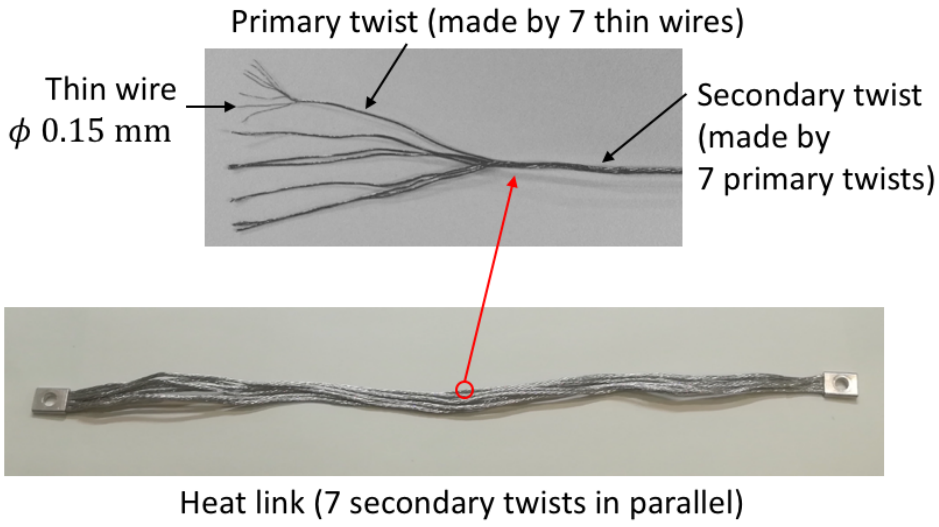

Figure 4.3: Detail of the heat link. One heat link consists of $7 \times 7 \times 7$ thin wires. End terminals are made by 5 N aluminum.

the pure aluminum was produced by Sumitomo Chemical Co., Ltd., thin wires were made by Noge Electric Industries Co., Ltd., the stranding work was done by Arai Co., Ltd., and the terminal was clamped by Furukawa Electric Power Systems Co., Ltd.

4.2.2 Thermal conductivity

The high thermal conductivity allows us to reduce the number of heat links required, that is, amount of vibration inflow to the cryopayload can be reduced. The thermal conductivity of the developed heat link has been practically measured as shown in figure 4.4 [53, 69]. The measured maximum thermal conductivity was 18500 W/m/K at 10 K.

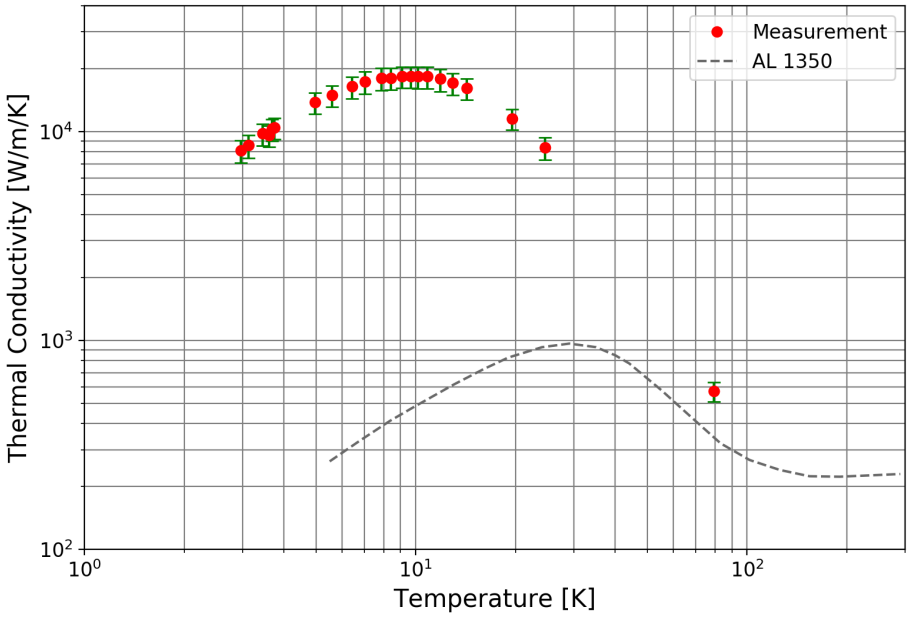

Figure 4.4: Measured thermal conductivity (red points) [53, 69]. Grey broken line is the thermal conductivity of AL 1350 for comparison [67]. The measured maximum value was 18500 W/m/K at 10 K.

4.2.3 Contact thermal resistance

Equation (4.5) defines thermal resistance, which is calculated by thermal conductivity. However, in cryogenic engineering field, it is well known that there exists thermal resistance in contacts, and it is difficult to estimate thermal resistance of these contacts theoretically. Therefore, they were measured for KAGRA's case this time.

Contact thermal resistances considered

The heat link shown in figure 4.3 is used as shown in figures 4.5 and 4.6 in KAGRA. In figure 4.5, the heat link is mounted on 6 N aluminum thin plate. In figure 4.6, terminals of two heat links are connected.

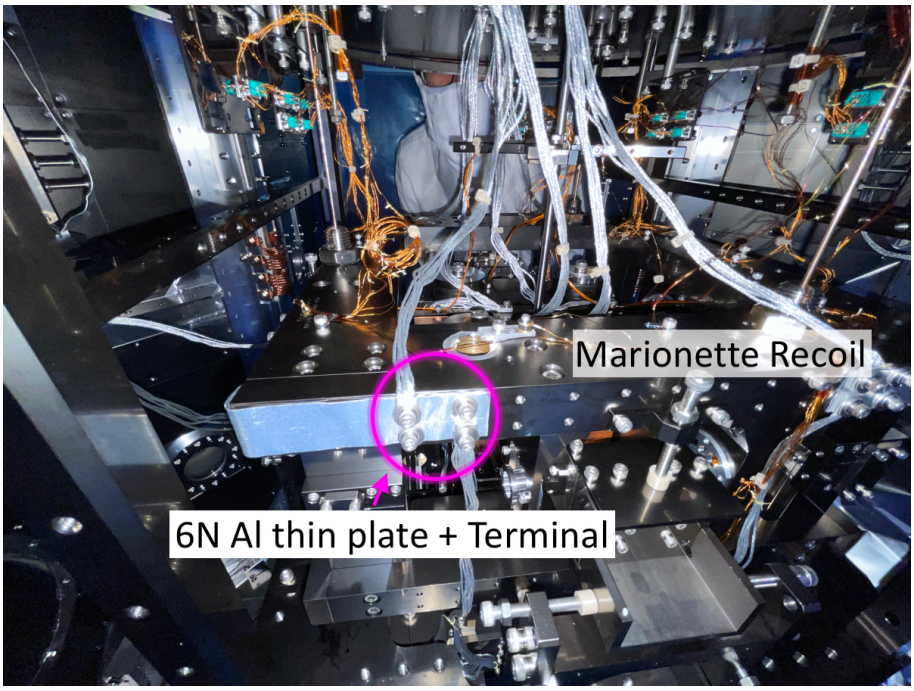

Figure 4.5: Photo of connection part of the 6 N aluminum thin plate and the heat link.

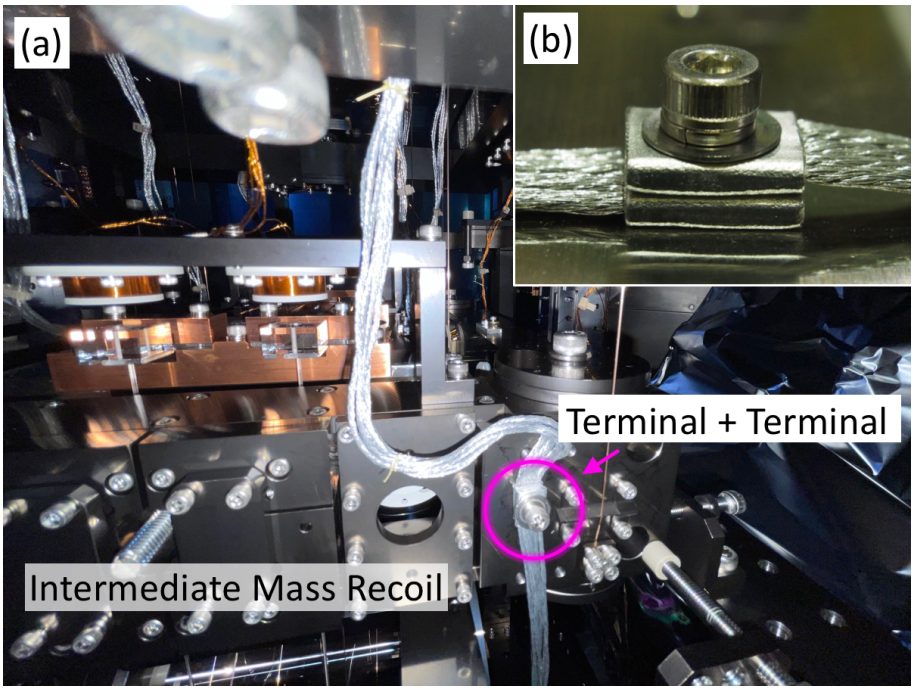

Figure 4.6: (a) Photo of terminal connection of two heat links. (b) Detail of connection of terminals. A stainless steel block with 3 mm in thickness will be inserted practically instead of a flat-washer.

Considering figures 4.5 and 4.6, considerable thermal resistances in the heat link path are schematically summarized as shown in figure 4.7. $R_{\mathrm{cond\_HL}}$ and $R_{\mathrm{cond\_PL}}$ are thermal resistances of the heat link and 6 N thin plate, respectively, which are calculated by thermal conductivities. R_{Term}, $R_{\mathrm{cont\_PLHL}}$ and $R_{\mathrm{cont\_HLHL}}$ are contact thermal resistances inside the terminal, between surfaces of the terminal and 6 N thin plate, and between surfaces of two terminals. These three contact thermal resistances have to be measured. Since the heat links are used in the case of either figures 4.5 or 4.6 in KAGRA, it is enough to measure compound thermal resistances such as $R_{\mathrm{Term}} + R_{\mathrm{cont\_PLHL}}$ in the left rectangle and $2R_{\mathrm{Term}} + R_{\mathrm{cont\_HLHL}}$ in the right rectangle in figure 4.7.

To study R_{Term} more, we observed the cross-section of the terminal as shown in figure 4.8[‡2]. It was found that there were many gaps, that is, side surfaces of many thin wires did not touch perfectly. These gaps may become sources of contact thermal resistance inside the terminal.

[‡2]Lapping process was performed by Mechanical Engineering Center in KEK.

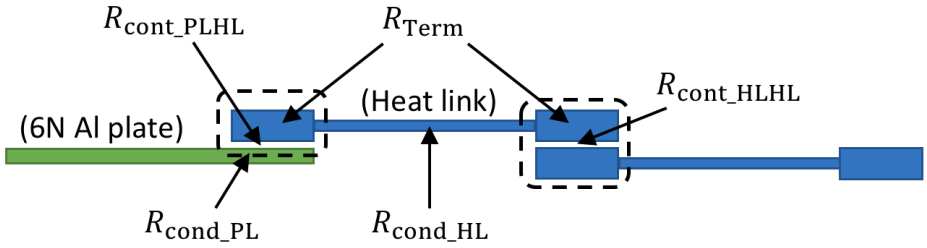

Figure 4.7: Schematic view of thermal resistances in the heat link path.

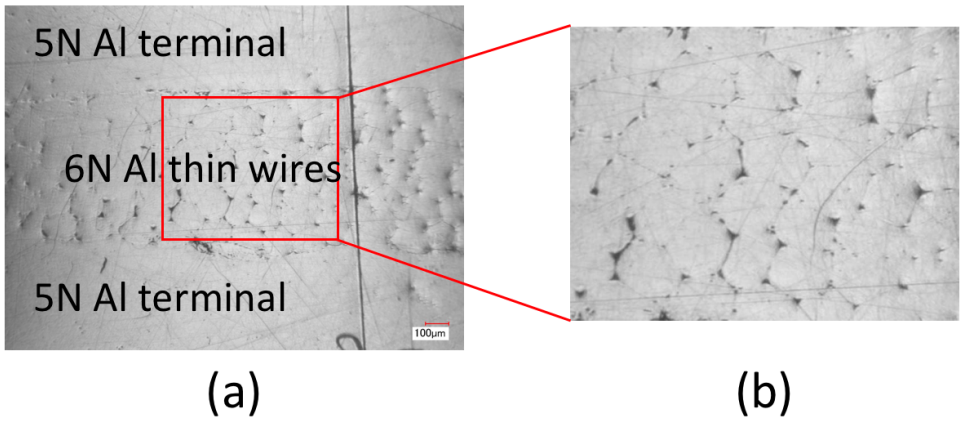

Figure 4.8: (a): Cross sectional photo of the heat link terminal. (b): Enlarged view of (a). Several gaps can be seen as black points.

Measurement method

Figure 4.9 shows schematic figures of the setup to measure the above two compound thermal resistances. Longitudinal heat flow method was adopted [67, 70]: the temperature difference was given by gradient heater at the bottom. First, overall thermal resistance was calculated by measuring the temperature difference $T_1 - T_2$ and input heat P. Then, thermal resistances of conductors, which can be calculated by thermal conductivities, were subtracted from them. The remaining value was the compound thermal resistance. To measure several points with respect to temperature, a base heater on the top copper base block

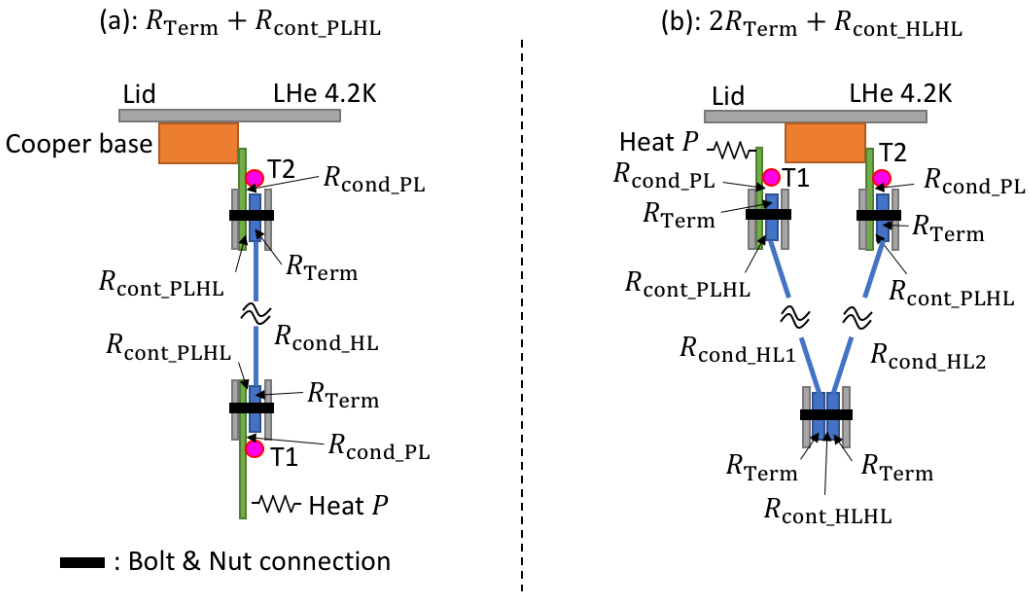

Figure 4.9: (a): Schematic view of measurement setup for $R_{\mathrm{Term}} + R_{\mathrm{cont\_PLHL}}$. (b): Schematic view of measurement setup for $2R_{\mathrm{Term}} + R_{\mathrm{cont\_HLHL}}$. The end is suspended by Kevlar wire.

was used to control the temperature of the whole setup. The setup was cooled with liquid helium as shown in figure 4.10.

For measuring $R_{\mathrm{Term}} + R_{\mathrm{cont\_PLHL}}$, the setup shown in figure 4.9 (a) was used. In this setup, the temperature gradient can be derived by

$$T_1 - T_2 = (2R_{\mathrm{cont\_PLHL}} + 2R_{\mathrm{Term}} + R_{\mathrm{cond\_HL}} + 2R_{\mathrm{cond\_PL}}) \times P. \tag{4.6}$$

Since thermal conductivities of the heat link and thin plate have already been measured, the compound thermal resistance $R_{\mathrm{Term}} + R_{\mathrm{cont\_PLHL}}$ can be obtained.

For measuring $2R_{\mathrm{Term}} + R_{\mathrm{cont\_HLHL}}$, the setup shown in figure 4.9 (b) was used. In this setup, the temperature gradient can be derived by

$$T_1 - T_2 = (2R_{\mathrm{cont\_PLHL}} + 4R_{\mathrm{Term}} + R_{\mathrm{cont\_HLHL}} + R_{\mathrm{cond\_HL1}} + R_{\mathrm{cond\_HL2}} + 2R_{\mathrm{cond\_PL}}) \times P. \tag{4.7}$$

By using the measured result of the compound thermal resistance of $R_{\mathrm{Term}} + R_{\mathrm{cont\_PLHL}}$, $2R_{\mathrm{Term}} + R_{\mathrm{cont\_HLHL}}$ value can be eventually obtained.

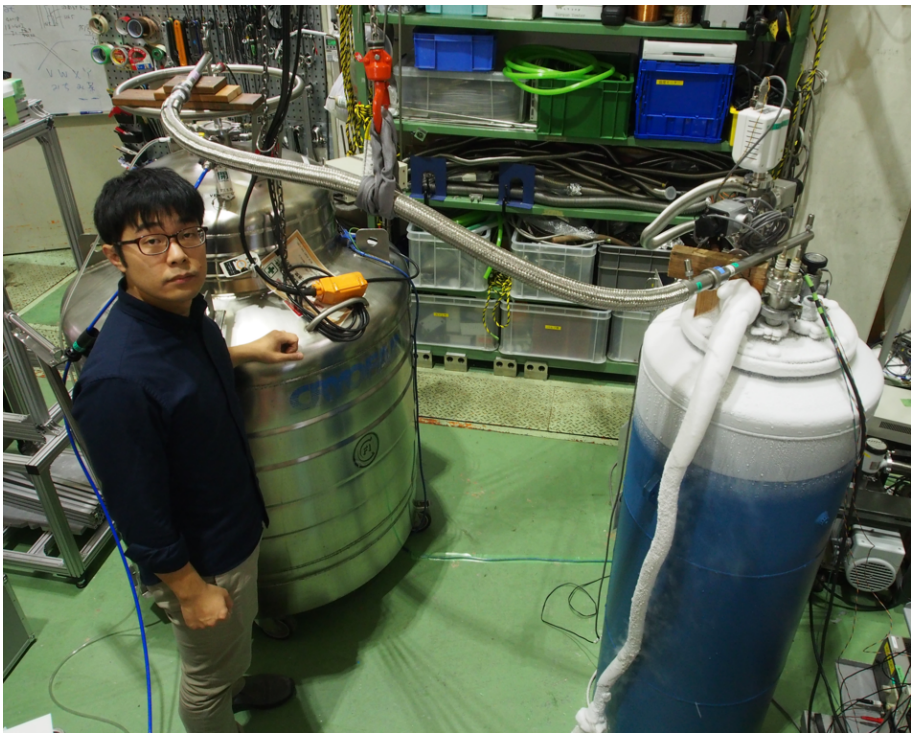

Figure 4.10: Photo of thermal resistance measurement. Left silver tank is 500 L liquid helium dewar. In the right blue cryostat, a vacuum tank with specimen is installed and cooled with transferred liquid helium. Vacuum pump unit is located back side of the blue cryostat.

All the thermometers were calibrated Cernox sensors. To reduce heat leakage through electrical wires, all wires were once anchored on the top copper base. Phosphor bronze wires were used for the thermometers. To reduce measurement error, electrical resistance of the gradient heater should be larger than electrical wires. The electrical resistivity of the manganin wire was measured as 15.6 Ω/m, 100 mm of wires were used, and the number of current lead was two, so the electrical resistance of the manganin wires is approximately 3.1 Ω. Therefore, 560 Ω of metal film resistor was chosen for the gradient heater to achieve below 1 % error. Heat extraction by thermal radiation was negligible because it was estimated to be orders of 100 μW while input heat was within several tens to hundreds mW. The samples were partially suspended by Kevlar wires so as not to give stress to the heat link. Heat extraction via Kevlar wires was negligible because they have extremely low thermal conductivity at cryogenic temperature.

250 mm long heat links were used for $R_{\mathrm{Term}} + R_{\mathrm{cont\_PLHL}}$ measurement, and 250 mm and 400 mm long heat links were used for $2R_{\mathrm{Term}} + R_{\mathrm{cont\_HLHL}}$. Length uncertainty due to terminal length became main source for error bar.

Measured result

In figures 4.11 and 4.12, colored points represent measured data while black curve shows the estimated $R_{\mathrm{cond\_HL}}$ calculated by thermal conductivity. There are large gaps between them. It indicates that these gaps obviously include the effects of contact thermal resistances.

Figure 4.13 shows values of $R_{\mathrm{Term}} + R_{\mathrm{cont\_PLHL}}$ and $2R_{\mathrm{Term}} + R_{\mathrm{cont\_HLHL}}$ calculated from measured results. Both curves have very similar shapes having minima around 18 K.

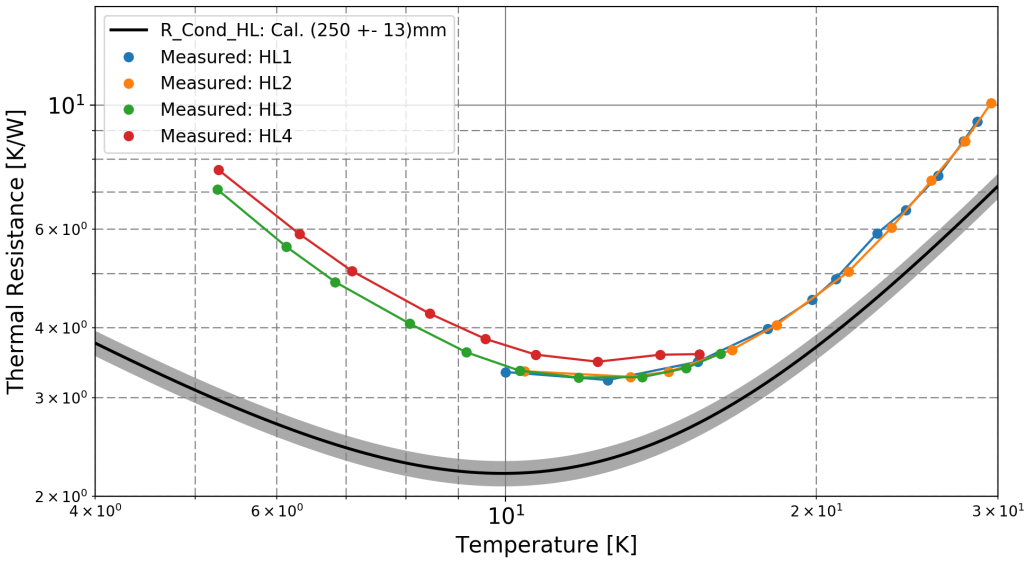

Figure 4.11: Results of $R_{\mathrm{Term}} + R_{\mathrm{cont\_PLHL}}$ measurement. High temperature region was measured in the first cooling. Then, low temperature region was measured after disassembling the whole setup once. Black curve shows calculated $R_{\mathrm{cond\_HL}}$ and grey zone represents error region due to length uncertainty.

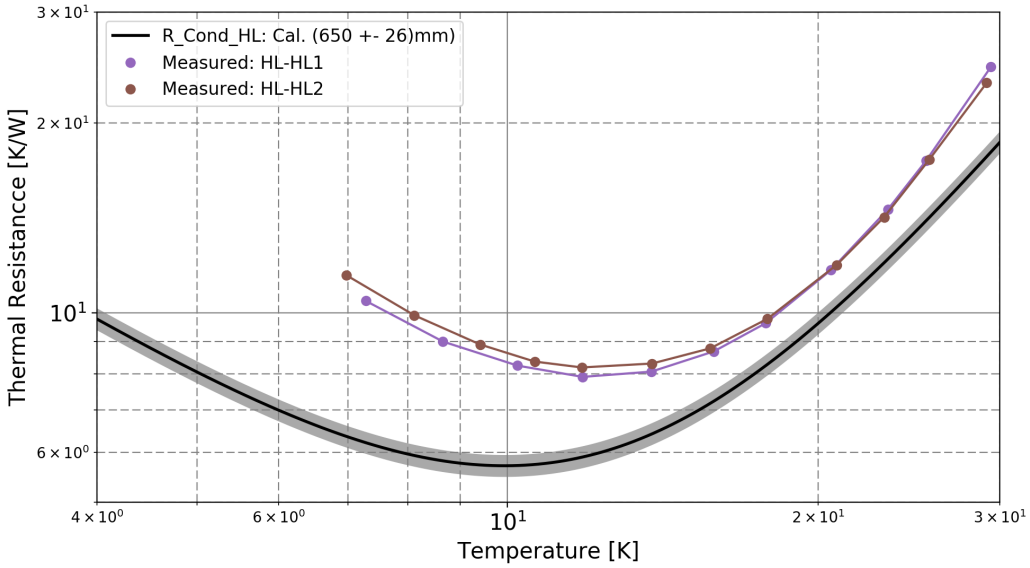

Figure 4.12: Results of $2R_{\mathrm{Term}} + R_{\mathrm{cont\_HLHL}}$ measurement. Black curve shows calculated $R_{\mathrm{cond\_HL1}} + R_{\mathrm{cond\_HL2}}$ and grey zone represents error region due to length uncertainty.

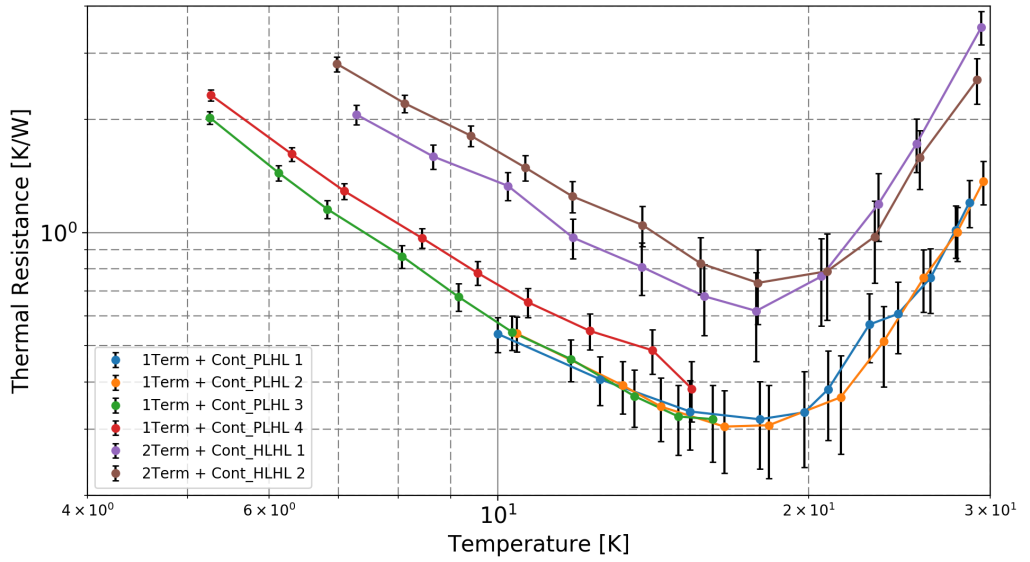

Figure 4.13: Obtained thermal resistances of $R_{\mathrm{Term}} + R_{\mathrm{cont\_PLHL}}$ and $2R_{\mathrm{Term}} + R_{\mathrm{cont\_HLHL}}$. Error bars are mainly due to length uncertainty.

4.2.4 Spring constant

The spring constant is an important factor to discuss vibration transfer. In cantilever shape, the spring constant of a cylindrical wire, k, is generally expressed as

$$k = 3\frac{EI}{L^3} = 3\frac{E}{L^3}\frac{\pi r^4}{4}, \tag{4.8}$$

where E, I, L, and r are Young's modulus, the moment of inertia of area, length, and radius of a wire.

Gathering thin wires results in reducing the spring constant. If N thin wires are lined up in parallel, the combined spring constant k_N is written as

$$k_N = N \times k_1 = N \times 3\frac{E}{L^3}\frac{\pi r_1^4}{4}, \tag{4.9}$$

where k_1 and r_1 are the spring constant and radius of a thin wire. When the total cross-sectional area of single wire and thin wires are the same, i.e. $\pi r^2 = N\pi r_1^2$, k_N has a relationship with k as

$$k_N = \frac{1}{N}k. \tag{4.10}$$

Equation (4.10) tells us that it is possible to effectively decrease the spring constant by gathering many thin wires. Therefore, this approach enables to achieve soft connection[‡3]. This is the reason why we have made the stranded cable type heat link as shown in figure 4.3. Experimentally, it was confirmed that the spring constant of our heat link was decreased to 1/43 by gathering thin wires when it is compared with single wire with same cross-sectional area [53, 69].

[‡3]Size effect also needs to be considered.

4.3 Cooling result

In this section, cooling results of the ETMY are analyzed using measured results reported in section 4.2.

4.3.1 Cooling curve

We performed the cooling test of Y-end Test Mass (ETMY) in spring of 2018. Figure 4.14 shows the cooling curve of the cryopayload for several stages. The gradients of cooling curves of cryopayload were changed around $70 - 80$ K. As discussed in section 4.1.3, it seems that thermal radiation is dominant above those switching temperatures. It is also considered that steep inclination after those temperatures occurred because of following two features: increase of thermal conductivity and decrease of specific heat.

Before reaching minimum temperatures, one cryocooler for the suspension entered a quasi-stable state and temperature of its cold head stopped at 23 K. Since two cryocoolers are connected to the cryopayload as explained in section 3.3.2, it is assumed that the temperature distribution inside the cryostat caused an inbalance of heat flow. We then once stopped those cryocoolers and restarted them again. Finally, the sapphire TM reached 17.8 K and the IM reached 14.9 K [12].

4.3.2 Heat flow estimation

Figure 4.15 shows the final temperature distribution during the cooling process. This is when the laser was not injected. The temperature difference between Cooling Bar (CB) and TM was over 10 K. Even if there is no laser absorption, thermal radiation from apertures enters TM, however, this value was reported as 50 mW in total [71]. This small value doesn't apparently explain the temperature gradient in figure 4.15. One of the easiest and the most reasonable explanation for such a large temperature gradient is unexpected heat flow.

Assuming that temperature gradient is caused by heat flow, the values are estimated for four paths shown in figure 4.15. Paths are: (1) TM to IM, (2) IM to MNR, (3) TMR to MNR, and (4) MNR to CB. In figure 4.15, $\triangle$ and $\square$ represent thermal resistances of $R_{\mathrm{Term}} + R_{\mathrm{cont\_PLHL}}$ and $2R_{\mathrm{Term}} + R_{\mathrm{cont\_HLHL}}$, respectively. Necessary information for calculation such as the number of conductors, geometry, and thermal conductivity are summarized in table 4.1.

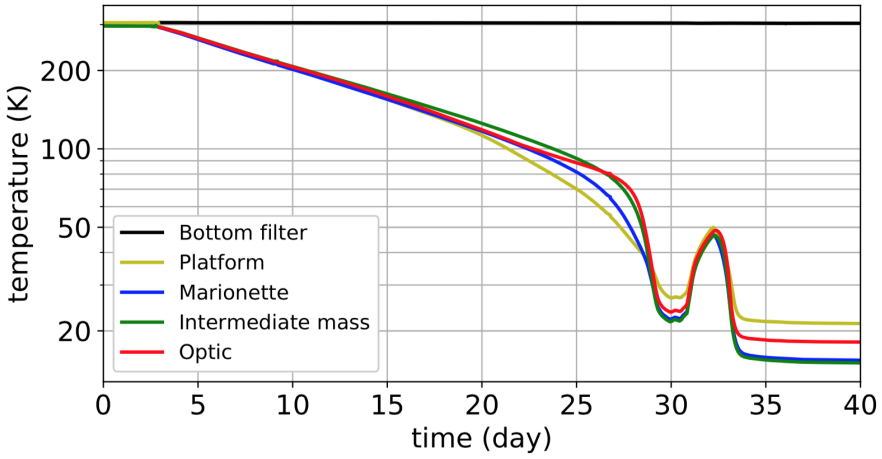

Figure 4.14: Cooling curve of the cryopayload [12]. One cryocooler for the suspension entered a quasi-stable state and temperature of its cold head stopped at 23 K. We then once stopped conductive-cooling-cryocoolers and restarted them again.

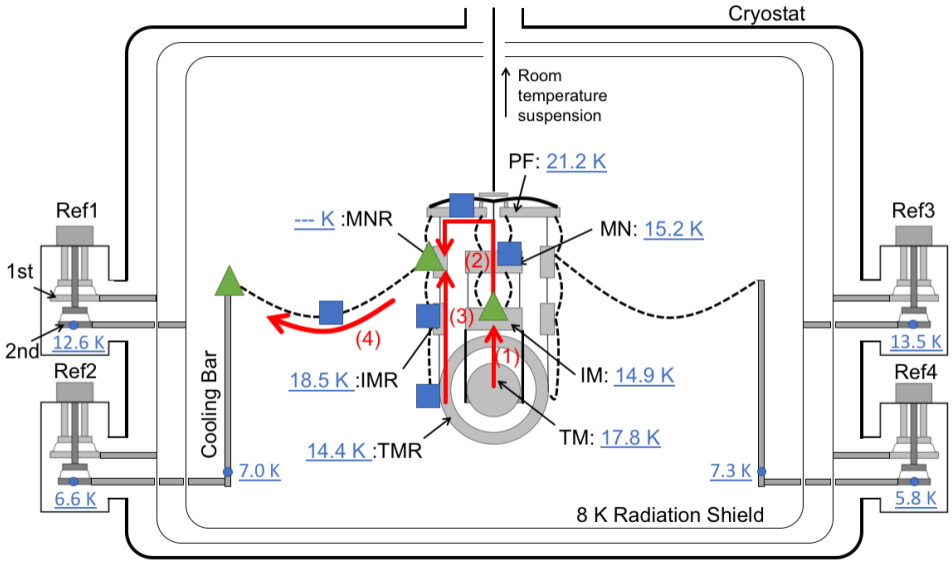

Figure 4.15: Final temperature distribution. △ and □ represent thermal resistances of $R_{\mathrm{Term}} + R_{\mathrm{cont\_PLHL}}$ and $2R_{\mathrm{Term}} + R_{\mathrm{cont\_HLHL}}$, respectively. The temperature difference between CB and TM was over 10 K.

Path (1): I first explain the story of sapphire fiber. Four sapphire fibers suspend the TM from the IM stage as explained in section 3.2.4. A sapphire fiber consists of three parts: two nail heads and a rod, and they are bonded with Sumiceram adhesive. The thermal conductivity of Sumiceram-bonded sapphire fiber is measured as shown in figure 4.16 [72]. Figure 4.16 shows two kinds of measured results: blue dots are the thermal conductivity of the sapphire rod and orange dots are the one between two nail heads including the effect of the Sumiceram bonding. In this dissertation, the latter data is used to reflect practical situation. Heat flow from the TM to IM was calculated as

$$P_{(1)} = \Delta T / R_{\mathrm{Sapphirefiber}} = (17.8 - 14.9)/16.1 = 0.18\,\mathrm{W}. \tag{4.11}$$

$R_{\mathrm{Sapphirefiber}}$ was calculated using equation (4.5) and table 4.1. The value having error bar is shown in table 4.1. The dominant factor of error bar was accuracy of thermometers which was $\pm\,0.5\,\mathrm{K}$.

Path (2)-(4): Since the temperature of the MNR stage was missing, it is not possible to calculate heat flows in the paths (2)−(4) as path (1). Therefore, assuming that the temperature of the MNR is T_{MNR}, we first build three equations as follows:

$$P_{(2)} = (14.9 - T_{\mathrm{MNR}})/R_{(2)}, \tag{4.12}$$

$$P_{(3)} = (14.4 - T_{\mathrm{MNR}})/R_{(3)}, \tag{4.13}$$

$$P_{(4)} = (T_{\mathrm{MNR}} - 7)/R_{(4)}, \tag{4.14}$$

where P_i and R_i are heat flow and thermal resistance of path (i). If we assume that $P_{(4)} = (P_{(2)} + P_{(3)})/2$ ($P_{(4)}$ is a path for one cryocooler), we can solve these simultaneous equations. Thermal resistances also need to be somehow decided. In figure 4.15, the CB and IM are at 7.0 K and 14.9 K, respectively, so temperature of the MNR is estimated within those temperatures. According to figure 4.4, the thermal conductivities of the heat link was 16900 W/m/K and 15700 W/m/K at 7.0 K and 14.9 K, respectively, and the peak was at around 10 K. Therefore, 17100 ± 1400 W/m/K was assumed for the thermal conductivity of heat links as it was an intermediate value of the maximum and minimum values within the above temperature range. Contact thermal resistances of $\triangle$ and $\square$ depending on temperature of the stages were used. For the MNR stage, 0.6 K/W and 1.7 K/W were assumed for $\triangle$ ($= R_{\mathrm{Term}} + R_{\mathrm{cont\_PLHL}}$) and $\square$ ($= 2R_{\mathrm{Term}} + R_{\mathrm{cont\_HLHL}}$), respectively.

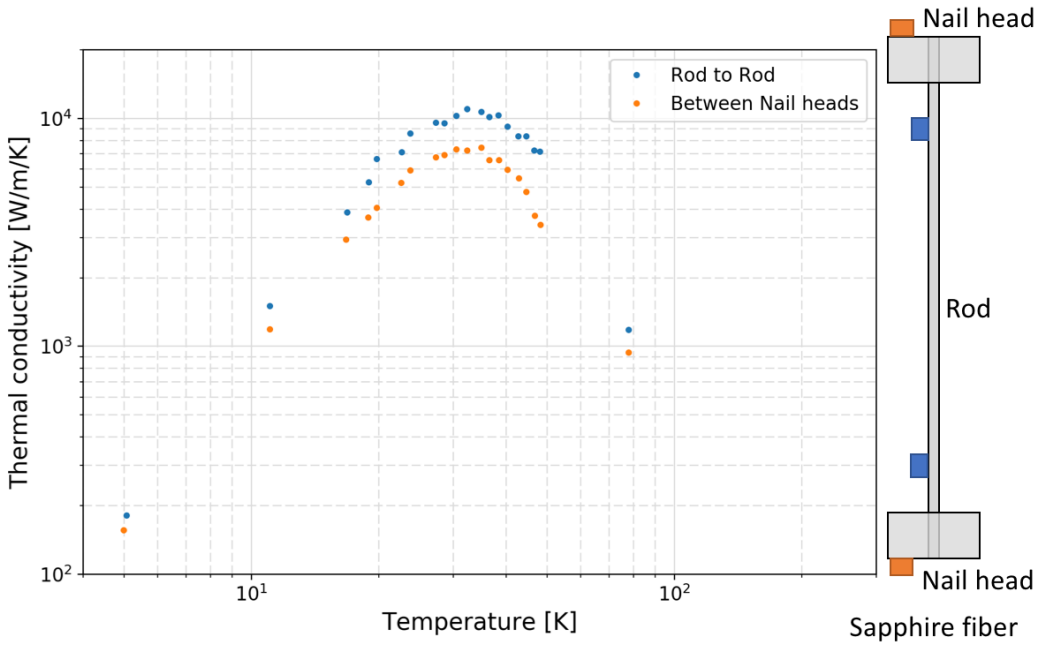

Figure 4.16: Thermal conductivity of sapphire fiber [72].

Path	Material	l [mm]	S [mm^2]	κ [W/m/K]	Heat flow [W]
(1)	Sapphire	350	8.04	2700 ± 500	0.18 ± 0.1
(2)	Al HL	1000	24.2	17100 ± 1400	0.9 ± 0.3
(3)	Al HL	700	24.2	17100 ± 1400	1.0 ± 0.5
(4)	Al HL	400+400	12.1	17100 ± 1400	0.9 ± 0.2

Table 4.1: Sumary of heat flow calculation. Path: (1) TM to IM, (2) IM to MNR, (3) TMR to MNR, and (4) MNR to CB. Note that path (4) is for one cryocooler. The dominant factor of error bar was accuracy of thermometers, which was ± 0.5 K.

Calculation results are summarized in the right column of table 4.1. Heat flows in the TM and RM chains were expected to be approximately 1 W for each. These values were unexpectedly large.

4.4 Vibration inflow via heat links

As mentioned in section 4.1.3, the heat link could introduce vibration to the cryopayload because it is connected to the vibration-isolated stage. This section first explains the calculation flow of vibration transfer, calculate the transfer function of the heat link using the Finite Element Method, and estimate displacement noise contribution due to heat link.

4.4.1 Calculation flow of vibration transfer

Schematic view of the calculation flow is shown in figure 4.17. Input vibration is vibration of the Cooling Bar (CB). Vibration of the CB is transmitted to the Marionette Recoil (MNR) via heat links. Vibration of the MNR is finally transmitted to Test Mass (TM) via Platform (PF), Marionette (MN), and Intermediate Mass (IM). A series of these flow can be expressed as:

$$\mathrm{Disp_{TM}} = \mathrm{Disp_{CB}} \times \mathrm{H_{HL}} \times \mathrm{H_{MNR \to TM}}, \tag{4.15}$$

where $\mathrm{Disp_{TM}}$, $\mathrm{Disp_{CB}}$ are vibrations of the TM and CB. $\mathrm{H_{HL}}$ and $\mathrm{H_{MNR \to TM}}$ are mechanical transfer functions (TFs) of the heat link and the payload from the MNR to TM. Horizontal and vertical degrees of freedom were considered for each parameter.

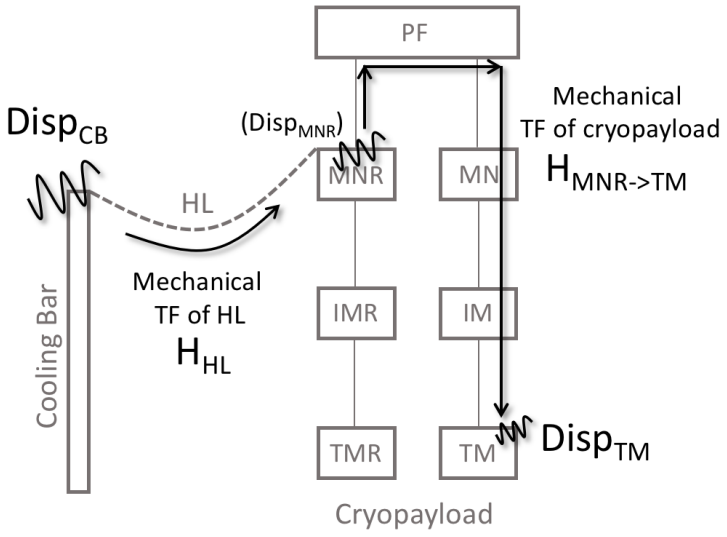

Figure 4.17: Schematic view of the calculation flow of vibration transfer.

For displacement noise estimation in this section, the measured data is used for vibration of the CB. It was measured with accelerometers[‡4] put near the top of the CB in KAGRA. The measured results are shown in figure 4.18. The mechanical transfer function of the heat links will be calculated in the following subsections. The mechanical transfer function from the MNR to TM in the cryopayload was calculated with SUMCOM[‡5] as shown in figure 4.19 [73].

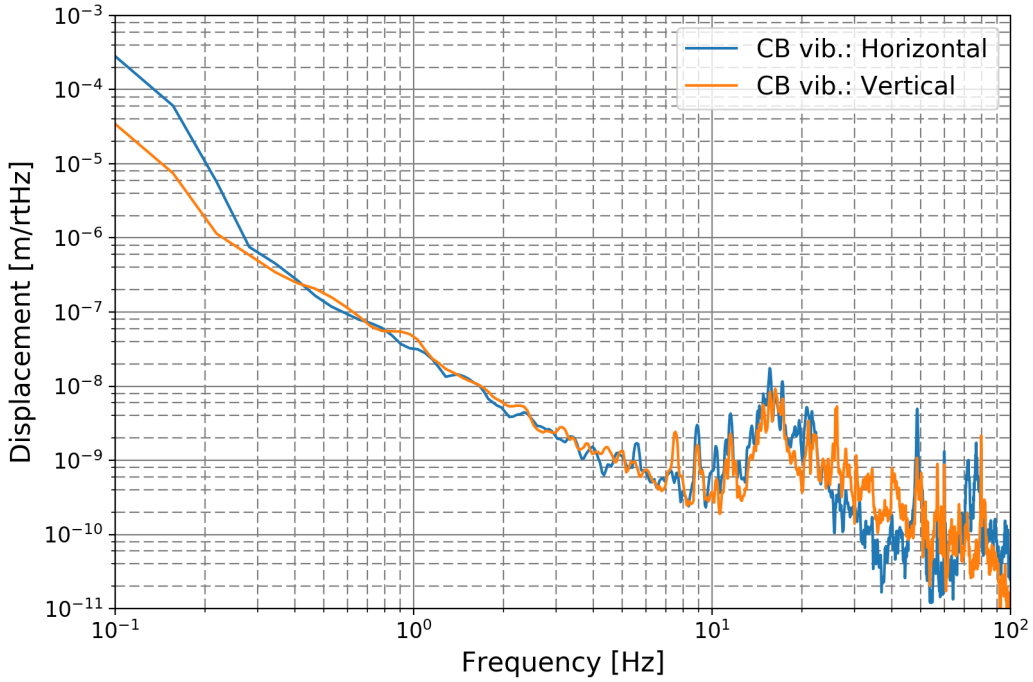

Figure 4.18: Vibration level of the CB. The broad peaks around 16 Hz are due to resonances of the radiation shield. Low-frequency regions were limited by noise level of the accelerometer.

[‡4]Accelerometer MG-102S and preamplifier OSP-06 made by Tokkyokiki Co. were used.
[‡5]Rigid body modelling tool for suspension characterization developed for KAGRA.

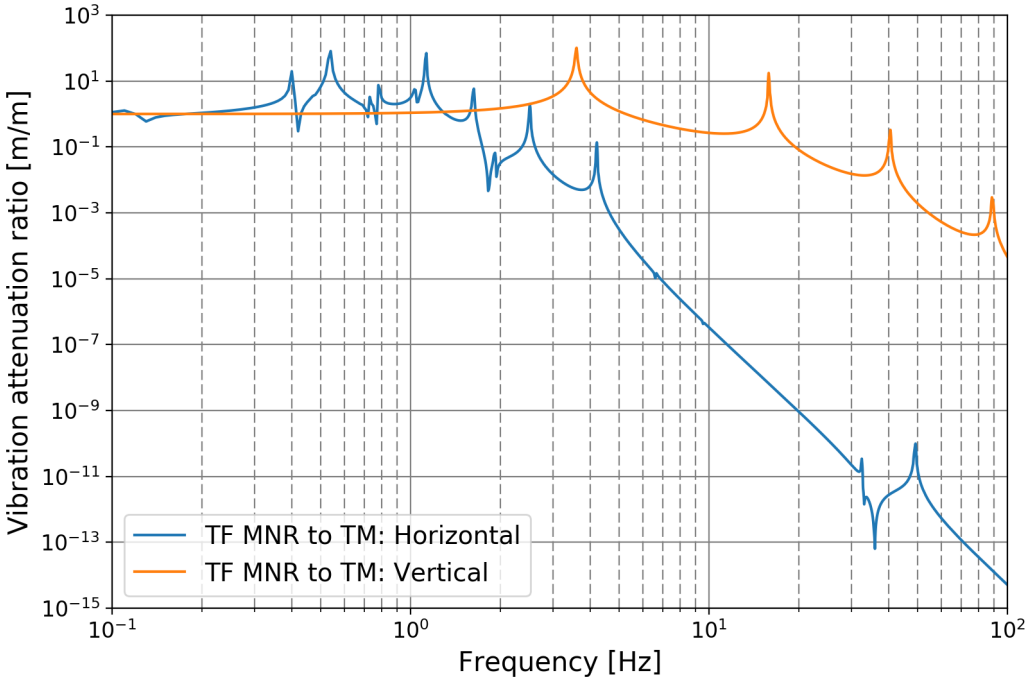

Figure 4.19: Mechanical transfer function from MNR to TM [73].

4.4.2 Calculation model of mechanical transfer function of the heat link

To estimate the vibration inflow through the heat link, the mechanical transfer function from the CB to MNR is necessary. The CB is fixed, however, the MNR is supported by the suspension and vertical spring, so these constraint conditions must be taken into account. Vibration directions to be considered are horizontal and vertical. The situations are summarized in figure 4.20 for horizontal and figure 4.21 for vertical directions. The cryopayload is assumed to be a point mass.

In figure 4.20, an equation of horizontal motion of the cryopayload is derived as

$$m\ddot{x} = -mg\frac{x}{l} - k_{\mathrm{h}}(x - X). \tag{4.16}$$

Applying Fourier transform to equation (4.16) yields

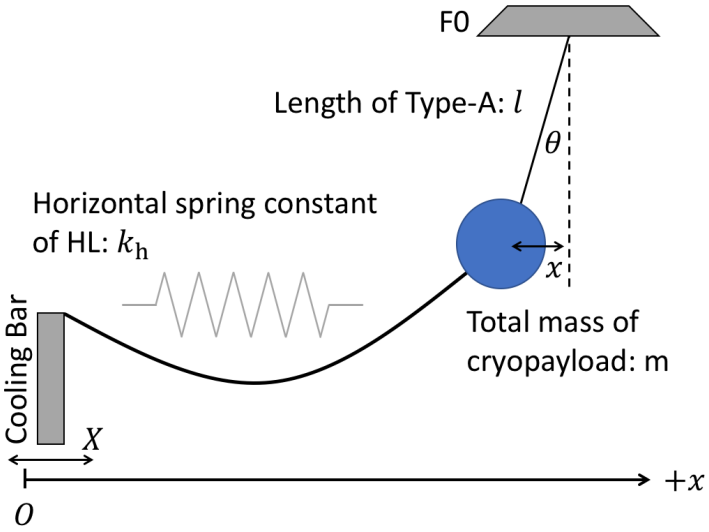

Figure 4.20: Horizontal constraint condition. It is assumed that the pendulum supports the cryopayload.

$$\frac{\tilde{x}}{\tilde{X}} = \frac{\omega_{\mathrm{h}}^2}{-\omega^2 + \omega_{\mathrm{sus}}^2 + \omega_{\mathrm{h}}^2}, \qquad \left(\omega_{\mathrm{h}}^2 = \frac{k_{\mathrm{h}}}{m},\ \omega_{\mathrm{sus}}^2 = \frac{g}{l}\right). \tag{4.17}$$

At DC region, equation (4.17) can be written as

$$\frac{\tilde{x}}{\tilde{X}} = \frac{\omega_{\mathrm{h}}^2}{\omega_{\mathrm{sus}}^2 + \omega_{\mathrm{h}}^2}. \tag{4.18}$$

In figure 4.21, an equation of vertical motion of whole system of Type-A is derived as

$$M\ddot{z} = -k_{\mathrm{F0}} z - k_{\mathrm{v}}(z - Z). \tag{4.19}$$

Applying Fourier transform to equation (4.19) yields

$$\frac{\tilde{z}}{\tilde{Z}} = \frac{\omega_{\mathrm{v}}^2}{-\omega^2 + \omega_{\mathrm{F0}}^2 + \omega_{\mathrm{v}}^2}, \qquad \left(\omega_{\mathrm{v}}^2 = \frac{k_{\mathrm{v}}}{M},\ \omega_{\mathrm{F0}}^2 = \frac{k_{\mathrm{F0}}}{M}\right). \tag{4.20}$$

At DC region, equation (4.20) can be written as

$$\frac{\tilde{z}}{\tilde{Z}} = \frac{\omega_{\mathrm{v}}^2}{\omega_{\mathrm{F0}}^2 + \omega_{\mathrm{v}}^2}. \tag{4.21}$$

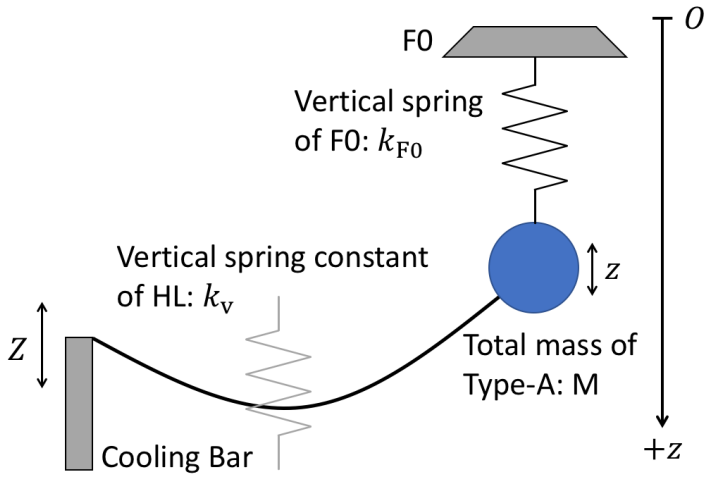

Figure 4.21: Vertical constraint condition. It is assumed that the vertical spring at the F0 stage supports whole suspension of TypeA.

In equations 4.17 and 4.20, all values except k_h and k_v are known values, they are summarized in table 4.2. Therefore, by calculating spring constants k_h and k_v, it is possible to obtain mechanical transfer functions of the heat link.

m	200 kg
M	600 kg
l	13 m
k_{F0}	2130 N/m

Table 4.2: Summary of parameters for mechanical transfer functions of the heat link.

4.4.3 Spring constant calculation by FEM modal analysis

Spring constants k_h and k_v were calculated by Finite Element Method[‡6] modal analysis. With the theory of the single harmonic oscillator, the spring constant is calculated from the resonant frequency, f, as $k = m(2\pi f)^2$. The setup shown in

[‡6]The FEM first divides an object into finite numbers of elements and then solves a series of linear equations of motions for each element. Even if the shape of the object is difficult to solve analytically, the FEM enables to reveal its behavior. This study used ANSYS Mechanical Enterprise managed by Computing Research Center in KEK.

figure 4.22 was adopted. A secondary twist was assumed instead of the heat link with seven parallel secondary twists because it was obvious that spring constant of the heat link was just seven times larger than the spring constant of the secondary twist. The geometry of the secondary twist including height difference and distance between the CB and point mass (=cryopayload) was the same as the practical relationship. A blue object was a substitute for the cryopayload, which moves only in the calculating degree of freedom. The material properties used are shown in table 4.3. According to section 4.2.4, the spring constant became 43 times smaller than a single wire with same cross-sectional area, therefore, this effect was incorporated into the analysis by reducing Young's modulus of aluminum from 68 GPa to 68/43=1.58 GPa.

Spring constants k_{h} and k_{v} were finally obtained as summarized in table 4.4. Vertical spring constant seemed to be about 20 times smaller than the horizontal.

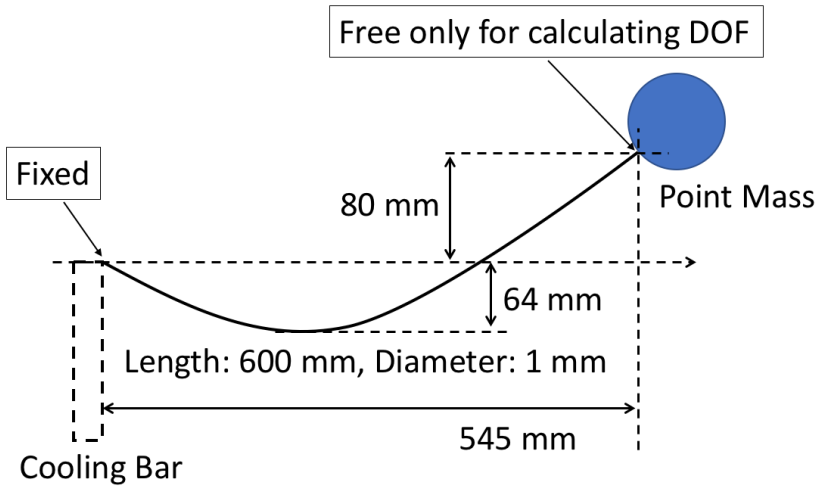

Figure 4.22: Schematic view of calculation setup. A secondary twist was used instead of the heat link. Geometry of wire was the same as the practical relationship.

Density	$2.7\,\mathrm{g/cm^3}$
Young's modulus	1.58 GPa
Poisson ratio	0.35

Table 4.3: Material properties used in the modal analysis for aluminum secondary twist. Typical Young's modulus of 68 GPa for aluminum is decreased by 43 according to section 4.2.4.

Horizontal	$1.249 \times 10^{-1}\,\mathrm{N/m}$
Vertical	$7.421 \times 10^{-3}\,\mathrm{N/m}$

Table 4.4: Obtained spring constants by modal analysis. Vertical spring constant is about 20 times softer than the horizontal.

4.4.4 Mechanical transfer function calculation by FEM frequency response analysis

The mechanical transfer function of the heat link can be easily calculated from the spring constant in the case of a simple harmonic oscillator. However, It is difficult to incorporate the effects of higher-order resonance modes analytically. Therefore the mechanical transfer function was calculated by FEM frequency response analysis.

The results of frequency response analysis are greatly affected by mechanical Q factor in general. It is known that the smaller Q factor, the greater the loss and the worse the vibration attenuation performance at high frequencies. In the following calculations, viscous damping was assumed as the type of damping and Q factor of 300 was used[‡7][‡8], which was reported in previous studies as Q factor of 5 N single wire [74].

First, mechanical transfer function in case of figure 4.22 was calculated. The input was force in frequency response analysis, so the calculation results were force to displacement transfer functions. However, since displacement to displacement transfer functions were necessary, they were normalized to be unity at DC. Normalized mechanical transfer functions are shown in figure 4.23. No

[‡7]The critical damping ratio $\xi = 1/2Q$ is usually used in ANSYS.

[‡8]Q factor of 300 might be too high because it is expected that a strand of many thin wires could have large friction loss inside strand.

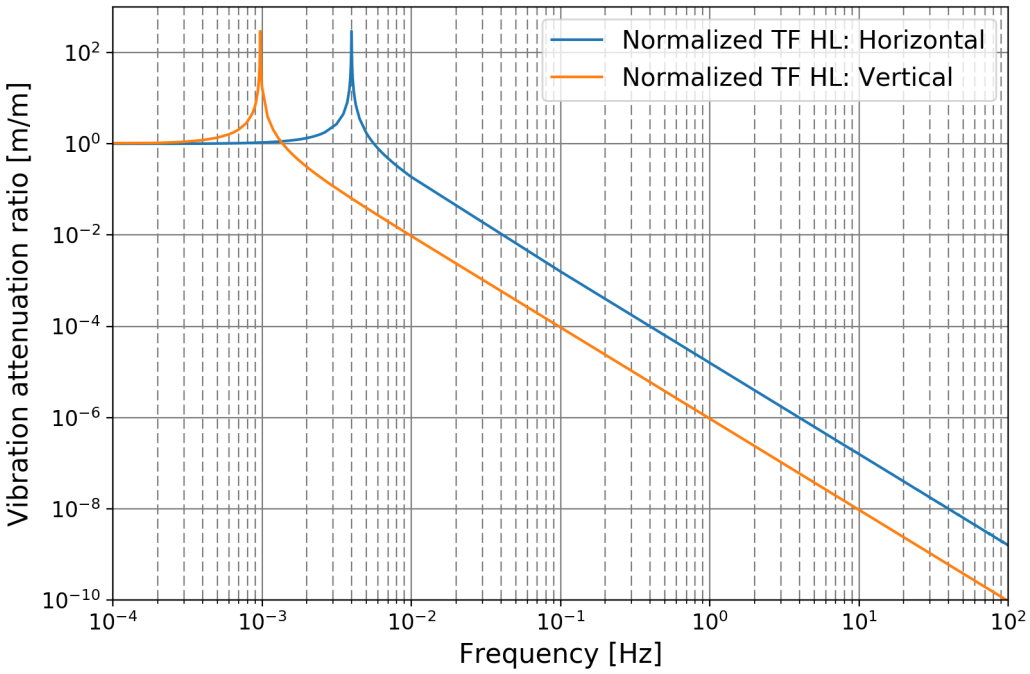

Figure 4.23: Obtained displacement to displacement transfer function. They were normalized from force to displacement transfer function.

peak of higher-order mode was observed. It was considered that the point mass was heavy enough to ignore the stiffness of the secondary twist.

In equations (4.17) and (4.20), the peak frequency ω_{res} of the transfer function is given by $\omega_{\mathrm{res}} = \sqrt{\omega_{\mathrm{sus/F0}}^2 + \omega_{\mathrm{h/v}}^2}$. These resonant frequencies are combined values of the constraint condition and aluminum heat link. ω_{sus}, ω_{F0}, ω_{h}, and ω_{v} were calculated as equation (4.22).

$$\begin{cases} \omega_{\mathrm{sus}} = 0.87, & (f_{\mathrm{sus}} = 140\,\mathrm{mHz}) \\ \omega_{\mathrm{F0}} = 1.9, & (f_{\mathrm{F0}} = 300\,\mathrm{mHz}) \\ \omega_{\mathrm{h}} = 2.5 \times 10^{-2}, & (f_{\mathrm{h}} = 4.0\,\mathrm{mHz}) \\ \omega_{\mathrm{v}} = 6.1 \times 10^{-3}, & (f_{\mathrm{v}} = 0.97\,\mathrm{mHz}) \end{cases} \tag{4.22}$$

ω_{h} and ω_{v} are the resonant frequencies of one secondary twist, however, four heat links will be connected to the cryopayload, so they need to be multiplied by $7 \times 4 = 28$. Even so they are still much smaller than ω_{sus} and ω_{F0}, therefore, peak

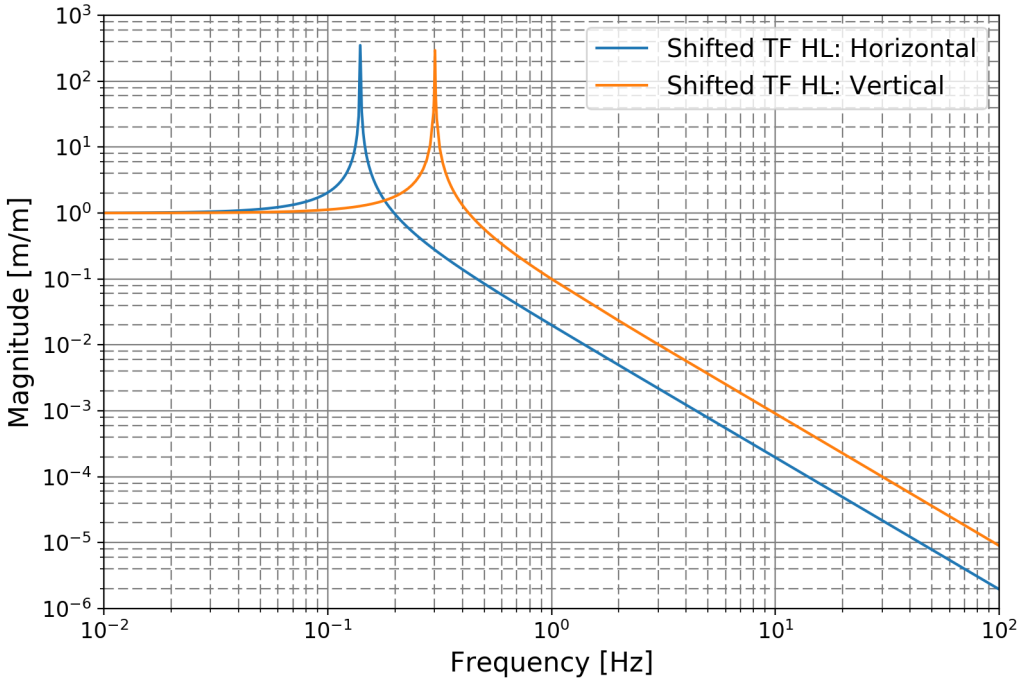

Figure 4.24: Shifted figure 4.23 to have resonances at $f = \frac{1}{2\pi}\sqrt{\omega_{\mathrm{sus/F0}}^2 + \omega_{\mathrm{h/v}}^2}$. k_{h} and k_{v} were multiplied by 28 because four heat links will be connected to the cryopayload in total.

frequencies are almost determined by the condition of constraints. In this case, the transfer functions of the heat link don't have resonances at $f = \frac{1}{2\pi}\sqrt{\omega_{\mathrm{h/v}}^2}$ as shown in figure 4.23, but have resonances at $f = \frac{1}{2\pi}\sqrt{\omega_{\mathrm{sus/F0}}^2 + \omega_{\mathrm{h/v}}^2}$. Therefore, figure 4.24 is obtained if we shift figure 4.23 to the high-frequency side so that it has resonances at these frequencies.

At last, DC gains must be adjusted. Considering equations (4.18) and (4.21) with tables 4.2 and 4.4, DC offset values were calculated. Therefore, the mechanical transfer functions of the heat links were finally calculated as figure 4.25.

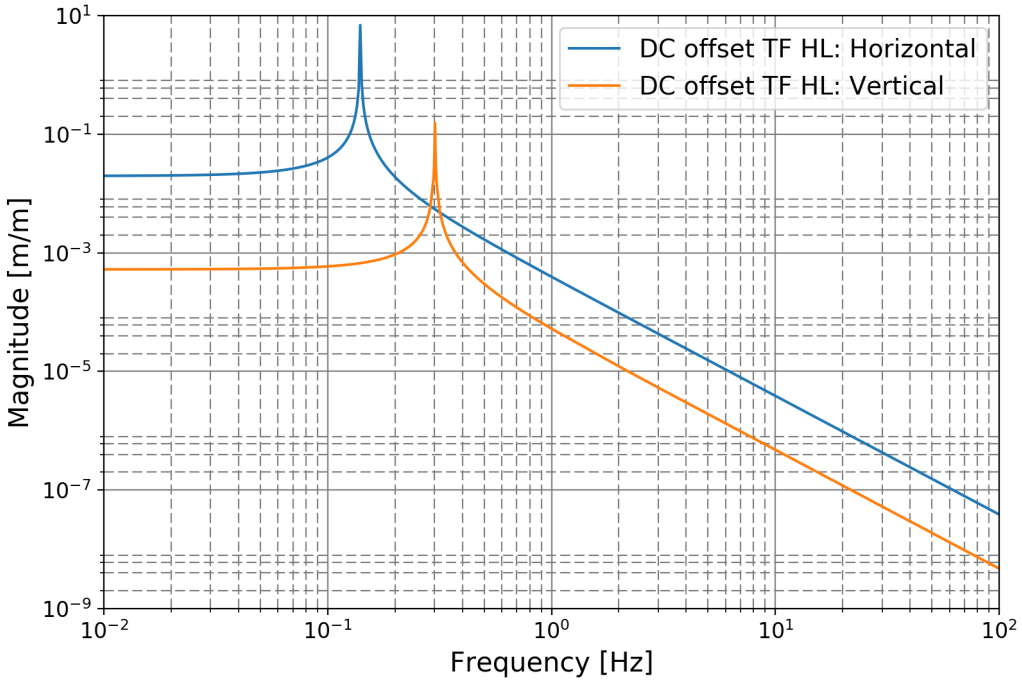

Figure 4.25: DC offset figure 4.24. Due to low spring constant of heat links in vertical, DC gain of vertical transfer function is largely reduced, however, this advantage seems to become small at high frequencies because of a relatively high resonant frequency.

4.4.5 Deterioration of sensitivity

Vibration inflow via heat links can be calculated by equation (4.15). Vibration of the CB, $\mathrm{Disp_{CB}}$, mechanical transfer function of the heat link, $\mathrm{H_{HL}}$, and mechanical transfer function from MNR to TM, $\mathrm{H_{MNR\to TM}}$, were given in figure 4.18, figure 4.25, and figure 4.19, respectively.

Since the KAGRA tunnel has an inclination of about 1/300 for water drainage, the direction of gravity is not perpendicular to the laser beam. Therefore, there is a coupling between horizontal and vertical. In this calculation, we assumed a stronger coupling ratio of 1/100, used commonly.

The results are summarized in figure 4.26. Blue and orange lines represent the displacement noise contribution caused by transmitted vibration via heat links for each degree of freedom. Red line is sum of them. As is clear from figure 4.26, it was found that vibration inflow via heat links can largely deteriorate the design sensitivity of KAGRA. As indicated by the overlap of the orange and red lines, vertical vibration inflow is problematic in the observation frequency band.

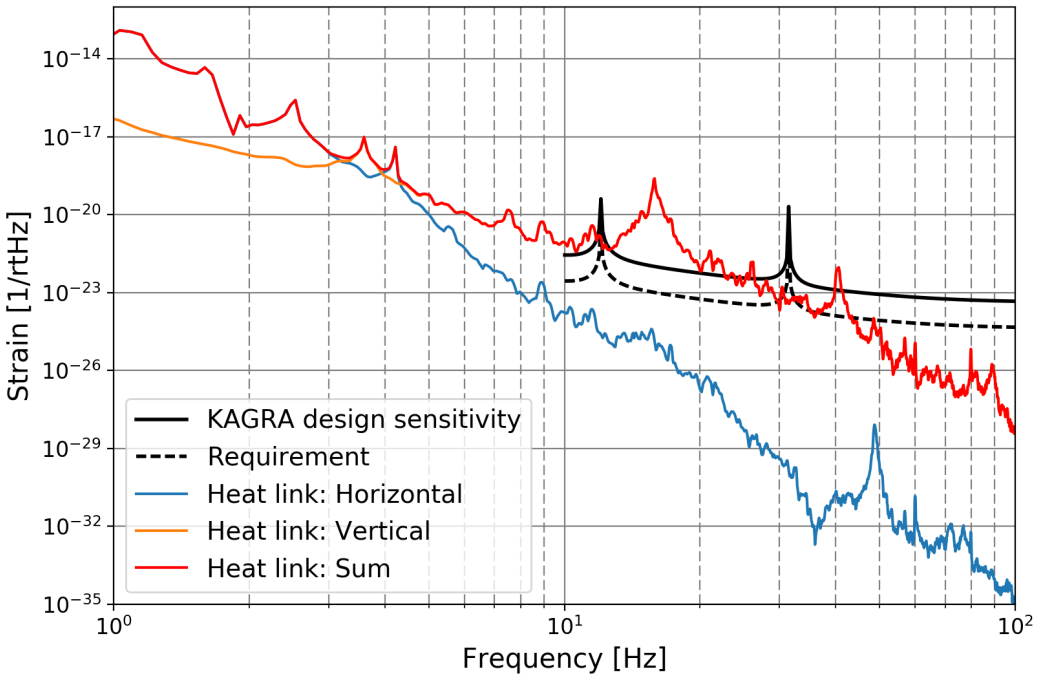

Figure 4.26: Comparison of sensitivity and vibration noise via heat links.

Figure 4.27 shows detectable volume calculated by sensitivity curve. Black and green lines were calculated by design sensitivity of KAGRA and deteriorated sensitivity due to heat link connection, respectively. Grey zone represents mass-gap region. Since the effect of the heat link was at low frequencies as shown in figure 4.26, it largely decreases the detectable volume for heavy black holes within mass-gap region. The number of detectable events is proportional to the volume, therefore, for $50 - 50\,M_\odot$ and $100 - 100\,M_\odot$ black hole mergers, it was estimated that number of detection will be decreased to aproximately half and 1/40, respectively.

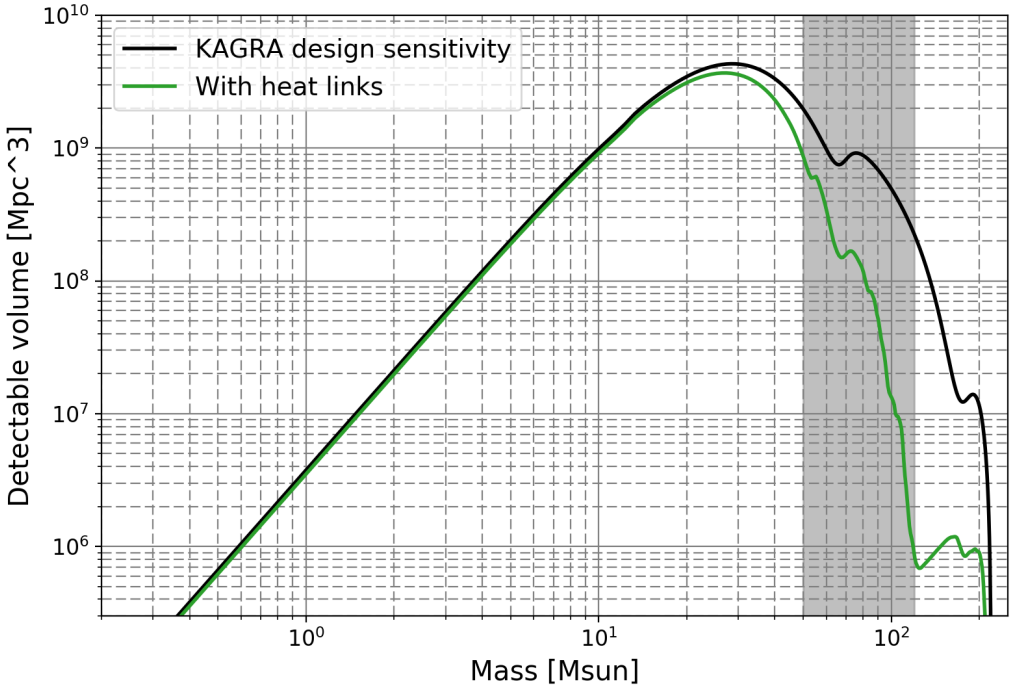

Figure 4.27: Comparison of detectable volume as a function of a component mass. Black and green lines were calculated by design sensitivity of KAGRA and deteriorated sensitivity due to heat link connection, respectively. Grey zone represents mass-gap region. Connection of heat links seems to largely decrease the detectable volume in mass-gap region.

4.5 Target of the study

As seen in figure 4.26 and 4.27, it was revealed that direct connection of the heat link makes the detector sensitivity worse and decreases the number of detectable events. On the other hand, heat links are essentially important for achieving cryogenic mirrors and reducing thermal noise. Therefore, the reduction of vibration inflow via the heat link has to be considered.

There are several ways to accomplish this purpose, but we install a new vibration isolation system called Heat Link Vibration Isolation System (HLVIS) to attenuate vibration transfer via heat links. This system should reduce vibration transfer, however, should not interfere with heat flow. Therefore, HLVIS must be considered from the viewpoints of mechanical and thermal aspects. For the mechanical aspects, the vibration attenuation performance of HLVIS needs to be evaluated at cryogenic temperature and the spring constant of the heat link, calculated by FEM, needs to be replaced with measured value for realistic estimation of vibration inflow. For the thermal aspect, heat links inside HLVIS need to be carefully arranged and the thermal design needs to be practically confirmed by the cooling test in KAGRA.

By conducting the above points one by one, I aim to reduce the vibration inflow below the noise requirement line, which is 1/10 of the sensitivity, and realize a low-vibration cryogenic mirror. This achievement will contribute to a significant improvement in the number of black hole detections, especially for the mass-gap region.

Chapter 5

Chapter 6

Chapter 7
PERFORMANCE TEST OF HLVIS IN KAGRA

Eight HLVISs in total have been installed in four cryostats of KAGRA during 2018 – 2019, and integrated cooling tests with cryopayloads were performed in the summer of 2019. Afterwards, interferometer commissioning was started towards the observing run O3. Finally, the observing run, called O3GK, was jointly performed by KAGRA and GEO600 in April 2020. This chapter first overviews assembly and installation works of the HLVIS and considers results of the integrated cooling test. Furthermore, vibration inflow via heat links is discussed with the current best sensitivity in O3GK and the sensitivity estimated for O4.

7.1 Assembly and installation of HLVIS

Assembly and installation works of the HLVIS were started in the summer of 2018 at Input-X cryostat (IXC) and completed in the spring of 2019 at End-X cryostat (EXC). All assembly works were carried out in the clean booth. Assembly procedure is briefly overviewed below.

The security frame was first assembled. The inner chain was connected from the bottom to the top. Flexible heat links and 6 N aluminum thin plates were installed on the inner chain and the security frame, respectively. Two thermometers were placed on the bottom security ring of the security frame and the 3rd stage of the inner chain.

It took about three days to complete assembly for one HLVIS. After assembling two HLVISs, they were installed into the cryostat. In order not to damage HLVISs and cryostat, installation frame, which has been used for cryopayload

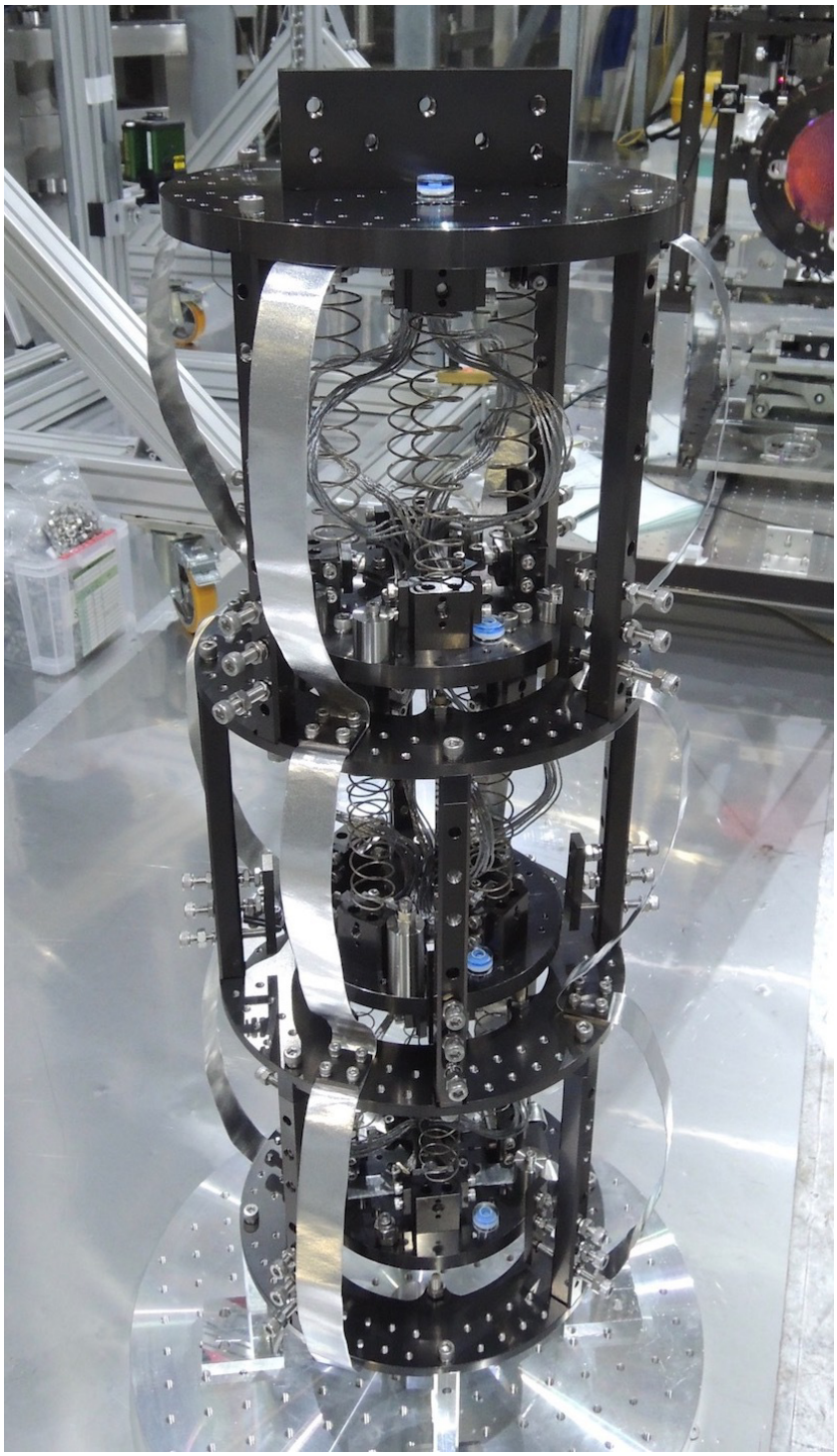

Figure 7.1: Assembled HLVIS. Low-magnetism Solblack has been coated. Flexible heat links and 6 N aluminum thin plates were mounted on the inner chain and security frame, respectively. Blue small cylinders are babble levels.

installation, was used to install HLVISs. The inner chain was fixed with screws to the security frame before the installation work. It was mounted on a cart on the installation frame and carried into the cryostat (figure 7.2). Then, the HLVIS was lifted up by two people and the third person fixes it to the beam of the ceiling of radiation shield with three M10 screws. The same procedure was repeated for the second HLVIS. Finally, thermometer wires were connected to the Burndy port, if Cryocon showed the correct value, the installation process was complete (figure 7.3).

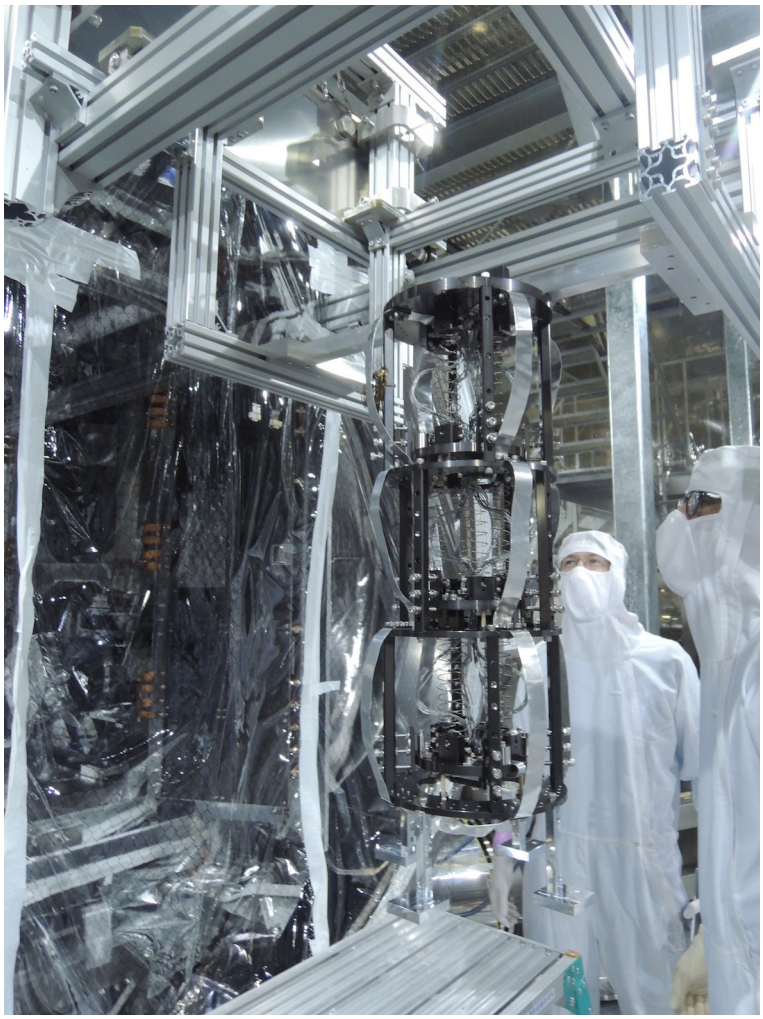

Figure 7.2: HLVIS was mounted on a cart on the installation frame for movement into the cryostat at IXC.

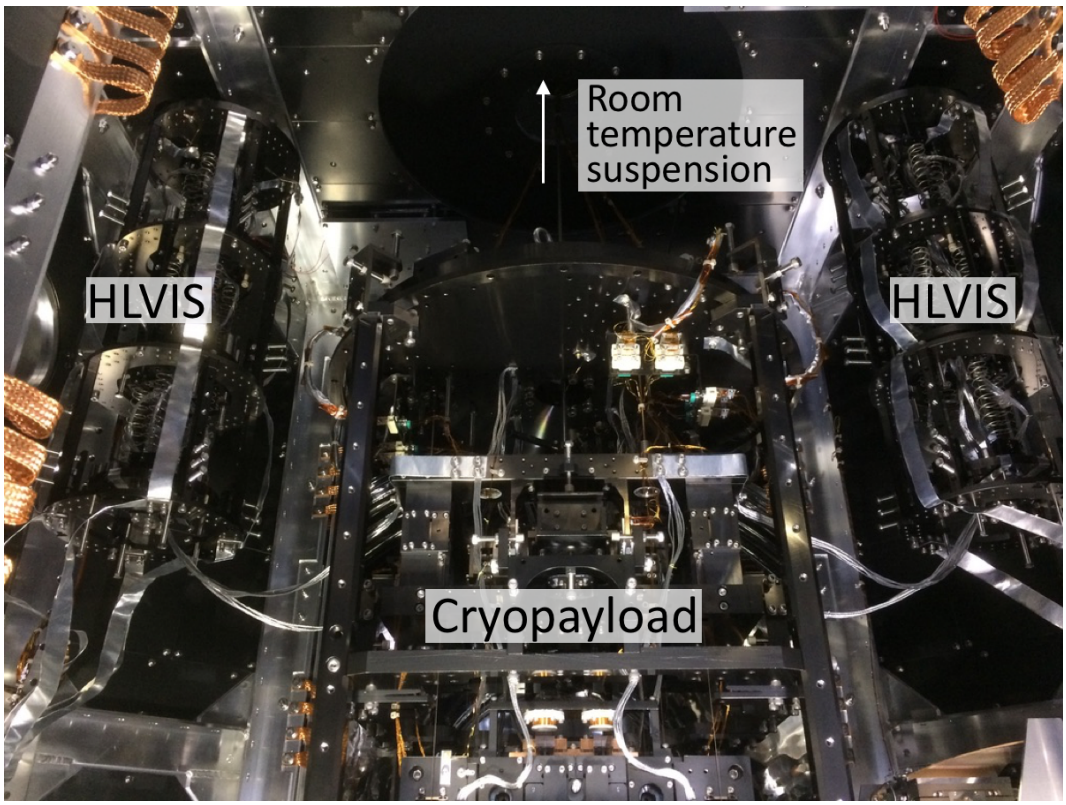

Figure 7.3: Final layout inside cryostat. Cryopayload were installed after HLVIS installation. Heat links between HLVISs and cryopaylaod were connected just before closing the cryostat.

7.2 Cooling Test with HLVIS

After installing HLVISs, integrated cooling tests were performed in all cryostats. Here, focusing on the End-Y cryostat (EYC), thermal design of the HLVIS was practically evaluated.

7.2.1 Heat flow estimation

Cooling curves were obtained as shown in figure 7.4. It took about 27 days to reach the minimum stable temperature. The final temperature distribution was as shown in figure 7.5. These temperatures were measured when the interferometer was not operating, therefore, the condition is the same as in the case of figure 4.15. As done in section 4.3.2, assuming that the temperature distribution was generated by heat flow, heat flow was calculated as summarized in table 7.1. Estimated heat flow in table 7.1 was consistent with previous results in table 4.1 within error bar.

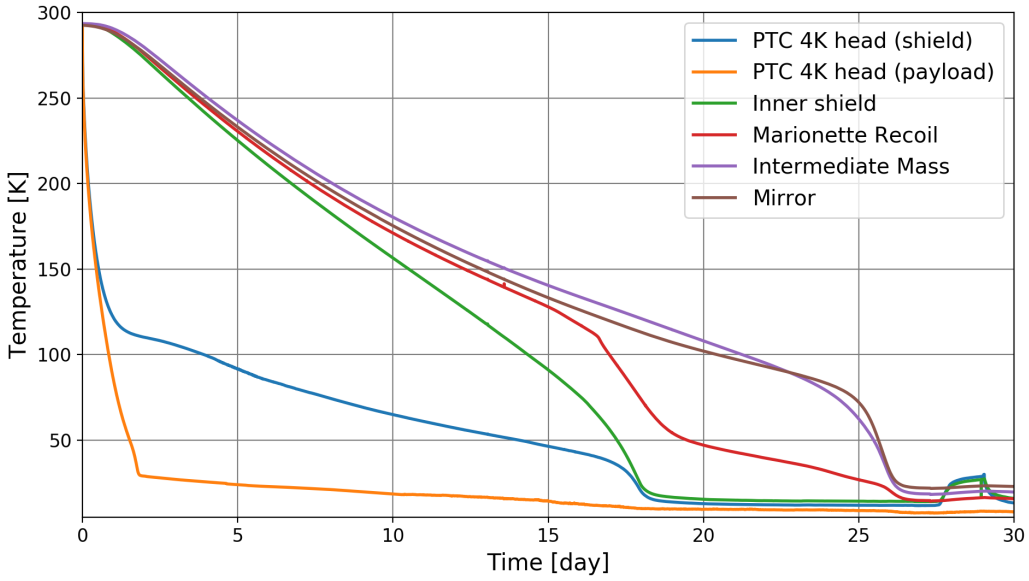

Figure 7.4: Cooling curve obtained during the EYC integrated cooling test. Cool down time was 27 days to reach a stable temperature.

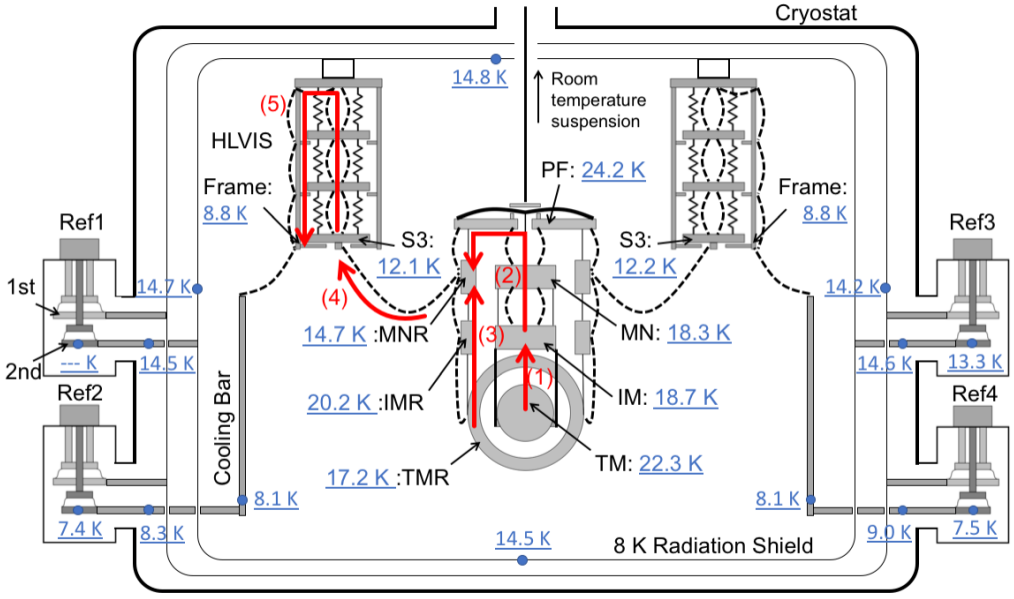

Figure 7.5: Final temperature distribution inside EYC after the integrated cooling test. Red arrows represent heat flow for five paths. Note that path (4) and (5) are for one cryocooler.

Path	Material	l [mm]	S [mm^2]	κ [W/m/K]	Heat flow [W]
(1)	Sapphire	350	8.04	4400 ± 700	0.36 ± 0.2
(2)	Al HL	1000	24.2	14000 ± 2300	1.1 ± 0.5
(3)	Al HL	700	24.2	14500 ± 1000	1.1 ± 0.5
(4)	Al HL	450	12.1	17000 ± 1000	0.99 ± 0.44
(5)	Al HL	750	24.2	18300 ± 200	1.1 ± 0.3
	Al plate	750	60	34800 ± 200	

Table 7.1: Results of heat flow calculation. Thermal conductivity of sapphire is the one including the effect of Sumiceram bonding (see figure 4.16). Note that path (4) and (5) are for one cryocooler. Main contribution of error bar is temperature accuracy of thermometer.

7.2.2 Discussion

While the IM temperature before installing HLVISs reached at 14.9 K, it stopped at 18.7 K after the installation. Temperature of the IM stage increased by +3.8 K. Here, we consider whether this temperature increase can be explained by existence of HLVIS.

The designed thermal resistance value was 3.0 K/W as explained in section **??**. The heat flow inside one HLVIS was estimated as 1.1 ± 0.3 W in table 7.1. Since temperature increase was calculated by product of thermal resistance and heat flow, an increase of the IM temperature, ΔT_{IM}, can be estimated as

$$\Delta T_{\mathrm{IM}} = R_{\mathrm{HLVIS}} \times P = 3.0 \times (1.1 \pm 0.3) = 3.3 \pm 0.9\,\mathrm{K}. \tag{7.1}$$

It seems that equation (7.1) explains the observed result within error bar. Therefore, we can conclude that thermal design of the HLVIS was as designed.

However, due to unexpected heat flow of about 1 W, TM may heat up which can be a serious problem. In this situation, IM cannot keep 16 K, which is required value to cool TM at 22 K when TM absorb heat input of 0.724 W. Reflecting these facts, we consider the realistic sensitivity for near future observing run O4 in section 7.3.2.

On the other hand, in order to achieve 16 K at the IM stage when full power laser is injected, it is indicated that improvements of the heat link such as length, number, and layout are strongly required. Details of these future tasks are presented in section 8.1.3.

7.3 Contribution of HLVIS in the past and future observation

The impact of HLVIS has been discussed based on design sensitivity so far. In this chapter, it is compared with O3GK sensitivity first and then O4 feasible sensitivity, which is calculated reflecting current issues.

7.3.1 O3GK

On February 25th, 2020, prior to O3GK observation, KAGRA started its first official observing run with a maximum binary neutron star (BNS) range of approximately 600 kpc [28]. The interferometer configuration was PRFPMI at this time. On March 10th, the observing run was temporarily stopped to adjust the alignment of the interferometer and proceed the noise investigation. After this commissioning break of about one month, KAGRA achieved about 1 Mpc in BNS range and resumed the observation on April 7th. This latter observation lasted until April 21st with GEO600 in Germany. This is called O3GK observing run.

In figure 7.6, green line shows O3GK sensitivity. Comparing it with the design sensitivity (black line), it is obvious that a large improvement is still necessary. Blue line shows vibration inflow via heat links estimated when HLVIS is not installed. Although the detector sensitivity was not seemingly limited by vibration inflow via heat links in O3GK, the vibration inflow will be large problem in O4 because KAGRA is aiming to achieve further better sensitivity shown by red line in figure 7.6. However, blue line is already suppressed to orange line by HLVIS installation, therefore, it can be concluded that the O4 sensitivity will not be limited by vibration inflow via heat links.

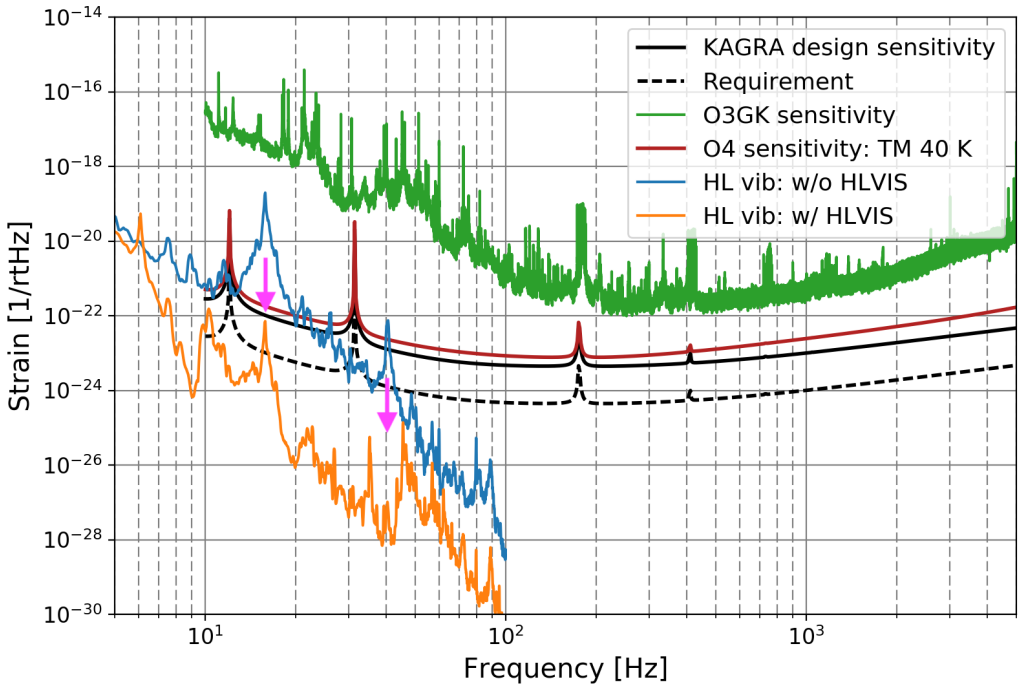

Figure 7.6: Comparison of several sensitivity curves and vibration inflow. Black solid and broken lines are KAGRA design sensitivity and noise requirement curve, green and red lines shows O3GK and estimated O4 sensitivities. Blue and orange lines are vibration inflow via heat links with and without HLVIS. Pink arrows represent reduction in vibration inflow by HLVIS.

7.3.2 O4

At the time of writing this dissertation, detector configuration of KAGRA in O4 is still under discussion. However, as already mentioned in section 7.2, temperature was increased by 3.8 K at IM stage by installing HLVISs and about 1 W of unknown heat was also found. Furthermore, although it is not mentioned so far, a frosting issue has been observed in KAGRA. This issue is that thick molecular layers are accumulated on Test Mass surface, and it reduces the finesse of the KAGRA arm cavity and finally makes the detector sensitivity worse. Since arm finesse drops around $30 - 40$ K [80], it seems the cause is residual nitrogen according to reference [81, 82].

Considering both issues, TM should not be cooled below 40 K in the current situation. Therefore, O4 sensitivity was estimated in the case of TM at 40 K. Moreover, the following improvements in O4 were considered for sensitivity calculation [83].

- **Detector configuration:** DRFPMI
- **Input power:** 300 W at BS[‡1]
- **Laser frequency and intensity noise:** 1/10 of O3GK
- **Uknown excess noise:** 1/40 of O3GK

Here, TM temperature is calculated when input power is 300 W at BS. Heat input into TM can be calculated by equation (**??**).

$$P_{\mathrm{abs}} = 2\beta_{\mathrm{sub}} t_{\mathrm{TM}} P_{\mathrm{mich}} + \gamma_{\mathrm{coa}} P_{\mathrm{circ}} + P_{\mathrm{rad}} \tag{5.17}'$$

Since $P_{\mathrm{rad}} = 50$ mW is thermal radiation from apertures, it always exist whether laser is injected or not. So, remaining two terms in the right-hand side of equation (**??**) should be considered. P_{mich} is half of $P_{\mathrm{BS}} = 300$ W; $P_{\mathrm{mich}} = 150$ W in O4. Therefore, increase of P_{abs} from when laser is injected, ΔP_{abs}, is calculated as

$$\Delta P_{\mathrm{abs}} = 0.3\,\mathrm{W}. \tag{7.2}$$

Repeating same calculation with table 7.1, we have estimated TM temperature when input power is 300 W at BS as

[‡1]Preparation status of high power laser and optical loss were considered. Moreover, input power is not so critical for O4 sensitivity.

$$T_{300\,\mathrm{W\ at\ BS}} = 28\,\mathrm{K}. \tag{7.3}$$

This temperature is obviously lower than frosting temperature, so frosting might happen if the setup is kept as it is. However, there is a $100\,\Omega$ heater made by nichrome wire on the IM stage, and it can be used to keep TM temperature high at 40 K. Therefore, it can be concluded that 40 K Test Mass is feasible in O4. Sensitivity curve estimated based on these discussion was shown with red curve in figure 7.6.

Figure 7.7 shows comparison of detectable volume using estimated O4 sensitivity curve. Red solid and broken lines are detectable volume with and without HLVIS. It is expected that HLVIS improves detectable volume, namely number of detections, by a factor of 1.5 and 11 for $50-50\,M_\odot$ and $100-100\,M_\odot$ objects, respectively, in O4.

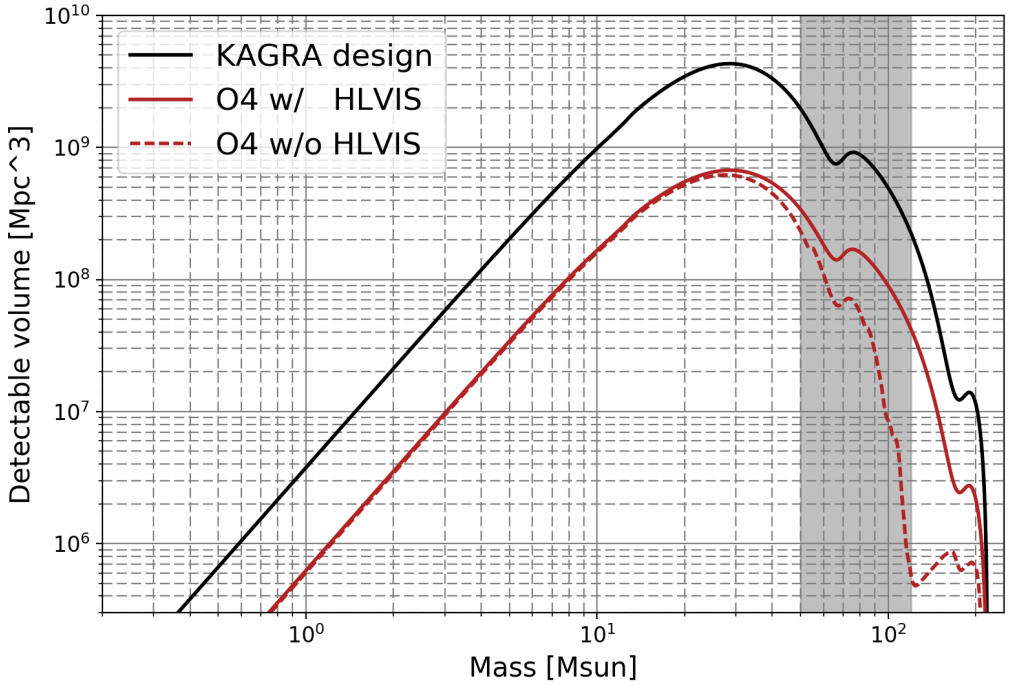

Figure 7.7: Comparison of detectable volume with and without HLVIS in O4. Black solid line is detectable volume calculated by design sensitivity. Red solid and broken lines are detectable volume in O4 with and without HLVIS, respectively.

Chapter 8
CONCLUSION

8.1 Future Prospects

8.1.1 Further reduction of vibration inflow

Although HLVIS greatly reduced vibration inflow via heat links, several peaks at around 10 Hz and 16 Hz were still over the noise requirement curve. One way to reduce these vibrations can be to make the HLVIS four stages. If new springs are designed to achieve $2\,\mathrm{Hz} - 4$ stages suspension in the vertical direction, the slope will be much steeper and the vibration can be reduced below the requirement.

8.1.2 Towards surging-free system

As seen in figure **??**, the surging phenomena of the spring makes the vibration isolation performance of the HLVIS worse above 20 Hz. These surging are not problematic at this moment, but may become a problem in future when KAGRA will be upgraded and aim to improve the sensitivity at low frequency.

In order to prevent surging, a non-linear spring is effective. This is because the resonant frequency of the non-linear spring changes while shock wave propagates along the spring wire [84]. A spring with a non-uniform pitch is considered as a non-linear spring, and it can be manufactured industrially.

8.1.3 Reduction of thermal resistance

In section 7.2, it was revealed that there was unexpected heat flow. In parallel with the identification of the origin, it is also important to consider how to extract heat flow effectively. For that, the thermal resistance of the heat link

should be smaller. Since total thermal resistance is decided by conductor and contact, both reduction should be considered.

As measured in section 4.2.3 and calculated in section **??**, contribution of contact thermal resistance are not negligible. Therefore, longer heat links should contribute to reduce thermal resistance since the number of connection can be reduced. The number of heat links in parallel also should be reconsidered, however, vibration attenuation performance should also be taken into account for that.

8.2 Conclusion

In this study, I have studied the impact of the heat links to KAGRA. The heat links are indispensable for KAGRA to achieve cryogenic sapphire Test Mass while there was a problem that they introduce vibration from the cryostat to the vibration isolated part, i.e. cryopayload. Although this problem has been actually pointed out in the previous researches, I showed a substantial solution to overcome this problem by developing the vibration isolation system for the heat link (HLVIS) for first time in the world in this dissertation. The design of the HLVIS is considered from mechanical and thermal aspects.

The requirement of the mechanical performance was to reduce vibration inflow via heat links below 1/10 of the design sensitivity. The mechanical transfer functions were measured for the horizontal and vertical directions at 16 K to verify practical mechanical performance in cryogenic environment. In the horizontal direction, although vibration attenuation performance above 10 Hz was slightly deteriorated by coupling with other degrees of freedom between $3 - 8$ Hz, its slope was as expected. In the vertical direction, the surging phenomena in the tension springs deteriorated the performance above 20 Hz, however, the slope was as expected between $10 - 20$ Hz, that is the most crucial frequency band for vibration inflow via heat links. The spring constants of the heat link were also practically measured as 1.0 N/m for horizontal and 0.22 N/m for vertical directions. Reflecting the above results, we estimated vibration inflow via HLVIS and confirmed that all peaks were suppressed under the design sensitivity in the observation frequency band. The suppressed vibration is still close to the design sensitivity so it is also indicated that further modification will be necessary in future. Thermal performance was evaluated by the integrated cooling test after the installation of the HLVIS in KAGRA. Although temperature of the cryopayload was slightly increased, it was considered that the thermal resistance of the

HLVIS was as designed. On the other hand, unexpected heat flow was found but the cause is still under investigation.

The impact of HLVIS was discussed not only with design sensitivity but also using O3GK and O4 sensitivities. Reliable sensitivity in O4 was estimated by considering issues of the unexpected heat flow and a frosting. As a result, vibration inflow via heat links was not seemingly problematic in O3GK, however, O4 sensitivity would be greatly deteriorated if HLVISs were not installed. All HLVISs were installed into the KAGRA cryostat already, therefore, it is estimated that vibration inflow via heat links will not be problem in O4.

Installation of the HLVIS allows us to improve the detector sensitivity. The number of detectable events, which is proportional to volume, is expected to be improved by a factor of approximately 2 and 40 for $50 - 50\,M_\odot$ and $100 - 100\,M_\odot$ binary black holes, respectively, in the design sensitivity. In O4 observation, about 1.5 and 11 times improvements are expected for $50 - 50\,M_\odot$ and $100 - 100\,M_\odot$ binary black holes, respectively. These achievements by developing HLVIS is essentially important for observing mass-gap objects. This work is essentially important not only for KAGRA but also for the next-generation gravitational wave detectors such as Einstein Telescope. Besides, we are sure that a part of this study will give new knowledge for low-vibration conductive cooling to the artificial satellite [85] and particle accelerator fields [86].

BIBLIOGRAPHY

[1] B.P. Abbott *et al.*, "Observation of Gravitational Waves from a Binary Black Hole Merger", Physical Review Letters, **116** 061102 (2016)

[2] B.P. Abbott *et al.*, "GW170817: Observation of Gravitational Waves from a Binary Neutron Star Inspiral", Physical Review Letters, **119** 161101 (2017)

[3] B.P. Abbott *et al.*, "Gravitational Waves and Gamma-Rays from a Binary Neutron Star Merger: GW170817 and GRB 170817A", The Astrophysical Journal Letters, **848** L13 (2017)

[4] B.P. Abbott *et al.*, "GW190521: A Binary Black Hole Merger with a Total Mass of 150 $M_{\odot}$", Physical Review Letters, **125** 101102 (2020)

[5] B.P. Abbott *et al.*, "Properties and Astrophysical Implications of the 150 $M_{\odot}$ Binary Black Hole Merger GW190521", The Astrophysical Journal Letters, **900** L13 (2020)

[6] J. Aasi *et al.*, "Advanced LIGO", Classical and Quantum Gravity, **32** 074001 (2015)

[7] F Acernese *et al.*, "Advanced Virgo: a second-generation interferometric gravitational wave detector", Classical and Quantum Gravity, **32** 024001 (2015)

[8] B.P. Abbott *et al.*, "Prospects for observing and localizing gravitational-wave transients with Advanced LIGO, Advanced Virgo and KAGRA", Living Reviews in Relativity, **21** 3 (2018)

[9] K. Kuroda *et al.*, "Large-scale Cryogenic Gravitational wave Telescope", International Journal of Modern Physics D, **8**, 557 (1999)

[10] K. Somiya [KAGRA Collaboration], "Detector configuration of KAGRA-the Japanese cryogenic gravitational-wave detector", Classical and Quantum Gravity, **29**, 124007 (2012)

[11] Akutsu *et al.* [KAGRA Collaboration], "Construction of KAGRA: an underground gravitational-wave observatory", Progress of Theoretical and Experimental Physics, **2018** 013F01 (2018)

[12] Akutsu *et al.* [KAGRA Collaboration], "First cryogenic test operation of underground km-scale gravitational-wave observatory KAGRA", Classical and Quantum Gravity, **36** 165008 (2019)

[13] Y. Sakakibara *et al.*, "Calculation of thermal radiation input via funneling through a duct shield with baffles for KAGRA", Classical and Quantum Gravity, **29** 205019 (2012)

[14] Y. Sakakibara *et al.*, "A Study of Cooling Time Reduction of Interferometric Cryogenic Gravitational Wave Detectors Using a High-Emissivity Coating", Advances in Cryogenic Engineering (Conference Proceedings), **1573** 1176-1183 (2014)

[15] D. Chen, "Study of a cryogenic suspension system for the gravitational wave telescope KAGRA", Doctoral Dissertation, University of Tokyo (2014)

[16] LCGT Collaboration, "LCGT Design Document ver3.0", https://gwdoc.icrr.u-tokyo.ac.jp/cgi-bin/DocDB/ShowDocument?docid=30

[17] M. Puntro *et al.*, "The Einstein Telescope: a third-generation gravitational wave observatory", Classical and Quantum Gravity, **27** 194002 (2010)

[18] C. Misner, K. Thorne, J. A. Wheeler, "GRAVITATION", Princeton University Press (2017)

[19] J. B. Hartle, "GRAVITY", Addison Wesley (2003)

[20] E. D. Black and R. N. Gutenkunst, "An introduction to signal extraction in interferometric gravitational wave detectors", American Journal of Physics, **71** 365 (2003)

[21] K. Hasegawa, "Optical and thermal study of molecular thin layers on cryogenic mirrors in next-generation gravitational wave telescopes", Doctoral Dissertation, University of Tokyo (2019)

[22] M. Ando, "Power recycling for an interferometric gravitational wave detector", Doctoral Dissertation, University of Tokyo (1998)

[23] J. Mizuno, "Resonant sideband extraction: a new configuration for interferometric gravitational wave detectors", Physics Letters A, **175** 5 p.273 (1993)

[24] A. Khalaidovski *et al.*, "Evaluation of heat extraction through sapphire fibers for the GW observatory KAGRA", Classical and Quantum Gravity, **31** 105004 (2014)

[25] D. Shoemaker *et al.*, "Noise behavior of the Garching 30-m prototype gravitational-wave detector", Physical Review D, **38** 423 (1988)

[26] K. Miyo, "A Study of Baseline Compensation System for Stable Operation of Gravitational-wave Telescopes", Doctoral Dissertation, University of Tokyo (2019)

[27] V. B. Braginsky, V. P. Mitrofanov and K. V. Tokmakov, "On the thermal noise from violin modes of the test mass suspension in gravitational wave antennae", Physics Letters A, **186** 18 (1994)

[28] T. Akutsu *et al.* [KAGRA Collaboration], "Overview of KAGRA: Detector design and construction history", Progress of Theoretical and Experimental Physics, (2020)

[29] B.P. Abbott *et al.*, "GW170814: A Three-Detector Observation of Gravitational Waves from a Binary Black Hole Coalescence", Physical Review Letters, **119** 141101 (2017)

[30] B.P. Abbott *et al.*, "GWTC-1: A Gravitational-Wave Transient Catalog of Compact Binary Mergers Observed by LIGO and Virgo during the First and Second Observing Runs", Physical Review X, **9** 031040 (2019)

[31] B.P. Abbott *et al.*, "GWTC-2: Compact Binary Coalescences Observed by LIGO and Virgo During the First Half of the Third Observing Run", arXiv:2010.14527 (2020)

[32] B.P. Abbott *et al.*, "GW190814: Gravitational Waves from the Coalescence of a 23 Solar Mass Black Hole with a 2.6 Solar Mass Compact Object", The Astrophysical Journal Letters, **896** L44 (2020)

[33] M. Dominik *et al.*, "Double Compact Objects. III. Gravitational-wave Detection Rates", The Astrophysical Journal, **806** 263 (2015)

[34] K. Inayoshi, "Formation pathway of Population III coalescing binary black holes through stable mass transfer", Monthly Notices of the Royal Astronomical Society, **468** 5020 (2017)

[35] I. Mandel and S. E. de Mink, "Merging binary black holes formed through chemically homogeneous evolution in short-period stellar binaries", Monthly Notices of the Royal Astronomical Society, **458** (2016)

[36] S. F. Portegies Zwart and S. L. W. McMillan, "Black Hole Mergers in the Universe", The Astrophysical Journal Letters, **528** 1 (2000)

[37] F. Antonini, N Murray, and S. Mikkola, "Black Hole Triple Dynamics: A Breakdown of the Orbit Average Approximation and Implications for Gravitational Wave Detections", The Astrophysical Journal Letters, **781** 1 (2014)

[38] B. McKernan *et al.*, "Intermediate mass black holes in AGN discs - I. Production and growth", Monthly Notices of the Royal Astronomical Society, **425** 460 (2012)

[39] B. J. Carr and S. W. Hawking, "Black Holes in the Early Universe", Monthly Notices of the Royal Astronomical Society, **168** 399 (1974)

[40] S. E. Woosley, "Pulsational Pair-instability Supernovae", The Astrophysical Journal, **836** 244 (2017)

[41] M. Maggiore, "Gravitational Waves: Volume 1: Theory and Experiments", Oxford University Press, (2007)

[42] J. H. Taylor, L. A. Fowler, and P. M. McCulloch, "Measurements of general relativistic effects in the binary pulsar PSR1913+16", Nature, **277** 437 (1979)

[43] M. Takamoto *et al.*, "Test of general relativity by a pair of transportable optical lattice clocks", Nature Photonics, **14** 411 (2020)

[44] B.P. Abbott *et al.*, "Tests of General Relativity with Binary Black Holes from the second LIGO-Virgo Gravitational-Wave Transient Catalog", arXiv:2010.14529

[45] E. Hirose *et al.*, "Mechanical loss of a multilayer tantala/silica coating on a sapphire disk at cryogenic temperatures: Toward the KAGRA gravitational wave detector", Physical Review D, **90** 102004 (2014)

[46] Y. Michimura *et al.*, JGW-T1707038-v9 : https://gwdoc.icrr.u-tokyo.ac.jp/cgi-bin/DocDB/ShowDocument?docid=7038

[47] S. Bonnefoy-Claudet, F. Cotton, and R-Y. Bard, "The nature of noise wavefield and its applications for site effects studies: A literature review", Earth-Science Reviews, **79** 205 (2006)

[48] K. Okutomi, "Development of 13.5-meter-tall Vibration Isolation System for the Main Mirrors in KAGRA", Doctoral Dissertation, The Graduate University for Advanced Studies (2019)

[49] K. Okutomi *et al.*, KAGRA log book 3441: http://klog.icrr.u-tokyo.ac.jp/osl/?r=3441

[50] T. Akutsu *et al.*, "Cryogenic suspension design for a kilometer-scale gravitational-wave detector", arXiv: 2010.01889

[51] T. Nishimoto, "Development of tilt adjustment mechanism for KAGRA cryogenic mirror suspension (in Japanese)", Master Thesis, University of Tokyo (2020)

[52] A. A. van Veggel and C. Killow, "Hydroxide catalysis bonding for astronomial instrument", Advanced Optical Technologies, 293 (2014)

[53] T. Yamada, "A Study of the KAGRA Cryogenic Payload System and its Conductive Cooling (in Japanese)", Master Thesis, University of Tokyo, (2017)

[54] W. E. Gifford and H. O. McMahon, "A New Low-Temperature Gas Expansion Cycle - Part II", Advances in Cryogenic Engineering (Conference Proceedings), **5** 368 (1960)

[55] C. Wang and P. E. Gifford, "Performance Characteristics of a 4 K Pulse Tube in Current Applications", Cryocoolers (Conference Proceedings), **11** 205 (2001)

[56] NIST Cryogenics, Cryogenics Technology Resources, Cryocoolers : https://trc.nist.gov/cryogenics/cryocoolers.html

[57] T. Tomaru *et al.*, "Vibration-Free Pulse Tube Cryocooler System for Gravitational Wave Detectors I - Vibration-Reduction Method and Measurement -", Cryocoolers (Conference Proceedings), **13** 695 (2004)

[58] R. Li *et al.*, "Vibration-Free Pulse Tube Cryocooler System for Gravitational Wave Detectors II - Cooling Performance and Vibration -", Cryocoolers (Conference Proceedings), **13** 703 (2004)

[59] Y. Ikushima *et al.*, "Ultra-low Vibration Pulse Tube Cooling System, Cooling Performance and Vibration (in Japanese)", TEION KOUGAKU (Journal of Cryogenics and Superconductivity Society of Japan), **43** 1 (2008)

[60] S. Aisenberg and R. Chabot, " Ion-Beam Deposition of Thin Films of Diamondlike Carbon ", Journal of Applied Physics, **42** 7 (1971)

[61] R. Takahashi *et al.*, "Application of diamond-like Carbon (DLC) coatings for gravitational wave detectors", Vacuum (Conference Proceedings), **73** 145 (2004)

[62] Asahi Precision Co., Ltd. : http://www.akg.jp/puresijyon/products/solbk.htm

[63] G. F. Naterer, "Advanced Heat Transfer", CRC Press (2018)

[64] S. Takada *et al.*, "Development of low magnetism Black coating of high emissivity of Ni-P type (in Japanese)", Poster 1P-p18, Cryogenics and Superconductivity Society of Japan meeting, Kochi, Japan (2017)

[65] H. Hoshikawa *et al.*, "Magnetoresistance of 5 N, 6 N, and 6 N8 High Purity Aluminum", Advances in Cryogenic Engineering (Conference Proceedings), **1435** 140 (2012)

[66] T. Sumomogi *et al.*, "Purification of 6N Aluminum by Ultrahigh-Vacuum Melting", Material Transactions, **53** 6 (2012)

[67] J. Tuttle, E. Canavan, and A. Jahromi, "Cryogenic thermal conductivity measurements on candidate materials for space missions", Cryogenics, **88** 36 (2017)

[68] Ed. by Douglas Mann, "LNG Materials and Fluids", National Bureau of Standards, Cryogenics Division, First Edition, (1977)

[69] T. Yamada *et al.*, "High Performance Thermal Link with Small Spring Constant for Cryogenic Applications", Cryogenics (accepted)

[70] Y. S. Touloukian and C. Y. Ho, "Thermophysical Properties of Matter, Vol. 2, Thermal Conductivity Conductivity - Nonmetaric Solids", The TPRC Data Series, IFI/PLENUM New York-Washington (1970).

[71] Y. Sakakibara *et al.*, "Progress on the cryogenic system for the KAGRA cryogenic interferometric gravitational wave telescope", Classical and Quantum Gravity, **31** 224003 (2014)

[72] T. Shishido, "A study of the sapphire suspension fiber for cryogenic gravitational wave detector KAGRA", Master Thesis, The Graduate University for Advanced Studies (2019)

[73] Calculated by Dr.Okutomi using SUMCON

[74] K. Kasahara *et al.*, "Study of Heat Links for a Cryogenic Laser Interferometric Gravitational Wave Detector (in Japanese)", TEION KOUGAKU (Journal of Cryogenics and Superconductivity Society of Japan) **39**, 1 (2004)

[75] Japanese Industrial Standards, JISB2704 (permitted)

[76] T. Tomaru *et al.*, "Conduction Cooling Using Ultra-pure Fine Metal Wire I -Pure Aluminum- (in Japanese)", TEION KOUGAKU (Journal of Cryogenics and Superconductivity Society of Japan), **46** (2011)

[77] NIST Cryogenics, Material Properties, Stainless Steel 316 : https://trc.nist.gov/cryogenics/materials/316Stainless/316Stainless_rev.htm

[78] T. Akutsu *et al.*, "Compact integrated optical sensors and electromagnetic actuators for vibration isolation systems in the gravitational-wave detector KAGRA", Reviews of Scientific Instruments, **91** 115001 (2020)

[79] Cryogenics and Superconductivity Society of Japan, "超電導・低温工学ハンドブック (Translation: Superconductivity and Cryogenic Engineering Handbook)", (1993)

[80] Y. Michimura *et al.*, KAGRA log book 10033: http://klog.icrr.u-tokyo.ac.jp/osl/?r=10033

[81] R. E. Honig and H. O. Hook : RCA Rev. **21** 360 (1960)

[82] H. Kumagai *et al.*, "真空の物理と応用 (Translation: Physics and Application of Vacuum)", Shokabo Co., Ltd. (1970)

[83] Y. Michimura *et al.*, JGW-G2012212-v3: https://gwdoc.icrr.u-tokyo.ac.jp/cgi-bin/DocDB/ShowDocument?docid=12212

[84] M. Shibata, "Effect of Varying Rate Spring with Two Stages on Preventing Surging Phenomenon (in Japanese)", Transactions of Japan Society of Spring Engineers, **1969** 14 (1969)

[85] Y. Takei *et al.*, "Vibration isolation system for cryocoolers of soft x-ray spectrometer on-board ASTRO-H (Hitomi)", Journal of Astronomical Telescopes, Instruments, and Systems, **4**(1), 011216 (2018)

[86] R. C. Dhuley *et al.*, "First demonstration of a cryocooler conduction cooled superconducting radiofrequency cavity operating at practical cw accelerating gradients", Superconductor Science and Technology, **33** 6 (2020)